Die approbierte Originalversion dieser Diplom-/Masterarbeit ist in der Hauptbibliothek der Technischen Universität Wien aufgestellt und zugänglich.
http://www.ub.tuwien.ac.at

The approved original version of this diploma or master thesis is available at the main library of the Vienna University of Technology.
http://www.ub.tuwien.ac.at/eng

DIPLOMARBEIT

Ab Initio und experimentelle Untersuchungen von Titan-Wolfram Diffusionsbarrieren

zur Erlangung des akademischen Grades

Diplom-Ingenieur

im Rahmen des Studiums

066 461 Masterstudium Technische Physik

eingereicht von

Sebastian Bichelmaier
Matrikelnummer 01325275

ausgeführt am Institut für Angewandte Physik
der Fakultät für Physik der Technischen Universität Wien
in Zusammenarbeit mit Infineon Technologies Austria AG

Betreuung:
Univ. Prof. Dipl.-Phys. Peter Mohn
Dr. Michael Nelhiebel
Dr. Johannes Zechner

Wien, 11.02.2019 _____ _____

This work was funded by the Austrian Research Promotion Agency (FFG) within the framework of Project No. 863947.

Acknowledgements

First and foremost I want to express my sincere gratitude to my supervisor Peter Mohn for his continous support, useful input and openness to my ideas. Thanks are also due to his whole group, especially Wernfried Mayr-Schmölzer who tought me the basics of VASP and always lent a helping hand with technical issues.

I especially want to thank Mischa Nelhiebel of KAI/Infineon who enabled me to do things normally impossible for a mere diploma student and always had the big picture in mind when I needed guidance. The countless meetings and discussions with him, Hannes Zechner and many other members of KAI, not only provided useful input, but also furthered my organizational and presentation skills. Many thanks are also due to Benjamin Steinwender for Latex support.

I also am indebted to Flo Pribahsnik and Matthias Röcklinger, who picked me up when the lonesomeness of Villach halted my motivation and with whom I always had a lot of fun during and after work.

Furthermore, I want to thank Anna Regoutz from the Imperial College London for being committed to making experimental analysis of the samples possible, doing a great deal of analysis of the data and providing me with a glimpse of the magic of experimental physics.

Lorenz Romaner, Jürgen Spitaler, Maxim Popov and Rishi Bodlos of the Material Center Leoben can also not be thanked enough for helping out with formulating the approach, diffusion calculations and the occasional buggy potential file.

I want to express my love and gratitude to my girlfriend, Martina, who supported me even through her term spent abroad. Finally I want to thank my family and all my friends, especially Julian and Georg.

Kurzfassung

In der vorliegenden Arbeit wurde das in der Halbleiterindustrie verwendete Material Titan-Wolfram, das als Adhäsionsschicht und Diffusionsbarriere eingesetzt wird, mit Dichtefunktionaltheorie (VASP) und (harter) Röntgenphotoelektronenspektroskopie (HAXPES und XPS) untersucht, wobei versucht wurde die Verteilung des Titan in den Körnern, bzw. an den Korngrenzen, sowie den Einfluss von Wärmebehandlungen auf das Material zu bestimmen. Dafür wurden 16 Strukturdateien, sowie zwölf experimentelle Proben festgelegt.

Die 16 Strukturen weisen positive Bildungsenthalpien auf, was darauf hindeutet, dass sie thermodynamisch meta- oder instabil sind. Die simulierten Zustandsdichten weisen zwar Merkmale auf, die eine Unterscheidung zwischen Korn- und Korngrenzen-Titan ermöglichen würden, jedoch ist der Streuquerschnitt des Titans zu klein, wodurch es in den experimentellen Untersuchungen nur eine geringe Signalintensität liefert.

Dennoch wurde festgestellt, dass höhere Titankonzentration zu einer geringeren Zustandsdichte nahe des Ferminiveaus führt, was auch in den Experimenten an wärmebehandelten Proben sichtbar ist. Auf dieser Erkenntnis aufbauend wurde die aus der Literatur bekannte Vermutung, dass Titan beim Erhitzen aus dem Material diffundiert, bestätigt.

Um dieses Phänomen besser zu verstehen wurde der Diffusionskoeffizient von Titan im Wolframkorn bestimmt. Bei den vorliegenden Temperaturen (400 °C) kann eine Diffusion im Korn ausgeschlossen werden, woraus geschlossen wird, dass ein signifikanter Anteil des Titans in der Korngrenze gelöst sein muss.

Abstract

In this thesis the material titanium-tungsten, which is used in semiconductor industry as adhesion layer and diffusion barrier, was analyzed using density functional theory (VASP) and (hard) X-ray photoelectron spectroscopy (HAXPES and XPS). It was attempted to determine the distribution of titanium between bulk and grain boundaries, as well as the material's response

to annealing treatments. To this end 16 structures and twelve experimental samples were identified.

The 16 structures all exhibit a positive enthalpy of formation, indicating a meta- or unstable state. While the simulated densities of states show characteristics that would theoretically allow for a distinction between bulk and grain boundary titanium, the cross section of titanium is too low, resulting in a low intensity of the titanium signal in the experimental data. However, it was determined that a higher titanium concentration results in a lower density of states near the Fermi energy, which is confirmed by experiment. Building on this we were able to confirm the conjecture from literature, that titanium diffuses out of the material when annealed.

To better understand this phenomenon, the diffusion coefficient of titanium in bulk tungsten was determined. For the temperatures at hand (400 °C) bulk diffusion is not relevant. Consequently, a significant portion of titanium has to be located in the grain boundary in the first place.

Contents

List of Figures **9**

List of Tables **11**

1. Introduction **13**

2. Theory **15**
2.1. Many-Body Quantum Systems 15
2.1.1. Born-Oppenheimer Approximation 16
2.1.2. Hartree and Hartree-Fock Approximation 17
2.1.3. Density Functional Theory 18
2.2. Crystal Lattices 22
2.2.1. Lattice Structures 22
2.2.2. Reciprocal Space 22
2.2.3. Surfaces and Grain Boundaries 23
2.2.4. Special Quasi-Random Structures 24
2.3. Diffusion 26
2.3.1. Self-Diffusion 26
2.3.2. Impurity Diffusion 29
2.4. Experimental Techniques 31
2.4.1. Photoelectric Effect 31
2.4.2. (Hard) X-Ray Photoelectron Spectroscopy 31

3. Computational and Experimental Method **35**
3.1. Computational Method 35
3.1.1. General 35
3.1.2. Relaxation 35
3.1.3. Nudged - Elastic Band 36
3.1.4. Phonon Calculations 37
3.1.5. Convergence of Results 37
3.1.6. Analysis of DFT Results 38
3.2. Experimental Method 38
3.2.1. XPS Experiments 38
3.2.2. HAXPES Experiments 39

4. Results and Discussion **43**
4.1. Equilibrium Lattice Parameter 43
4.1.1. Relation of Lattice Parameter and Ti-Content 45

4.2. Electronic Structure 45
4.2.1. Analyzed Cells and Samples 45
4.2.2. Results 51
4.3. Self-Diffusion of Tungsten 61
4.3.1. Vacancy Concentration 61
4.3.2. Tracer Jump Frequency 62
4.3.3. Result 63
4.4. Diffusion of Titanium in Tungsten 65

5. Conclusion and Outlook **69**

A. CL Spectra of the Samples **73**
A.1. XPS Spectra 73
A.2. HAXPES Spectra 80

B. All Densities of State **87**
B.1. Bulk Structures 88
B.2. Grain Boundary Structures 89

Bibliography **91**

List of Figures

2.1. Hierachy of exchange functionals 20
2.2. The three most common lattice types on the examples of Cu, W and Ti 22
2.3. bcc-W (110) and (111) 24
2.4. Σ5-CSL 24
2.5. Special quasi-random structure $W_{87.5\,\%}Ti_{12.5\,\%}$ 25
2.6. Sketch of transition state in the energy landscape 29
2.7. Possible NN jumps in a bcc-W lattice with a Ti impurity. . . 30
2.8. Principle of the photoelectric effect 32
2.9. Schematic setup of an XPS experiment 32
2.10. Depth resolution of HAXPES 33

3.1. Convergence studies for Ti, W and Cu 40
3.2. Convergence study of the formation enthalpy 41
3.3. Increase of noise with supercell size 41
3.4. Effect of broadening and applying cross-sections 41

4.1. Equilibrium volume search for Ti, W and Cu 44
4.2. Non-Vegard WTi 45
4.3. Bulk structures 47
4.4. Grain boundary structures 48
4.5. Special quasirandom structures of Ti-W alloys 49
4.6. The energy per atom for the structures considered 51
4.7. The heats of formation for the structures considered 52
4.8. The heats of formation per Ti atom for the structures considered 52
4.9. Ti projected DOS of bulk and GB structures 53
4.10. Ti projected DOS of bulk and GB structures 54
4.11. Total projected DOS of bulk and GB structures 55
4.12. Total DOS of bulk and GB structures 55
4.13. Decomposed SQS DOS 56
4.14. The total SQS DOS 56
4.15. XPS measurements comparing annealing effects 57
4.16. HAXPES measurements comparing annealing effects 58
4.17. XPS measurements comparing concentration effects 59
4.18. HAXPES measurements comparing concentration effects . . 60
4.19. Cells necessary for calculating the vacancy concentration . . 61
4.20. Phononic DOS and bandstructure for a W cell. 62
4.21. Phonon DOS of W from literature 62

4.22. Equilibrium vacancy concentration 63
4.23. The MEP of w_0 64
4.24. Phonon DOS for perfect, initial and transition state 64
4.25. Self-diffusion coefficient of tungsten 65
4.26. MEP and phonon spectra involved in w_2 66
4.27. MEP and phonon spectra involved in w_3 66
4.28. Diffusion coefficient of Ti in W 67

A.1. XPS CL spectra comparing different anneals of sample 2 . . 73
A.2. XPS CL spectra comparing different anneals of sample 4 . . 74
A.3. XPS CL spectra comparing different anneals of sample 6 . . 75
A.4. XPS CL spectra comparing different anneals of sample 8 . . 76
A.5. XPS CL spectra comparing different concentrations of as deposited samples 77
A.6. XPS CL spectra comparing different concentrations of briefly annealed samples 78
A.7. XPS CL spectra comparing different concentrations of long-term annealed samples 79
A.8. HAXPES CL spectra comparing different anneals of sample 2 80
A.9. HAXPES CL spectra comparing different anneals of sample 4 81
A.10. HAXPES CL spectra comparing different anneals of sample 6 82
A.11. HAXPES CL spectra comparing different anneals of sample 8 83
A.12. HAXPES CL spectra comparing different concentrations of as deposited samples 84
A.13. HAXPES CL spectra comparing different concentrations of briefly annealed samples 85
A.14. HAXPES CL spectra comparing different concentrations of long-term annealed samples 86

B.1. All bulk DOSes 88
B.2. All GB DOSes 89

List of Tables

3.1. XPS regions of interest 39
3.2. HAXPES regions of interest 39

4.1. Equilibrium lattice parameters 43
4.2. Summary of input structures for the DFT calculations. . . . 46
4.3. Summary of Ti-W samples. 50
4.4. Vacancy formation parameters of W 63
4.5. Comparison of self-diffusion parameters with literature . . . 65

1. Introduction

In today's semiconductor industry the race to ever increasing complexity has necessitated the move to smaller and smaller structures. This has introduced new challenges, one of which is to efficiently prevent the active device from overheating. In this area copper (Cu) has replaced aluminum [1] due to its low bulk electrical resistivity, improved thermal conductivity and resistance to electromigration.

However, even at relatively low temperatures Cu migrates into silicon (Si) [2] and can thus lead to a breakdown of the device. Thus diffusion barriers are necessary to enable design and continued functionality of semiconductor devices [3].

A commonly used diffusion barrier is a sputtered titanium (Ti) - tungsten (W) layer [4], where the Ti is thought to sit at the grain boundary of W and thus block diffusion along the grain boundaries. However, a lot is still unclear about the actual atomic structure of sputtered Ti-W diffusion barriers. With the continuous shrinkage of the technology in mind, the need for new materials with improved properties arises. To enable this process and increase efficiency, a fundamental understanding of the workings of current materials is desirable. However, neither the distribution of Ti, nor its stability with increasing temperature or even its diffusion coefficient in W is known - reference books on material properties do not list a lot of information [5].

The density of states (DOS) of a material is highly susceptible to slight changes in the chemical bonds and thus the local atomic structure and distribution of elements. Density functional theory (DFT) has been shown to be a well-tested and reliable way of obtaining orbital decomposed DOS [6–9]. Only recently it was shown that segregation in the energetically most favorable $\Sigma 3$ grain boundary (GB), [10] of the nanocrystalline W is possible, albeit unlikely [11]. However, Ti atoms blocking GB diffusion, is how the diffusion barrier is expected to work.

By combining DFT with state of the art X-ray photoelectron spectroscopy (XPS) and hard X-ray photoelectron spectroscopy (HAXPES) experiments we aim to gain an understanding of the distribution and dynamics of Ti in the Ti-W diffusion barrier, thus providing valuable input for the development of new materials.

The heat (or enthalpy) of formation is a quantity known best from chemistry, describing if the formation of a compound is exothermic, i.e. realeases energy, or endothermic, i.e. requires energy [12]. It can be used to determine the stability of the compounds involved - endothermic structures tend to be meta- or unstable. The heats of formation and DOS of six GB structures, six bulk structures and four special quasi-random structures (SQS) will be calculated, to see whether some are more stable than others or if special features in the DOS emerge, making experimental identification of Ti at GB possible.

Complementary to this, the question arises of how fast Ti diffusion in W is taking place - and at what temperatures. It is unclear, if the atoms remain as deposited by the sputtering process, which typically is far from an equilibrium structure, or if equilibration during various annealing steps in wafer production can take place.

There have been many efforts to derive diffusion coefficients from first principles to improve upon empirical or semi-empirical models and enable design of materials with required diffusivities. For cubic systems where vacancy mediated diffusion is the predominant mechanism, a procedure within the framework of DFT and transition state theory (TST) was devised [13–15] that enables the calculation of self-diffusion coefficients from first principles.

Many efforts since went into furthering this methodology to enable calculation of impurity diffusion coefficients as well [16, 17]. One way to achieve this is using LeClaire and Lidiard's five frequency model [18] (for face centered cubic - fcc - structures) and extensions thereof (for other crystal symmetries). The results of these simulations fit the experimental reality astonishingly well [17] which is why this approach is utilized in this thesis.

We will be using DFT and TST together with a slightly adapted frequency model, to account for the body centered cubic (bcc) structure of W, to calculate the diffusion pre-factor (D_0) as well as the activation energy (Q) of a Ti impurity diffusing in W. The approach includes static total energy contributions as well as dynamic vibrational entropies due to phonons.

In the second chapter the basic theory will be presented, in the third chapter the computational and experimental methodology is described and in the fourth chapter the results will be presented and discussed. Finally a conclusion and outlook will be provided.

2. Theory

2.1. Many-Body Quantum Systems

This chapter is based on the lecture notes of solid state physics II [19].

For non-relativistic quantum problems considered in this thesis, one has to solve the Schroedinger Equation,

$$i\hbar\partial_t \left|\Psi\right\rangle = \hat{H}\left|\Psi\right\rangle,$$

as well as its time-independent form

$$\hat{H}\left|\Psi\right\rangle = E\left|\Psi\right\rangle, \tag{2.1}$$

where $|\Psi\rangle$ is the (normalized) wavefunction of the system, $\hat{H}$ the Hamiltonian operator and E the energy. We will assume no external electromagnetic field. The many-body aspect of Eq. 2.1 is hidden in $\hat{H}$:

$$\hat{H} = \hat{T}_i + \hat{T}_e + \hat{V}_{ee} + \hat{V}_{ii} + \hat{V}_{ie}, \tag{2.2}$$

with the kinetic ($\hat{T}$) and interaction ($\hat{V}$) contributions of the ions (subscript i) and electrons (subscript e), and the mixed interaction of ions and electrons (subscript ie). Looking at the spatial projections of the operators $\langle x'|\hat{X}|x\rangle$, denoted as X, one finds:

$$\begin{aligned}
T_i &= -\sum_{j=1}^{N_i} \frac{\hbar^2\nabla_j^2}{2M_j} \\
T_e &= -\sum_{j=1}^{N_e} \frac{\hbar^2\nabla_j^2}{2m_e} \\
V_{ee} &= \frac{1}{2}\sum_{j=1}^{N_e}{}' \sum_{l=1}^{N_e} \frac{e^2}{|\vec{r}_j - \vec{r}_l|} \\
V_{ii} &= \frac{1}{2}\sum_{j=1}^{N_i}{}' \sum_{l=1}^{N_i} \frac{e^2 Z_j Z_l}{|\vec{R}_j - \vec{R}_l|} \\
V_{ie} &= \sum_{j=1}^{N_i}\sum_{l=1}^{N_e} \frac{e^2 Z_l}{|\vec{r}_j - \vec{R}_l|},
\end{aligned}$$

with $\nabla = (\partial_x, \partial_y, \partial_z)$, and a system containing N_i ions of masses M_j and charges Z_j at positions R_j, N_e electrons of mass m_e at positions r_j and the elementary charge e, and the reduced Planck's constant $\hbar$. The factor $\frac{1}{2}$ in the third and fourth term accounts for the double counting, and the primed sum, $\sum'$, excludes the case $j = l$. For convenience (Hartree) atomic units (a.u.) will be used, thus $m_e = e = \hbar = 1$.

To make this equation more managable and enable current technologies to calculate (approximate) results for even a small number of atoms, some approximations need to be made.

2.1.1. Born-Oppenheimer Approximation

In real space Eq. 2.1 now takes the form of

$$H\Psi(\vec{R}_1, \ldots, \vec{R}_{N_i}; \vec{r}_1, \ldots, \vec{r}_{N_e}) = E\Psi(\vec{R}_1, \ldots, \vec{R}_{N_i}; \vec{r}_1\sigma_1, \ldots, \vec{r}_{N_e}\sigma_{N_e}), \quad (2.3)$$

where σ_i indicates the spin of the i-th electron. Born and Oppenheimer have shown [20] that the error introduced by assuming separability of the ionic and electronic movement is small as long as $m_e \ll M_i$. Then we can write

$$\Psi(\vec{R}_l, \ldots, \vec{R}_{N_i}; \vec{r}_1, \ldots, \vec{r}_{N_e}) = \psi(\vec{R})\phi(\vec{r}\sigma), \quad (2.4)$$

where we have introduced $\vec{R}$ and $\vec{r}$ as the shorthand notations for the $\vec{R}_l$ and $\vec{r}_l$, respectively. The qualitative explanation for this is the fact that since the electrons are much lighter, they can move on timescales much shorter than the ions and thus experience the ions as a static *background*. Therefore the Born-Oppenheimer approximation is sometimes referred to as adiabatic approximation.

Further we assume no coupling to an external field and thus the spin degrees of freedom (DOF) are also separable

$$\phi(\vec{r}\sigma) = \phi(\vec{r})\chi(\sigma), \quad (2.5)$$

and cancel out in Eq. 2.1 if no external field is applied. This leaves the following two equations

$$\underbrace{(T_e + V_{ie} + V_{ee})}_{H_{el}}\phi(\vec{r}) = E_e\phi(\vec{r}) \quad (2.6)$$

$$(T_i + V_{ii} + E_e)\psi(\vec{R}) = i\hbar\partial_t\psi(\vec{R}). \quad (2.7)$$

To further simplify Eq. 2.7, the ionic movements are assumed to behave classically and thus follow Newton's equations of motion

$$M_i\ddot{a}_i = F = -\nabla E_0 = -\nabla(E_e + V_{ii}). \quad (2.8)$$

2.1.2. Hartree and Hartree-Fock Approximation

Solving Eq. 2.7 is still impossible for most systems apart from hydrogen. Hartree's initial guess [21] was that one can simply write the many-particle wavefunction as a product of single-particle wavefunctions:

$$\phi(\vec{r}) = \prod_{j=1}^{N_e} \phi(\vec{r}_i).$$

This poses a serious problem for electrons as they are fermions and hence have to obey Pauli's principle [22]. The more elaborate Hartree-Fock approximation [23] utilizes Slater determinants [24],

$$\phi(\vec{r}) = \frac{1}{\sqrt{N!}} \begin{vmatrix} \phi_1(\vec{r}_1) & \dots & \phi_{N_e}(\vec{r}_1) \\ \vdots & \ddots & \vdots \\ \phi_1(\vec{r}_{N_e}) & \dots & \phi_{N_e}(\vec{r}_{N_e}) \end{vmatrix}, \tag{2.9}$$

thus satisfying the antisymmetrisation requirements of fermions. The expectation value of the energy is

$$\langle E_e \rangle = \int \phi(\vec{r})^\dagger H_{el} \phi(\vec{r}) d\vec{r}_1 \dots d\vec{r}_{N_e}. \tag{2.10}$$

Inserting Eq. 2.9 into Eq. 2.10 and varying it w.r.t. the ϕ_j yields the so-called Hartree-Fock equations

$$\begin{aligned} [-\nabla^2 + \sum_j \int \int \phi_j^\dagger(\vec{r}_2)\phi_j(\vec{r}_2) \frac{2}{|\vec{r}_1 - \vec{r}_2|} d^3 r_2 \\ - \sum_j \int \int \phi_j^\dagger(\vec{r}_2)\phi_l(\vec{r}_2) \frac{2}{|\vec{r}_1 - \vec{r}_2|} d^3 r_2] \phi_l(\vec{r}_1) = \epsilon_l \phi_l(\vec{r}_1). \end{aligned} \tag{2.11}$$

The first integral corresponds simply to the electron-electron interaction, whereas the second one is called the exchange term and is purely quantum in nature. To build the bridge to the next chapter, we consider the case of plane waves:

$$\phi(\vec{k}, \vec{r}) = \mathcal{N} e^{i\vec{k}\vec{r}},$$

where $\mathcal{N}$ is some chosen normalization. Inserting this into Eq. 2.11 yields the following for the exchange energy, ϵ_x:

$$\epsilon_x(\vec{k}) = -\mathcal{N} \sum_q \int e^{i(\vec{k}-\vec{q})(\vec{r}_1 - \vec{r}_2)} \frac{2}{|\vec{r}_1 - \vec{r}_2|} = -8\pi\mathcal{N} \sum_q \frac{1}{|\vec{k} - \vec{q}|^2}. \tag{2.12}$$

After converting the sum to an integral up to the Fermi-vector, $\vec{k}_F$, performing the integration and summing over all of $\vec{k}$-space, we arrive at

$$E_x = -3 \left(\frac{3\rho}{8\pi} \right)^{1/3}. \tag{2.13}$$

This result is quite remarkable, since it relates the exchange energy, a phenomenon arising from the interaction of quantum particles, to a semi-classical quantity, the electron density - a concept that was furthered by Hohenberg and Kohn.

2.1.3. Density Functional Theory

The foundations of Density Functional Theory (DFT) were set by Hohenberg and Kohn, with the Hohenberg-Kohn Theorems (HKT, [25]) which ultimately earned Walter Kohn the Nobel Prize in Chemistry in 1998.

Hohenberg-Kohn Theorems

The Hohenberg-Kohn Theorems relate the electron (groundstate) density, $\rho(\vec{r}) = \phi^\dagger(\vec{r})\phi(\vec{r})$[1], of a system of electrons with an external potential, $V_{ext}(\vec{r})$ (for example the potential of the positively charged ions in the crystal lattice) and its total (groundstate) energy[2]. The first theorem states [25]:

Theorem 1 *$V_{ext}(\vec{r})$ is a unique functional of $\rho(\vec{r})$, apart from a trivial additive constant.*

The proof is done through reductio ad absurdum: assume two different potentials, $v_1(\vec{r})$ and $v_2(\vec{r})$, that lead to the same density, ρ. The two Hamiltonians, $H_1(\vec{r})$ and $H_2(\vec{r})$ will thus have two different ground-state wave-functions, $\phi_1(\vec{r})$ and $\phi_2(\vec{r})$. According to the variational principle [26] it follows that

$$E_1^0 < \langle\Psi_2|H_1|\Psi_2\rangle = \langle\Psi_2|H_2|\Psi_2\rangle - \langle\Psi_2|H_1 - H_2|\Psi_2\rangle$$
$$= E_2^0 + \int n_0(\vec{r})[v_1(\vec{r}) - v_2(\vec{r})]d^3r.$$

Interchanging the subscripts now leads to a similar expression

$$E_2^0 < E_1^0 + \int n_0(\vec{r})[v_2(\vec{r}) - v_2(\vec{r})]d^3r,$$

adding both results in a contradiction

$$E_1^0 + E_2^0 < E_2^0 + E_1^0,$$

thus proving the theorem. A corollary is that since H is uniquely determined by V_{ext}, the full ground-state wave function is a unique functional of ρ.

[1] Where $\phi^\dagger$ indicates the complex conjugation and transposition ϕ.

[2] NB: Indeed, it relates the value of *any* observable to the groundstate density; energy just being one example.

We shall now introduce the functional

$$F[\rho(\vec{r})] = \langle\phi|H - V_{ext}|\phi\rangle \,,$$

thus expressing the total energy as

$$E[\rho(\vec{r})] = \langle\phi|H|\phi\rangle = F[\rho(\vec{r})] + \int \rho(\vec{r})V_{ext}d^3r. \tag{2.14}$$

The second theorem states [25]:

Theorem 2 *Eq. 2.14 takes its minimum value, the groundstate energy E_0, for the correct groundstate density $\rho(\vec{r})$, if the total number of particles, N, is kept constant.*

This follows as a consequence of the general variational principle of quantum mechanics [26], since the energy functional of an N particle system

$$E[\phi'] = \langle\phi'|V_{ext}|\phi'\rangle + \langle\phi'|(T+U)|\phi'\rangle \,, \tag{2.15}$$

has a minimum at the correct ground state wave function $|\phi\rangle$, w.r.t. variations of $|\phi'\rangle$. Assuming now that $|\phi'\rangle$ is the ground state of a different external potential V'_{ext}, then

$$E[\phi'] = \int V_{ext}(\vec{r})\rho'(\vec{r})d^3r + F[\rho'(\vec{r})] > E[\phi] = \int V_{ext}(\vec{r})\rho(\vec{r})d^3r + F[\rho(\vec{r})],$$

thus showing that Eq. 2.15 is minimal relative to all densities $\rho'(\vec{r})$ arising from other external potentials $V'_{ext}(\vec{r})$ [25].

Kohn-Sham Equations

Together with L. J. Sham, Kohn developed a formalism that utilizes the Hohenberg-Kohn Theorems and lays the foundations for modern DFT applications [27]. Their approach was to express the density in terms of single-electron wave functions, $\phi_i(\vec{r})$, thus resulting in the following expression for the total energy [28]:

$$\begin{aligned} E[\phi_i(\vec{r})] = &-\sum_i \int \phi_i^\dagger \nabla^2 \phi_i d^3r + \int V(\vec{r})\rho(\vec{r})d^3r + \\ &\frac{1}{2}\int\int \frac{\rho(\vec{r})\rho(\vec{r}')}{|\vec{r}-\vec{r}'|}d^3r d^3r' + E_{ion} + E_{XC}[\phi_i]. \end{aligned} \tag{2.16}$$

Variation of Eq. 2.16 w.r.t. $\phi_i^\dagger$ leads to

$$\left[-\frac{1}{2}\nabla^2 + V(\vec{r}) + \int \frac{\rho(\vec{r}')}{|\vec{r}-\vec{r}'|} d^3r' + V_{XC}(\vec{r})\right] \phi_i(\vec{r}) = \epsilon_i \phi_i(\vec{r}), \tag{2.17}$$

which is an effective single-particle Schroedinger equation. As can be seen this points to a self-consistent scheme for solving the Kohn-Sham equations - after an inital guess of the wave functions ϕ_i, we are able to construct a density $\rho = \sum_i \phi_i^\dagger \phi_i$. With this we are able to solve Eq. 2.17 and get a refined expression for the ϕ_i. The only remaining unknown is the exchange part of the energy, V_{XC} in which the e**x**change and **c**orrelation energies are hidden. Unfortunately this quantity is far from unique and depending on computational resources, required accuracy and material properties, different exchange-functionals should be used. In the following section a brief overview of the possibilities will be given.

Hierachy of Exchange Functionals

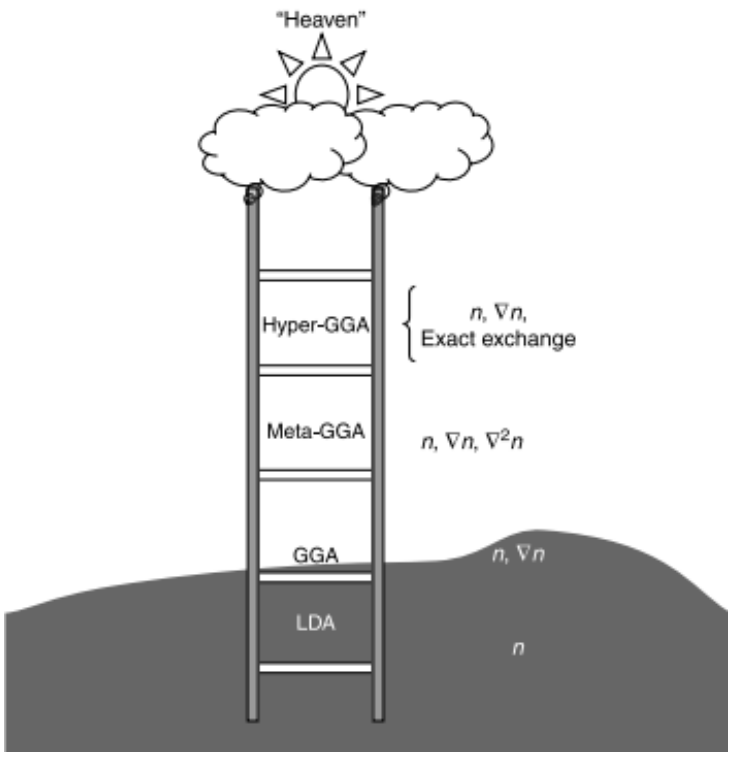

Figure 2.1.: Perdews' hierachy of exchange functionals [29], where $n \equiv \rho$. The image is taken from [28].

A useful analogy of this hierachy was given by Perdew [29] and is depicted in [28]. The graphic is reproduced in Fig. 2.1 and shows the most common exchange functionals and their dependencies. The simplest version is called

local density approximation (LDA) - it is defined as the exchange energy a uniform electron gas with density ρ would exhibit.

On the next step of ladder is the generalized gradient approximation (GGA), dependent not only on the local density, ρ, but also on the local change of density, $\nabla\rho$. The most common implementations of this are the Perdew-Wang 91 (PW91, [30]) and Perdew-Burke-Enzerhof (PBE, [31]). These are indeed the most commonly used XC potentials at the moment.

Further up, we find the meta-GGA functionals, also including the second derivative (i.e. the kinetic energy) of the density ρ (e.g. TPSS, [32]) and finally the hyper- or hybrid-GGAs mixing exact exchange and GGA approaches (e.g. B3LYP, [33, 34]).

While Fig. 2.1 might indicate that going up is *always* better, this is not necessarily true. Often one has to settle for a compromise of accuracy and computational time, or in special cases, a functional on a lower level of the ladder can outperform those above.

Densities of State

The density of states (DOS), $D(E)$, represents the number of states (or orbitals) per unit energy interval [35]:

$$N = \int D(E)dE = \frac{1}{8\pi^2}\int (\nabla_{\vec{k}} E(\vec{k}))^{-1} dS_{\vec{k}},$$

with $dS_{\vec{k}}$ being an element of the constant energy surface $E(\vec{k}) = \epsilon = const.$ That is, the DOS answers the question of how many of the (ϕ_i, ϵ_i) pairs in Eqs. 2.16 and 2.17 lie in an interval $\Delta\epsilon$. Every one of those states can be occupied by two (one spin up, one spin down) electron and the highest occupied state (at $T = 0$K) lies at the Fermi energy, E_f. Since the states can be expanded in any complete basis set it is possible to express the DOS with respect to the $s, p, d, \ldots$ orbitals that are ubiquitous in experimental physics and chemistry and are mathematically represented by the spherical harmonics Y_{lm}.

In this nomenclature $l = 0, 1, \ldots$ is the angular momentum quantum number and $m = -l, -l+1, ...$ is the projection of the angular momentum onto the preferred axis. This multiplicity gives rise to the well-known orbital labels, where s corresponds to $l = m = 0$, p_x, p_y, p_z to $l = 1, m = -1, 0, 1$ and so forth.

2.2. Crystal Lattices

A necessary input for any DFT calculation is the system's geometry. In this thesis only crystalline materials are considered, thus their most important aspects, namely lattice structures and grain boundaries will be covered briefly.

2.2.1. Lattice Structures

The three most common crystalline structures are depicted as their conventional unit cell in Fig. 2.2. Most metallic elements and those under investigation in this thesis crystallize in either face-centered cubic (fcc, e.g. Cu Fig. 2.2a), body-centered cubic (bcc, e.g. W Fig. 2.2b) or hexagonal closed packed (hcp, e.g. Ti Fig. 2.2c) structures.

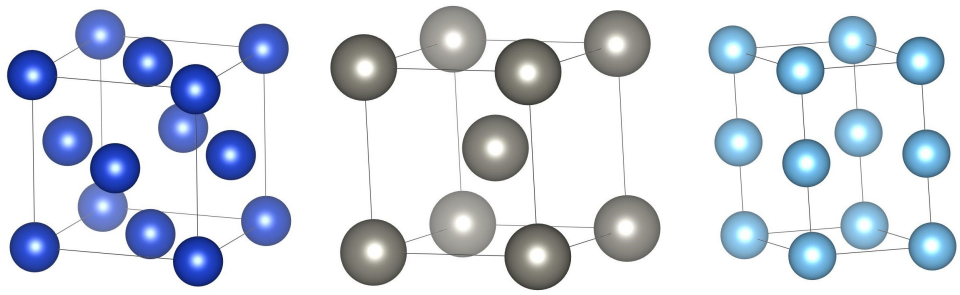

(a) (b) (c)

Figure 2.2.: The three most common lattice types on the examples of the primitive cells of Cu: face-centered cubic (fcc, Fig. 2.2a), W: body-centered cubic (bcc, Fig. 2.2b) and Ti: hexagonal closed packed (hcp, Fig. 2.2c). Graphics created with VESTA [36].

In the simplest case a crystal consists of a periodic repetition of its unit cell. This periodicity can be expressed by translation symmetry, i.e. any function f of the periodic lattice, defined by the unit cell basis $\vec{a}_1, \vec{a}_2, \vec{a}_3$, is invariant under translation of integer, t_1, t_2, t_3, multiples of these basis vectors:

$$f(\vec{r} + t_1\vec{a}_1 + t_2\vec{a}_2 + t_3\vec{a}_3) = f(\vec{r}). \tag{2.18}$$

2.2.2. Reciprocal Space

Performing a fourier transformation of Eq. 2.18

$$n_{\vec{G}} = V_c^{-1} \int_{\text{cell}} dV n(\vec{r}) e^{-i\vec{G}\vec{r}}, \tag{2.19}$$

requires a vector $\vec{G}$, such that

$$n(\vec{r}) = \sum_{\vec{G}} n_{\vec{G}} e^{i\vec{G}\vec{r}}.$$

This is achieved by defining the basis of the reciprocal lattice

$$\vec{b}_1 = 2\pi \frac{\vec{a}_2 \times \vec{a}_3}{\vec{a}_1 \cdot \vec{a}_2 \times \vec{a}_3} \tag{2.20}$$

$$\vec{b}_2 = 2\pi \frac{\vec{a}_3 \times \vec{a}_1}{\vec{a}_1 \cdot \vec{a}_2 \times \vec{a}_3} \tag{2.21}$$

$$\vec{b}_3 = 2\pi \frac{\vec{a}_1 \times \vec{a}_2}{\vec{a}_1 \cdot \vec{a}_2 \times \vec{a}_3}, \tag{2.22}$$

which, for integers v_1, v_2, v_3, form vectors

$$G = v_1\vec{b}_1 + v_2\vec{b}_2 + v_3\vec{b}_3.$$

By Euler‘s identity

$$e^{2\pi i N} = 1 \quad N \in \mathbb{N},$$

the translation symmetry discussed above is achieved, since for a translation $\vec{T} = t_1\vec{a}_1 + t_2\vec{a}_2 + t_3\vec{a}_3$,

$$n(\vec{r} + \vec{T}) = \sum_{\vec{G}} e^{i\vec{G}\vec{r}} e^{i\vec{G}\vec{T}} = \sum_{\vec{G}} e^{i\vec{G}\vec{r}} e^{i2\pi(\underbrace{u_1v_1 + u_2v_2 + u_3v_3}_{\in\mathbb{N}})} = n(\vec{r}),$$

is invariant.

2.2.3. Surfaces and Grain Boundaries

Clearly there are many ways to cut through the structures depicted in Fig. 2.2. A useful concept for describing which plane one is talking about are the miller indices, typically denoted by integers h, k, l, that define a vector in reciprocal space:

$$G_{hkl} = h\vec{b}_1 + k\vec{b}_2 + l\vec{b}_3,$$

and three intersection points in real space,

$$\vec{P}_1 = \frac{\vec{a}_1}{h} \quad \vec{P}_2 = \frac{\vec{a}_2}{k} \quad \vec{P}_3 = \frac{\vec{a}_3}{l},$$

thus defining a plane. For example, the planes (110) and (111) of bcc-W are shown in Figs. 2.3a and 2.3b. If the crystal is not perfect, or consists of multiple elements two planes are adjacent to each other, since the orientation, or even the crystal lattice, might differ. In the case of the same element, but different orientations one talks about a grain boundary, if it contains two different elements this boundary is called an interface.

There is a classification scheme of grain boundaries, motivated by the coincidence site lattice model (CSL, [37]). Consider a square lattice as seen in Fig. 2.4a - if we superimpose the same lattice and rotate it by 36.9° [38], we can see that every fifth site of the original lattice aligns with the rotated one. Thus we call a grain boundary with this structure a $\Sigma 5$ grain boundary.

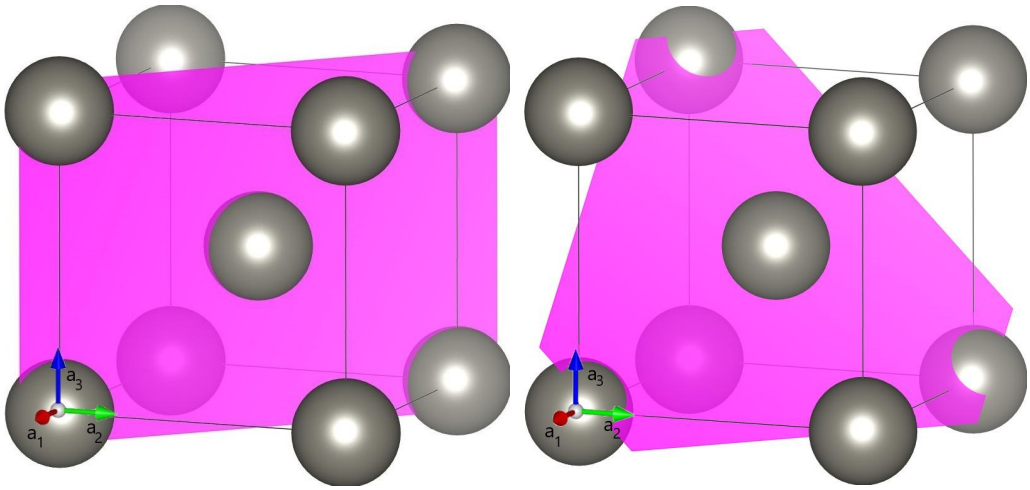

(a) (b)

Figure 2.3.: Two planes in bcc-W:
(a) (110) plane, intersecting axis a_1 and a_2, but parallel to a_3
(b) (111) plane, intersecting a_1, a_2, a_3.

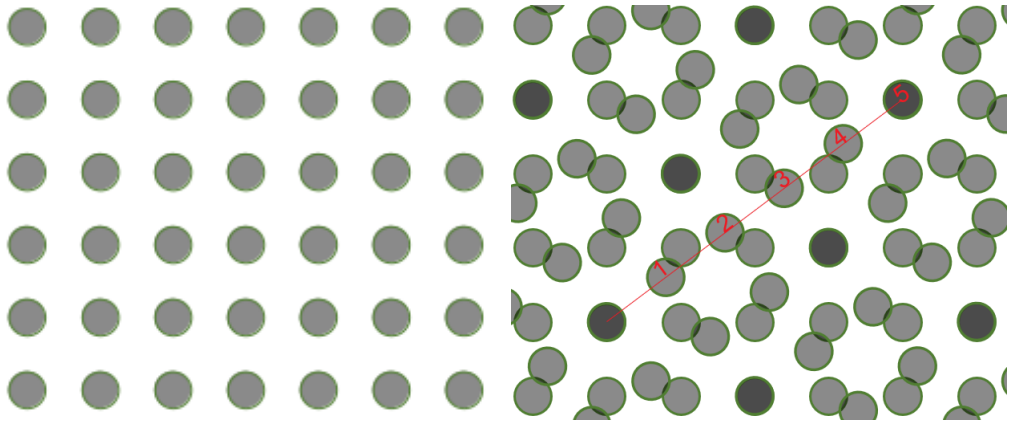

(a) (b)

Figure 2.4.: A square lattice Fig. 2.4a overlayed with the same lattice rotated by 36.9° Fig. 2.4b. Every fifth site coincides, thus it is called a $\Sigma 5$ grain boundary.

2.2.4. Special Quasi-Random Structures

Special quasi-random structures (SQS), proposed by Zunger et al. [39], are structures that can mimic random behaviour (as e.g. sputtered materials exhibit) of bi-alloys ($A_{1-x}B_x$) within relatively small cells and decrease periodicity errors - thus drastically reducing the number of atoms required to simulate realistic structures. It does so by specifically building structures whose radial correlation functions match (or at least approximate) those of the ensemble average of random alloys. The SQS used in this thesis were provided by A. Ruban and M. Dehghani of the Material Center Leoben and

generated using the Automated Alloy Toolkit (ATAT, [40, 41]). A typical 16 atom SQS for $W_{87.5\,\%}Ti_{12.5\,\%}$ is depicted in Fig. 2.5.

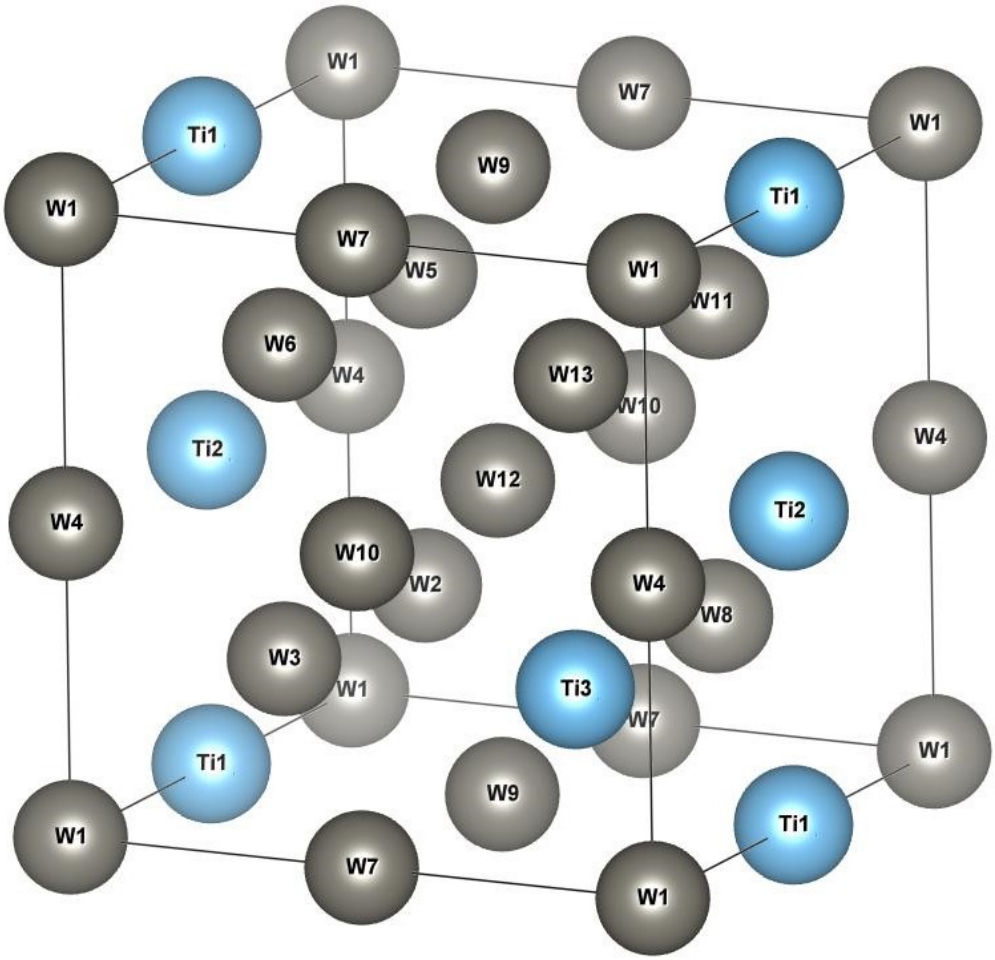

Figure 2.5.: A 16 atom $2 \times 2 \times 2$ Special Quasirandom Structure supercell with the composition $W_{87.5\,\%}Ti_{12.5\,\%}$. Courtesy of MCL.

2.3. Diffusion

2.3.1. Self-Diffusion

In the case of uncorrelated jumps the diffusion coefficient can be described by Einstein's random walk formula [42]

$$D = \frac{1}{2t} \langle X^2 \rangle , \tag{2.23}$$

with the mean square of the net displacement $\langle X^2 \rangle$ over a time t. For cubic systems, as tungsten, all jumps are of the same length, x, and are identically correlated with later jumps (LeClaire in [43]). Therefore $\langle X^2 \rangle$ can be written as $N \langle x^2 \rangle$, when N jumps happen in time t. With the definition of the total tracer jump frequency $\Gamma = \frac{N}{t}$ [44], this can be written as

$$D = \frac{1}{2} \Gamma \langle x^2 \rangle .$$

If the vacancy concentration is denoted C, the probability of having a vacancy in the nearest-neighbour environment, expressed by the coordination number z, of the tracer and the tracer atom jump frequency w_0, Γ can be written as

$$\Gamma = zCw_0,$$

which results in

$$D = \frac{1}{2} zCw_0 \langle x^2 \rangle .$$

Jump Distance

When considering $\langle x^2 \rangle$, the properties of cubic crystal symmetry can again be used to simplify the term. The average jump distance, r, is independent of direction, thus the distance moved along a specific direction x can be evaluated to $\langle x^2 \rangle = \frac{r^2}{3}$. Further we need to factor in that there is some correlation between the jumps (i.e. the fact that jumps back the atom's path are more likely):

$$\langle X^2 \rangle = f \langle X^2 \rangle_{rnd} ,$$

where $f = \frac{1+\langle \cos\theta \rangle}{1-\langle \cos\theta \rangle}$ (LeClaire in [43]), with θ being the angle between any two consecutive jumps, evaluated for bcc crystals to $f = 0.7272$. Using this we arrive at the equation for the diffusion coefficient of cubic crystals:

$$D = \frac{1}{6} zCw_0 r^2 f. \tag{2.24}$$

Considering now the bcc specific case, with a coordination number of $z = 8$ and an average jump distance of $r = \frac{\sqrt{3}a}{2}$, where a is the equilibrium lattice parameter, we arrive at

$$D = Cw_0 a^2 f. \tag{2.25}$$

Vacancy Concentration

To create a vacancy, an atom must be moved from the lattice site to (or above) the surface of the crystal, which requires energy. The other thermodynamic quantity affected is entropy. Thus the relevant thermodynamic potential is the Gibbs free energy:

$$G_f^{1v} = H_f^{1v} - TS_f^{1v} = H_f^{1v} - T(S_f^{1v,c} + S_f^{1v,th}), \tag{2.26}$$

which can be expressed in terms of the enthalpy, H_f, the temperature T and the configurational and thermal (vibrational) entropy, S_f^c and S_f^{th}, respectively. The superscript $1v$ indicates monovacancy processes, when not explicitly mentioned otherwise only these will be considered, therefore the superscript will be omitted. The configurational entropy in a system with $N+n$ sites, consisting of N atoms and n vacancies is given by

$$S_f^c = k_B \ln W_c = k_B \ln \frac{(N+n)!}{N!n!},$$

using now Stirling's approximation for large N [45],

$$\ln N! \approx N(\ln N) - N,$$

this expression can be obtained:

$$S_f^c = -k_B \left(N \ln \frac{N}{N+n} + n \ln \frac{n}{N+n} \right).$$

With this the total change in Gibbs free energy when n vacancies are created in a system can be written as

$$\begin{aligned} nG_f =& nH_f - T(nS_f^{th} + S_f^c) \\ =& n(H_f - TS_f^{th}) + k_B T \left(N \ln \frac{N}{N+n} + n \ln \frac{n}{N+n} \right). \end{aligned}$$

By differentiation w.r.t n the equilibrium value of G_f and thus n can be found. From $\partial G_f / \partial n = 0$ it follows that

$$\frac{n}{N+n} = \exp\left(\frac{S_f^{th}}{k_B}\right) \exp\left(-\frac{H_f}{k_B T}\right),$$

thus the vacancy concentration when forming a single vacancy can now be expressed in microscopic quantities [46],

$$C = \exp\left(\frac{\Delta S_f^{th}}{k_B}\right) \exp\left(-\frac{\Delta H_f^{vac}}{k_B T}\right), \tag{2.27}$$

where ΔH_f^{vac} and ΔS_f^{th} are the enthalpy and entropy of vacancy formation respectively, k_B is the Boltzmann constant and T is the temperature in Kelvin. The enthalpy of formation can be derived using

$$\Delta H_f^{vac} = E((N-1) + \text{vac}) - \frac{N-1}{N} E(N), \tag{2.28}$$

where N is the number of atoms in the perfect system, $E(N)$ its energy and $E((N-1)+\text{vac})$ the energy of a system with $N-1$ atoms and one vacancy. For the vibrational, entropic contribution information about the vibrational states of the system, the phonon frequencies ν, are needed. Using these, the vibrational entropy can be expressed using

$$S^{th} = k_B \int \left\{ \frac{h\nu}{2k_BT} \coth\left(\frac{h\nu}{2k_BT}\right) - \ln\left[2\sinh\left(\frac{h\nu}{2k_BT}\right)\right]\right\} g(\nu)d\nu,$$

or in the case of discrete states, where $g(\nu) = \sum_{i=1}^{3N} \delta(\nu - \nu_i)$,

$$S^{th} = k_B \sum \left\{ \frac{h\nu_i}{2k_BT} \coth\left(\frac{h\nu_i}{2k_BT}\right) - \ln\left[2\sinh\left(\frac{h\nu_i}{2k_BT}\right)\right]\right\}, \tag{2.29}$$

where h is Planck's constant. The vibrational entropy of vacancy formation can then be expressed by

$$\Delta S_f^{th} = S^{th}((N-1)+\text{vac}) - \frac{N-1}{N} S^{th}(N), \tag{2.30}$$

with the same notation as in Eq. 2.28.

Tracer Jump Frequency

Eyrings reaction rate theory and Vineyards improvements [14, 47] can be used to link the tracer jump frequency, w_0, to microscopic quantities:

$$w_0 = \nu^* \exp\left(-\frac{\Delta H_m^{vac}}{k_BT}\right), \tag{2.31}$$

where ΔH_m^{vac} is the vacancy migration enthalpy, corresponding to an energy barrier as depicted in Fig. 2.6 and

$$\nu^* = \frac{\Pi_{i=1}^{3(N-1)} \nu_i}{\Pi_{i=1}^{3N-4} \nu_i'}, \tag{2.32}$$

where the $3N-4$ frequencies ν_i' are those of the transition state, as indicated in Fig. 2.6. Noteworthy here is the explicit exclusion of the one imaginary mode a transition state will exhibit. Putting these equations together yields a formula for the self diffusion coefficient

$$D = \exp\left(\frac{\Delta S_f^{th}}{k_B}\right) \exp\left(-\frac{\Delta H_f^{vac}}{k_BT}\right) \nu^* \exp\left(-\frac{\Delta H_m^{vac}}{k_BT}\right) a^2 f. \tag{2.33}$$

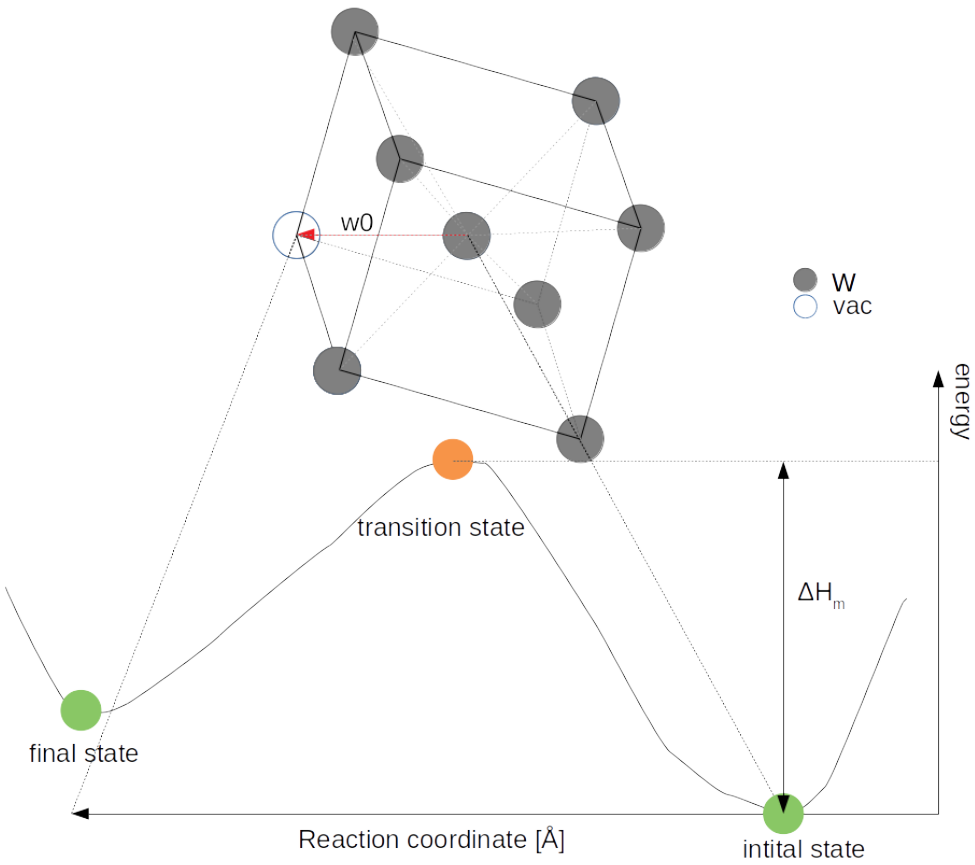

Figure 2.6.: The transition state with the vacancy migration enthalpy ΔH_m^{vac} indicated.

2.3.2. Impurity Diffusion

The underlying concept of the foregoing chapter remains the same but due to the impurity the system now has an increased number of environments where jumps can happen and there is a slight change of the correlation factor. Typically Le Claire's five-frequency model [18] is utilized to describe the different jumps in an fcc metal. In the model only nearest neighbor (NN) interactions are considered, since in fcc the next nearest neighbour (NNN) distances are a lot larger than the NN distances.

While W is a bcc metal, we will nonetheless rely on NN considerations only. This is based on Mantinas result for Mo diffusion in W [15] where she found that NNN binding is very weak, as well as the findings in [48] that suggest that the migration enthalpy for NNN migration is at least twice that of NN migration. Furthermore the jump of the host atom conserving the association of the impurity with the vacancy (usually called w_1) is impossible, as NN bcc atoms do not have common neighbouring sites.

Thus we will only consider the four frequencies as shown in Fig. 2.7:

- w_0: the jump of the host atom in a NN environment of only host atoms
- w_2: the jump of the impurity atom
- w_3: the jump of a host atom disassociating the impurity from the vacancy
- w_4: the reverse of w_3, a jump associating the impurity with the vacancy

Each w_2-w_4 has a similar transition state as shown in Fig. 2.6 for w_0. Using these frequencies, Le Claire's model states that

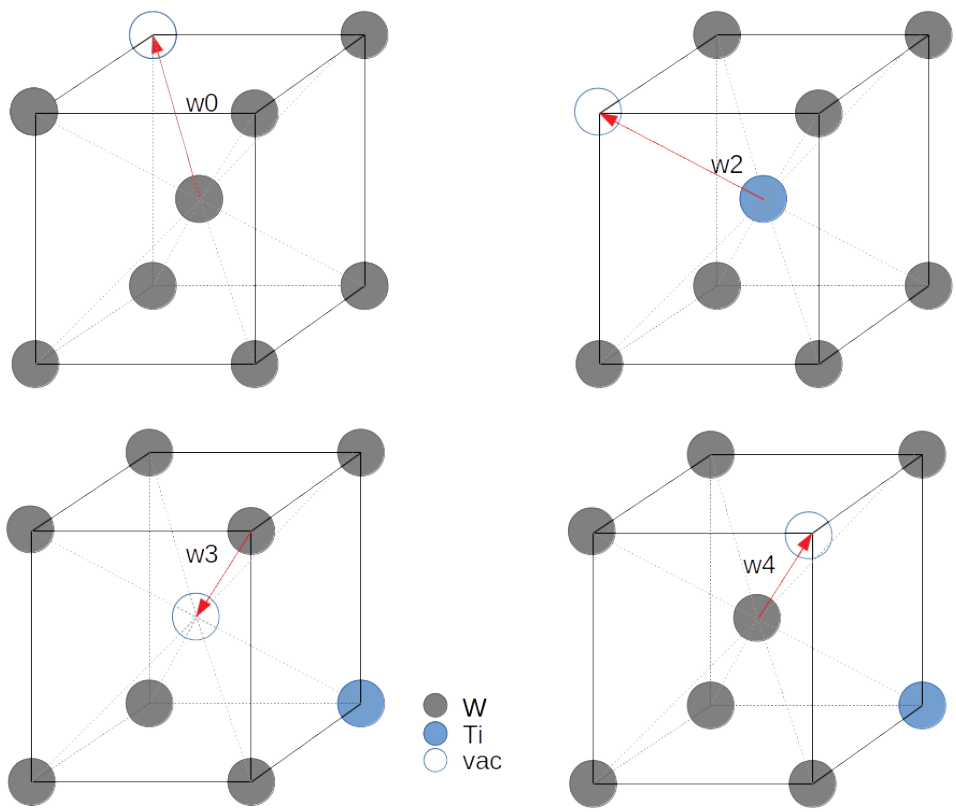

Figure 2.7.: Possible NN jumps in a bcc-W lattice with a Ti impurity.

$$D_2 = D_0 \frac{f_2}{f} \frac{w_4}{w_0} \frac{w_2}{w_3}, \tag{2.34}$$

where D_0 is the self-diffusion coefficient of the host atom, D_2 is the diffusion coefficient of the impurity atom in the host lattice and f_2 is a correction factor for the correlations found in [49]:

$$f_2 = \frac{7w_3 + F_3}{2w_2 + 7w_3F_3}, \tag{2.35}$$

with

$$F_3 = \frac{1}{7}\frac{528.5 + 779.03\frac{w_4}{w_0} + 267.5\left(\frac{w_4}{w_0}\right)^2 + 24\left(\frac{w_4}{w_0}\right)^3}{75.5 + 146.83\frac{w_4}{w_0} + 69.46\left(\frac{w_4}{w_0}\right)^2 + 8\left(\frac{w_4}{w_0}\right)^3}.$$

.

2.4. Experimental Techniques

2.4.1. Photoelectric Effect

If electromagnetic (EM) waves of the right frequency hit a material, electrons are emitted. The energy of the EM wave, $E = h\nu$ has to be high enough to overcome the binding energy, E_B, which is the energy difference between the surface and the location of the electron within the sample. Then an electron with the maximum kinetic energy of

$$E_k = h\nu - E_B, \tag{2.36}$$

can be emitted. This process is known as the photoelectric effect (see Fig. 2.8) and provides the basis for many experimental techniques. Two of these, X-ray photoelectron spectroscopy (XPS) and Hard XPS (HAXPES), will be utilized to examine Ti-W samples, thus we will give a brief introduction of the techniques here. For an in-depth explanation see e.g. [50].

2.4.2. (Hard) X-Ray Photoelectron Spectroscopy

The fundamentals of XPS and HAXPES are the same - as mentioned they both rely on the photoelectric effect. However, they differ with regards to energy, X-ray source and depth resolution. The most important components of those experiments are (see also Fig. 2.9):

- **Vacuum**: When choosing the quality of the vacuum one has to consider the inelastic mean free path (IMFP) of the electron, as well as the oxidation time of the surface since the technique is very surface sensitive. Typical high (1×10^{-11} bar) or ultra-high (1×10^{-12} bar) vacuum is used.

- **X-ray source**: This can be any monochromatic, suitably focused source of X-rays. In classical XPS a heated electrode is used, generating X-rays of up to 2 keV. The high energies of HAXPES (2 keV to 12 keV) usually require a synchrotron or specialized X-ray source.

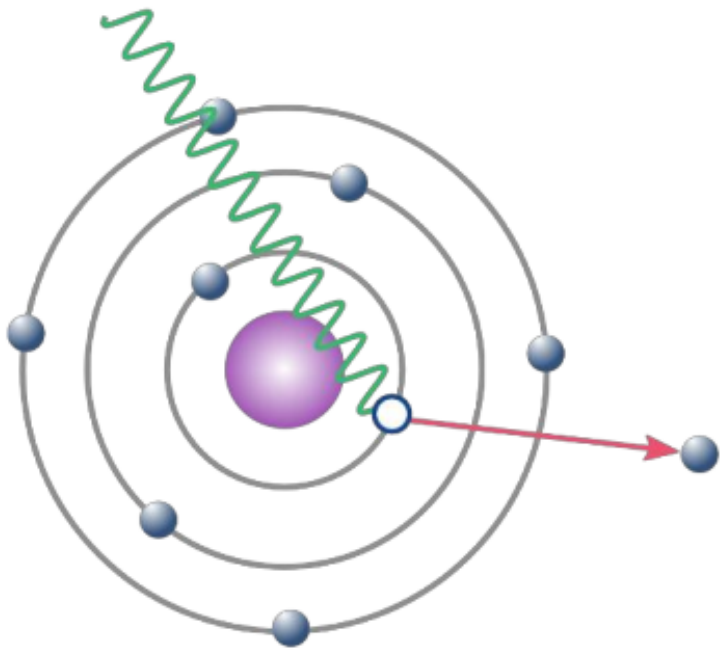

Figure 2.8.: Principle of the photoelectric effect: The squiggly line represents an incident photon, that stimulates emission of an electron. Picture courtesy of A. Regoutz, Imperial College.

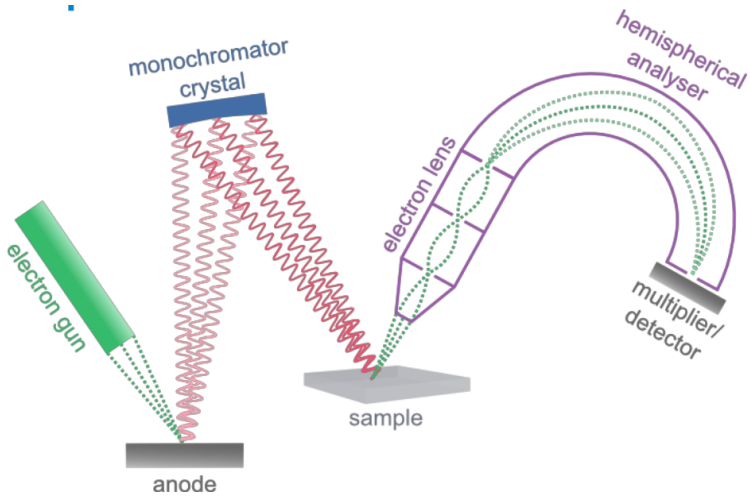

Figure 2.9.: Schematic setup of an XPS experiment. Picture courtesy of A. Regoutz, Imperial College.

- **Sample**: When using XPS the sample surface needs to be very clean, since the depth resolution is about 5 nm which corresponds to a maximum depth of about 15 atomic layers. This is usually achieved by evacuating the sample and sputtering off a few layers. In the case of

HAXPES the sample preparation is not that important since the depth resolution can reach up to 50 nm (see Fig. 2.10).

- **Detector**: State of the art are hemispherical detectors that disperse the electrons as a function of their kinetic energy. This detector has a work function, ϕ, so formula Eq. 2.36 needs to be amended:

$$E_k = h\nu - E_B - \phi.$$

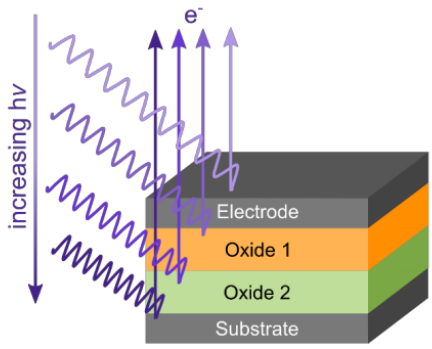

Figure 2.10.: Schematic of the superior depth resolution HAXPES has when compared to XPS. Picture courtesy of A. Regoutz, Imperial College.

3. Computational and Experimental Method

3.1. Computational Method

3.1.1. General

The DFT calculations within this thesis are performed with the Vienna Ab Initio Simulation Package (VASP) code [6–9], using the projector augmented wave (PAW) formalism [51] and the GGA-PBE exchange potential [31]. We use Methfessel-Paxton smearing [52]. Ionic relaxation was performed to reduce the residual forces to less than $1 \times 10^{-2}\,\mathrm{eV/Å}$ for energy calculations and $1 \times 10^{-8}\,\mathrm{eV/Å}$ for vibrational calculations.

Analysis, broadening and weighting of the calculated densities of state was done with GALORE [53] developed by UCL. The generation and visualization of structures was done using the VESTA software [36], phonon calculations were set up and analysed using homemade python code and phonopy [54].

Finally the climbing image nudged elastic band (CINEB) calculations were set up using the Vasp Transition State Toolkit (vtst) of the University of Texas [55, 56]. The grain boundary under investigation was obtained through SegroCalc [10].

The computational results presented have been achieved in part using the Vienna Scientific Cluster 2 (VSC2), on which the work shown in this thesis consumed approximately $300\,000\,\mathrm{core} - \mathrm{h}$.

3.1.2. Relaxation

The energies obtained through DFT calculations, e.g. Eq. 2.17, are, by means of the ionic contribution, susceptible to ionic displacements. Moreover, there are forces exerted on the ions, which in turn lead to movements towards the

equilibrium structure (see Eq. 2.8[1]). Usually the experimentally obtained lattice parameter is a good initial guess, however the approximations in the exchange functional tend to change the computational equilibrium lattice by a few percent. There are two ways to relax towards this equilibrium, either by using the VASP integrated cell-volume relaxation by setting $ISIF = 3$ in the INCAR file, or by manually varying the lattice parameter[2]. Although the first method seems to be convenient, it has some caveats. Due to the finiteness of the plane wave basis set used, an isotropic error, called Pulay stress, is introduced to the diagonal elements of the stress tensor. The second issue arises from the change in volume during one VASP run, which is not reflected in the set of basis wavefunctions thus requiring a second relaxation run using the result of the first one. To circumvent this the second method is employed, where the lattice parameter, i.e. the volume, is varied by a script and only ionic relaxation ($ISIF = 2$) is done by VASP. This yields a list of energies with corresponding volumes, which are most commonly fitted by the Birch-Murnaghan equation of state (BMEOS, [58]):

$$E(V) = E_0 + \frac{9V_0B_0}{16}\left\{\left[\left(\frac{V_0}{V}\right)^{\frac{2}{3}} - 1\right]^3 B_0' + \left[\left(\frac{V_0}{V}\right)^{\frac{2}{3}} - 1\right]^2 \left[6 - 4\left(\frac{V_0}{V}\right)^{\frac{2}{3}}\right]\right\}, \tag{3.1}$$

where one conveniently also receives the Bulk modulus, $B_0 = -V\left(\frac{\partial P}{\partial V}\right)_{P=0}$ and its derivative $B_0' = \left(\frac{\partial B}{\partial P}\right)_{P=0}$. The minimum energy structure is the one used for calculations.

3.1.3. Nudged - Elastic Band

The climbing image nudged elastic band (CINEB, [55]) method is employed for finding the minimum energy path (MEP) between an initial and final state of a transition as seen in e.g. Fig. 2.6. In elastic band methods, several states of the system (called images), linked together with zero-length springs are used. With nebmake.pl of vtst N intermediate images interpolating between the initial and final state are created.

In contrast to the classical NEB, the distance between the images is regulated by variable spring constants and, more importantly, one of the images is forced up the elastic band, so it reaches the highest saddle point. Through this mechanism the kinks commonly found in the classic elastic band method can be avoided and one arrives at a very good estimation of the saddle point which corresponds to the transition state [55].

[1] Although within VASP these forces are calculated by the means of the Hellmann-Feynman Theorem, see e.g. [57]

[2] and for hcp cells the c/a ratio as well

3.1.4. Phonon Calculations

For phonon calculations density functional perturbation theory (DFPT) as implemented in VASP is utilized. The analysis is done by phonopy which is an efficient python code linking the atomistic results to macroscopic thermodynamic properties. This link is found in the partition function of statistical mechanics:

$$Z = \exp\left(-\frac{\phi}{k_B T}\right) \prod_{\vec{q}\nu} \frac{\exp\left(-\frac{\hbar\omega(\vec{q}\nu)}{2k_B T}\right)}{1 - \exp\left(-\frac{\hbar\omega(\vec{q}\nu)}{k_B T}\right)}, \tag{3.2}$$

where $\vec{q}$ is the wave vector and ν the frequency of the phonon and ϕ an (arbitrary) energy zero-point. As is well known from thermodynamics Eq. 3.2 can be used to derive an expression for the entropy S:

$$S^{th} = -\left(\frac{\partial F}{\partial T}\right)_V = \left(\frac{\partial k_B T \ln Z}{\partial T}\right)_V,$$

$$S^{th} = \frac{1}{2T} \sum_{\vec{q}\nu} \hbar\omega(\vec{q}\nu) \coth\left(\frac{\omega(\vec{q}\nu)}{2k_B T}\right) - k_B \sum_{\vec{q}\nu} \ln\left[2\sinh\left(\frac{\omega(\vec{q}\nu)}{2k_B T}\right)\right], \tag{3.3}$$

providing the necessary link to Eq. 2.29.

3.1.5. Convergence of Results

Densities of State

Convergence studies regarding the energy cut-off and the density of the mesh in k-space, were done for tungsten (Fig. 3.1a), titanium (Fig. 3.1b) and copper (Fig. 3.1c) separately. A cut-off energy of 380 eV and a $22 \times 22 \times 22$ mesh in k-space was chosen for the primitive cell. Note that the mesh is rescaled depending on the size of the supercell in accordance with common practice (see for example the VASP workshop), e.g. for a $2 \times 2 \times 2$ supercell, the grid is $11 \times 11 \times 11$. Further the equilibrium lattice constant was determined using Eq. 3.1.

Diffusion

The convergence of the vacancy formation enthalpy, Eq. 2.28, (representative of the other, computationally more expensive parameters) was tested with respect to the following parameters:

- energy cut-off,

- density of grid in reciprocal space.

It was found that a relatively low energy cut-off ($ENCUT = 200\,\text{eV}$) provides the necessary accuracy, whereas the reciprocal grid had to be dense ($KPOINTS = 9 \times 9 \times 9$), as is depicted in Fig. 3.2. The minimal necessary size of the supercell was determined to be $N = 54$. While the formation enthalpy did already converge with $N = 27$, the presence of impurity atoms necessitated a larger cell. Again, the equation of state Eq. 3.1 was used to determine the equilibrium lattice constant.

3.1.6. Analysis of DFT Results

With increasing supercell size, the results of DOS calculations tend to be afflicted by intense noise, as can be seen in Fig. 3.3. The cause of this effect is unknown to the author, though is presumed to be a numerical artifact. The possibility of this increase in noise being due to the common practice of scaling the number of points in momentum space reciprocally to the volume of the cell (i.e. $a^3 : 22 \times 22 \times 22 \rightarrow (2a)^3 : 11 \times 11 \times 11$) was proven wrong: The 8 atom cell, which already experiences this phenomenon was calculated with a $22 \times 22 \times 22$ mesh, identical to the 1 atom cell. To counteract this the DFT results were analyzed using the GALORE tool developed by the University College London (UCL). The tool automatically shifts the point of origin to the Fermi energy, incorporates the cross-sections and applies a Gaussian and (if required) a Lorentzian energy broadening, eliminating the noise and enabling comparison to the experimental results, which naturally have a limited energy resolution. If not indicated otherwise, the cross-section correction was applied for an X-ray energy of 1.5 keV. Due to the experimental energy resolution the Gaussian broadening is set to 300 meV. A comparison between raw data, broadened data and broadened data with correct crosssections for a W cell and 6 keV can be seen in Fig. 3.4.

3.2. Experimental Method

The XPS and HAXPES measurements were performed in the group of Dr. Anna Regoutz, Imperial College Research Fellow at the Faculty of Engineering, Department of Materials, Imperial College London, UK. Dr. Regoutz is also visiting scientist at the Diamond Light Source (DLS), the UK synchrotron.

3.2.1. XPS Experiments

The XPS measurements were performed on a standard laboratory XPS system. Monochromated Al-K_α radiation, at an energy of 1.5 keV, is used as the probing X-ray source. Through an initial survey, carried out with a rough increment of 500 meV, we defined the following regions of interest:

Region name	**Energy range** / eV	**Energy increment** / meV
Valence band	$-2 - 15$	50
Ti-2p	$450 - 475$	100
W-4f	$25 - 42$	100
C-1s	$278 - 295$	100
O-1s	$522 - 540$	100

Table 3.1.: The chosen energy ranges and corresponding states for the XPS experiment.

3.2.2. HAXPES Experiments

To achieve depth resolution, we performed HAXPES measurements which were carried out at the Diamond Light Source (DLS) in Didcot, UK at the I09 beamline with 6 keV monochromated X-rays. Again we defined regions of interest for these measurements by an initial survey scan:

Region name	**Energy range** / eV	**Energy increment** / meV
Valence band	$-8 - 12$	50
Ti-2p	$431 - 465$	50
W-4f	$22 - 37$	50
Ti-1s	$4950 - 4975$	100
O-1s	$519 - 535$	100

Table 3.2.: The chosen energy ranges and corresponding states for the HAXPES experiment.

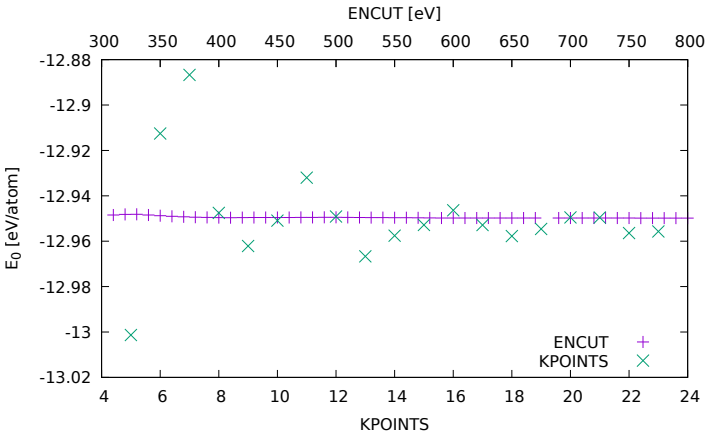

(a)

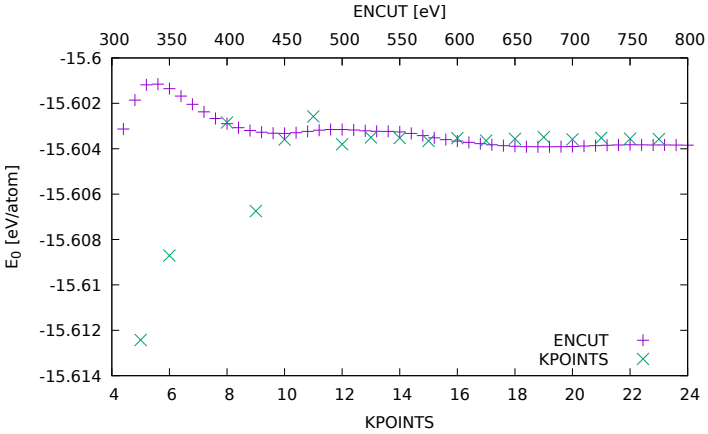

(b)

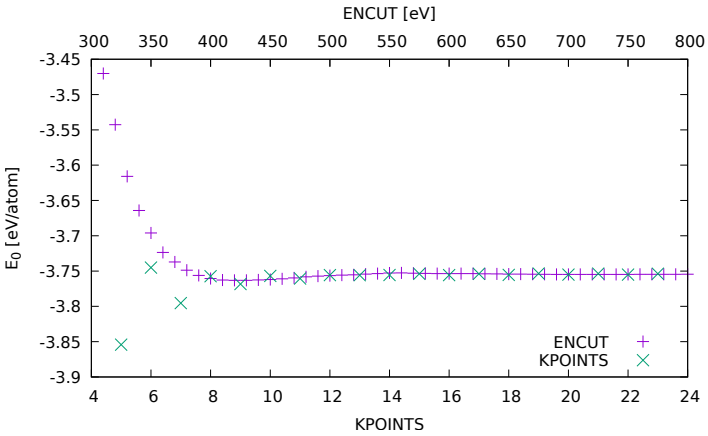

(c)

Figure 3.1.: Convergence studies for the elements used in this thesis. All performed on the primitive cell of the element. To reach the desired precision of 1 meV, the parameters were chosen as $ENCUT = 380\,\text{eV}$ and $KPOINTS = 22 \times 22 \times 22$.
Fig. 3.1a - tungsten, Fig. 3.1b - titanium and Fig. 3.1c - copper.

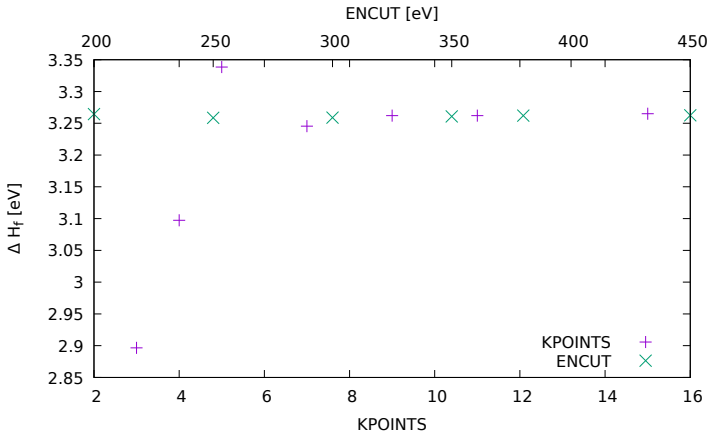

Figure 3.2.: Convergence study of the formation enthalpy Eq. 2.28 of tungsten vacancies. The strong dependence on k-mesh density is clearly visible, whereas the cut-off energy can be chosen very low.

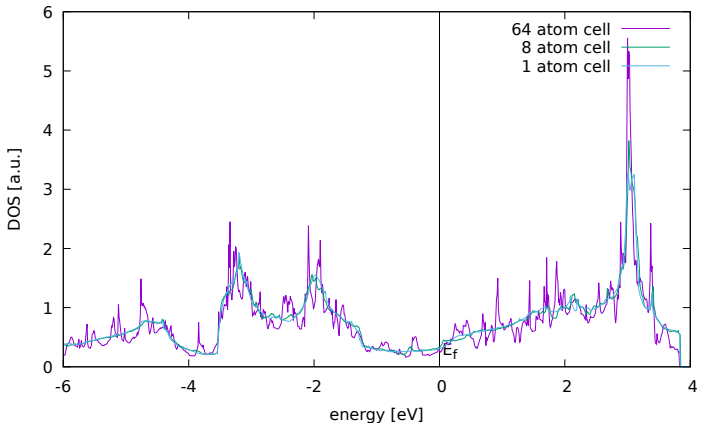

Figure 3.3.: The increase of noise in the density of states of bcc-W with increasing supercell size (1/8/64 atoms).

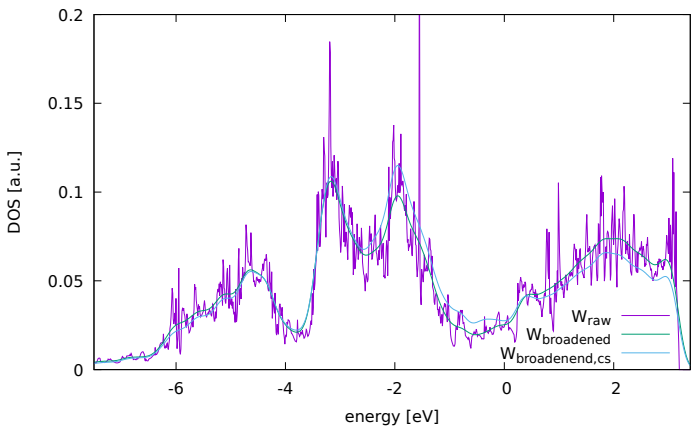

Figure 3.4.: The effect of the applied 300 meV gaussian broadening and the effect of the cross-section for 6 keV X-ray energy.

4. Results and Discussion

4.1. Equilibrium Lattice Parameter

Following the procedure outlined in Section 3 we perform calculations for W, Ti and Cu for various lattice parameters and plot the resulting energy as a function of the volume. After fitting Eq. 3.1 to the obtained data, we can deduce the equilibrium volume and thus the equilibrium lattice parameter. This procedure is shown in Figures 4.1a to 4.1c. Together with experimental results the outcomes are displayed in Tab. 4.1. As can be seen the agreement is very good. The slight deviations on the sub-Ångström scale can be accounted for by considering two facts:

- Firstly, the samples tested in the experiments are not as uniform as our structures.
- Secondly, the choice of the pseudopotential and the approximations done in their derivation also introduce a systematic error.

Element	**Method**	**Lattice Parameter / Å**	**Reference**
W	DFT, PBE	3.186	this work
W	XRD	3.155 ± 0.001	[59]
W	XRD	3.1646	[60]
W	DFT	$3.12 - 3.16$	[61]
Cu	DFT, PBE	3.632	this work
Cu	XRD	3.597 ± 0.004	[59]
Cu	XRD	3.615	[62]
Cu	DFT, PBE	3.661	[63]
Ti	DFT, PBE	$a = 2.934$, $c/a = 1.59$	this work
Ti	XRD	$a = 2.9504 \pm 0.003$, $c/a = 1.59$	[64]

Table 4.1.: Equilibrium lattice parameters of W, Cu and Ti from experiment and simulation in comparison with this work.

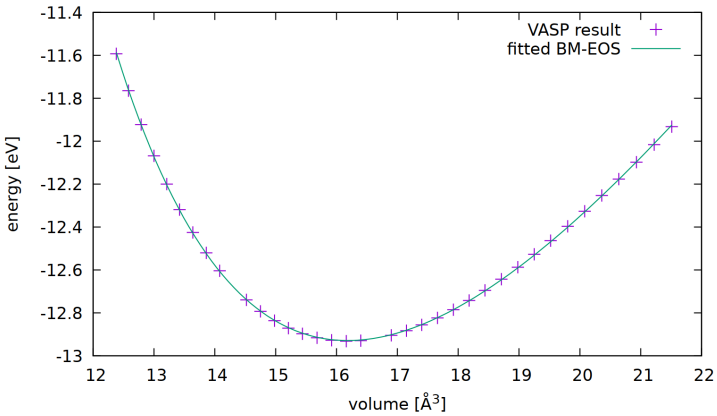

(a)

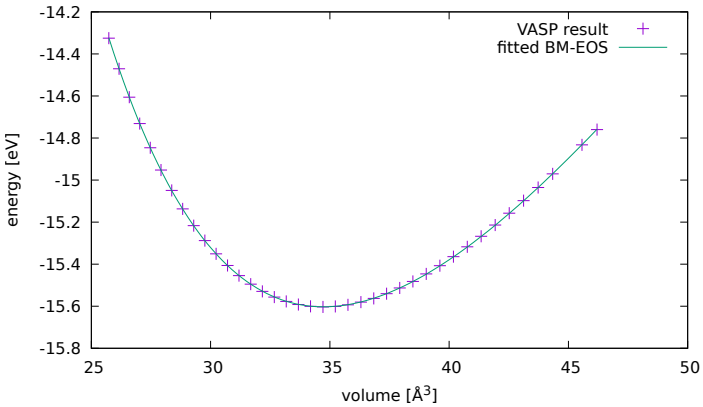

(b)

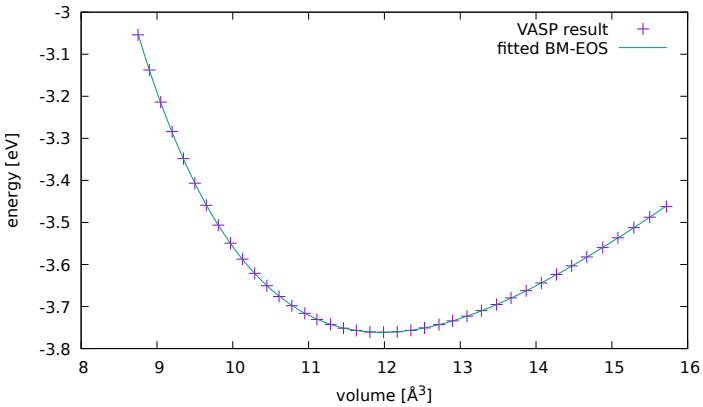

(c)

Figure 4.1.: Variation of volume to find minimum energy volume and thus equilibrium lattice constant of the tungsten (Fig. 4.1a), titanium (Fig. 4.1b) and copper (Fig. 4.1c) primitive cell using Eq. 3.1. The results are shown in Tab. 4.1.

4.1.1. Relation of Lattice Parameter and Ti-Content

The effect that titanium doping has on the tungsten lattice constant was tested using SQS with Ti concentrations ranging from 12.5 at% to 87.5 at%. It was found that in the range < 40 at% the lattice constant does not change significantly. However, the slight changes that do happen, are visible in the density of state, as will be discussed below. The result is depicted in Fig. 4.2. This is quite surprising, as a Vegard-like [65] behavior, that is a linear relationship between volume and impurity concentration, was expected. We, however, see the onset of this only after a Ti concentration of about 30 at%.

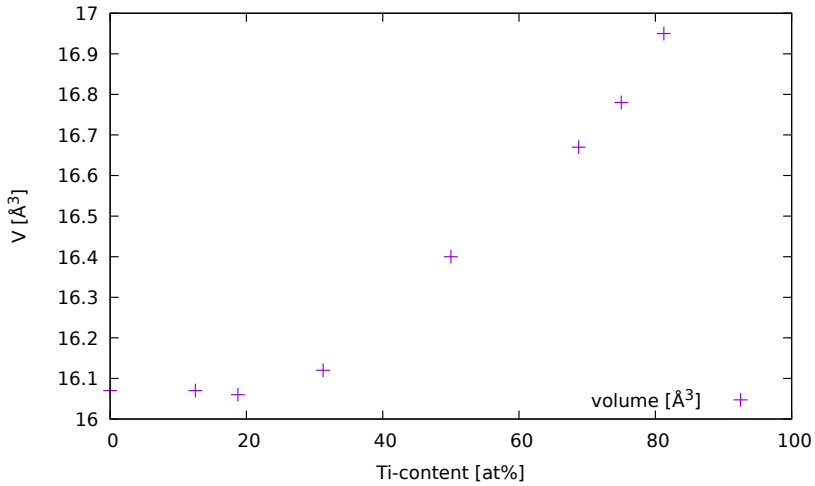

Figure 4.2.: Equilibrium volumes of tungsten SQS with varying Ti content, exhibiting non-Vegard behavior.

4.2. Electronic Structure

4.2.1. Analyzed Cells and Samples

DFT Input

The input structures for the DFT calculations were chosen based on three goals:

1. Determine if titanium clustering in either the bulk or the GB is energetically favorable over the other and assess the energetic stability of the structures.

2. Determine if there are differences between Ti in the GB and in bulk W that are visible in the electronic structure. These differences could then be used in combination with the experimental data and the energetic considerations to gain an understanding of the position of the Ti atoms in the diffusion barrier. Thus 16 structures were identified, that are depicted in Figures 4.3 to 4.5 and tabulated in Tab. 4.2. The Σ3 GB was chosen, as a recent publication showed that it is energetically the most favorable [10].

3. Determine the impact different Ti concentrations have on the electronic structure. Thus, several SQS, as depicted in Fig. 4.5, were analysed.

The nomenclature of the structures is displayed in Tab. 4.2.

Name	**Figure**	**# Ti atoms**	**# W atoms**
B1	Fig. 4.3a	1	127
B2	Fig. 4.3b	2	126
B3	Fig. 4.3c	3	125
B4	Fig. 4.3d	4	124
B5	Fig. 4.3e	9	119
B6	Fig. 4.3f	27	101
G1	Fig. 4.4a	1	71
G2	Fig. 4.4b	1	71
G3	Fig. 4.4c	1	71
G4	Fig. 4.4d	2	70
G5	Fig. 4.4e	3	69
G6	Fig. 4.4f	12	48
S1	Fig. 4.5a	2	14
S2	Fig. 4.5b	3	13
S3	Fig. 4.5c	4	12
S4	Fig. 4.5d	5	11

Table 4.2.: Summary of input structures for the DFT calculations.

(HA)XPES Samples

The samples were produced by sputtering 300 nm of Ti-W on a Si substrate coated with 100 nm of SiO_2. The Ti concentration varies between 11.4 at% to 26.9 at%. The samples under examination were subject to two different anneals, as well as one as deposited sample. This leaves us with a total of 12 samples, summarized in Tab. 4.3.

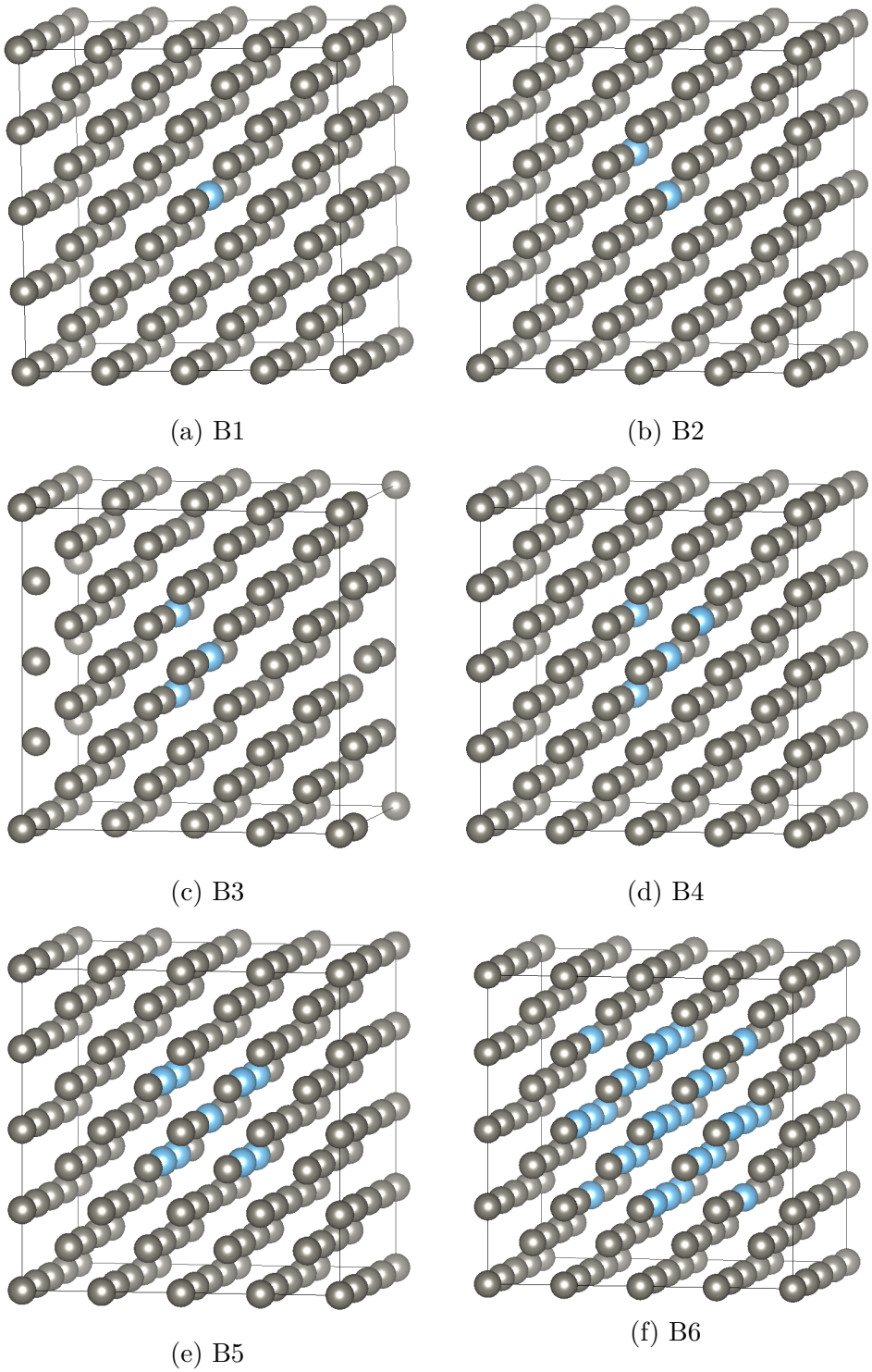

Figure 4.3.: The W bulk structures analyzed in this thesis, containing an increasing number from one (Fig. 4.3a) to 27 (Fig. 4.3f) Ti atoms, clustered together. The naming convention is shown in Tab. 4.2.

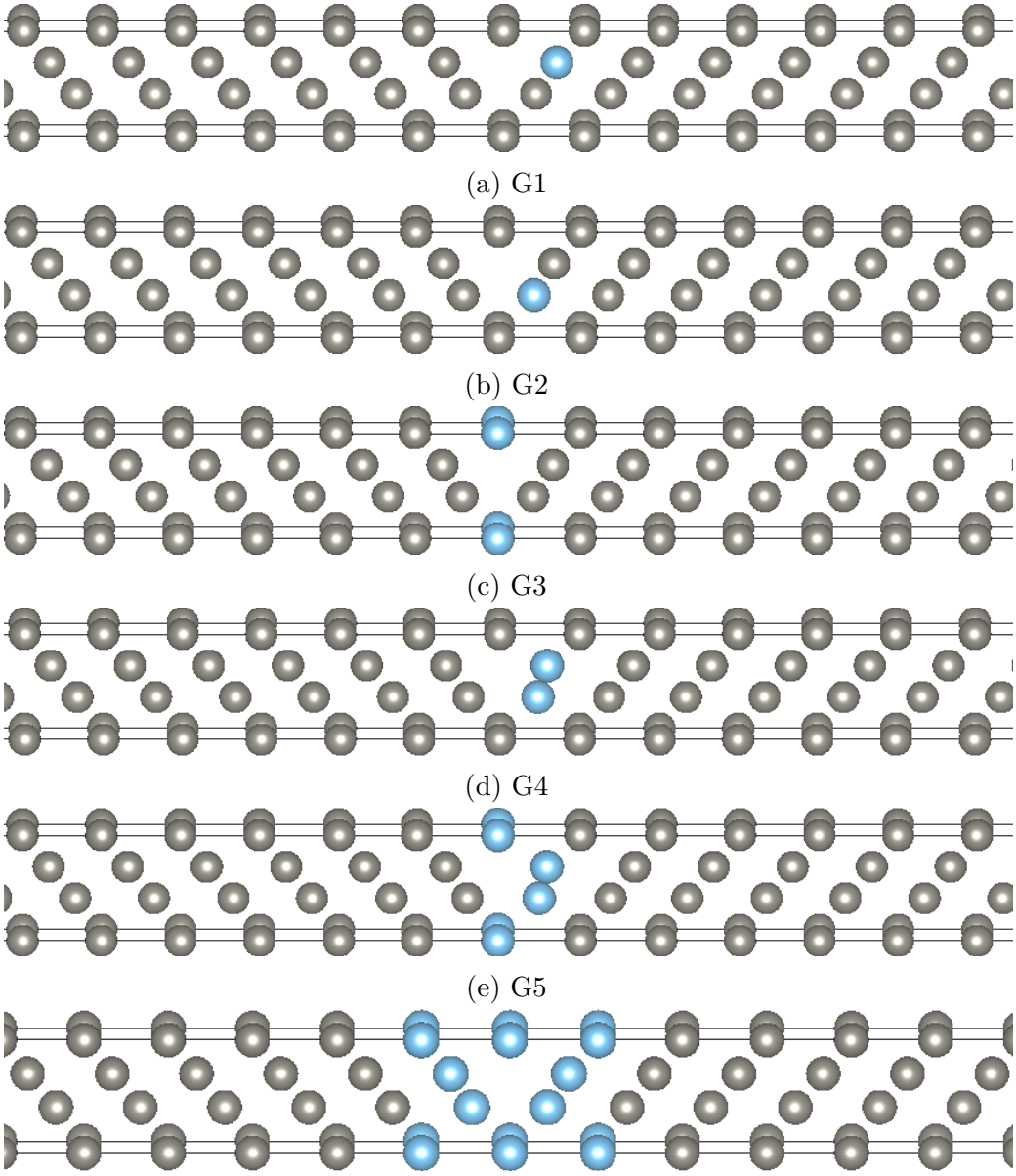

(a) G1

(b) G2

(c) G3

(d) G4

(e) G5

(f) G6

Figure 4.4.: The W Σ3 grain boundary structures analyzed in this thesis, containing Ti at site 35 (Fig. 4.4a), 36 (Fig. 4.4b), 37 (Fig. 4.4c) and clustered at sites 35 and 36 (Fig. 4.4d), at 35, 36 and 37 (Fig. 4.4e) and with a concentration of 20% (Fig. 4.4f). The naming convention is shown in Tab. 4.2.

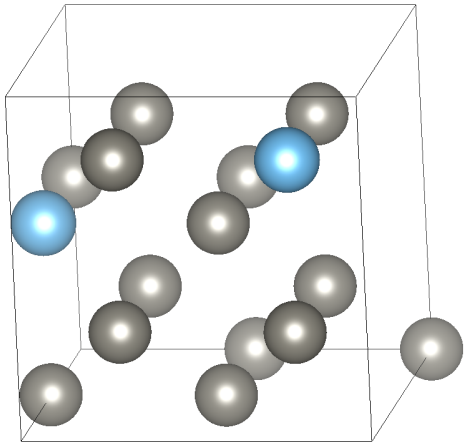

(a) S1

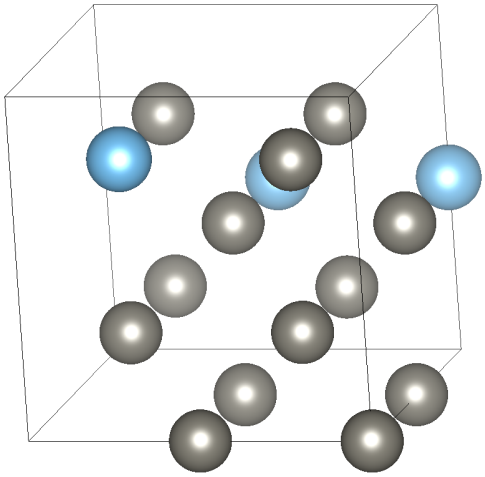

(b) S2

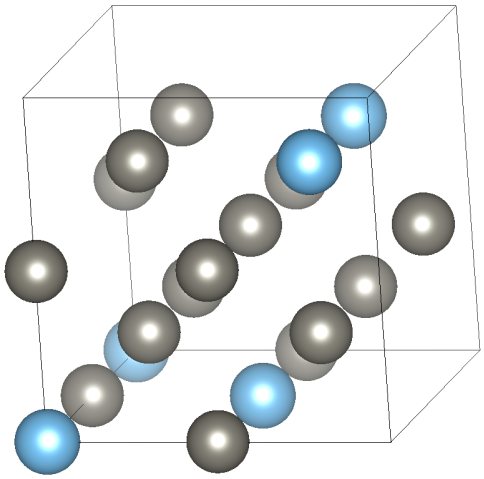

(c) S3

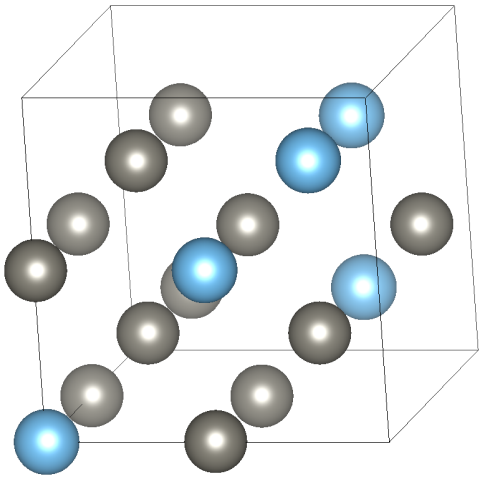

(d) S4

Figure 4.5.: SQS with varying Ti concentration: Fig. 4.5a: $W_{0.875}Ti_{0.125}$, Fig. 4.5b: $W_{0.8125}Ti_{0.1875}$ and Fig. 4.5d: $W_{0.6875}Ti_{0.3125}$. The naming convention is shown in Tab. 4.2.

Sample Identifier	**Ti content** / at%	**Annealing parameters**
2A	26.9	no anneal
2B	26.9	anneal > 300 °C
2C	26.9	10× longer anneal > 300 °C
4A	22.1	no anneal
4B	22.1	anneal > 300 °C
4C	22.1	10× longer anneal > 300 °C
6A	17.6	no anneal
6B	17.6	anneal > 300 °C
6C	17.6	10× longer anneal > 300 °C
8A	11.4	no anneal
8B	11.4	anneal > 300 °C
8C	11.4	10× longer anneal > 300 °C

Table 4.3.: Summary of Ti-W samples.

4.2.2. Results

Enthalpies of Formation

The energy per atom of the structures Figures 4.3 to 4.5 is depicted in Fig. 4.6. As can be seen the addition of Ti increases the structural energy, this is an indicator of the increased interaction energies in the system, which can be a result of the structural discrepancies of the bcc W and the hcp Ti. The found linearity is possibly caused by the relative weak Ti-Ti and Ti-W interactions, when compared to the pure W metal.

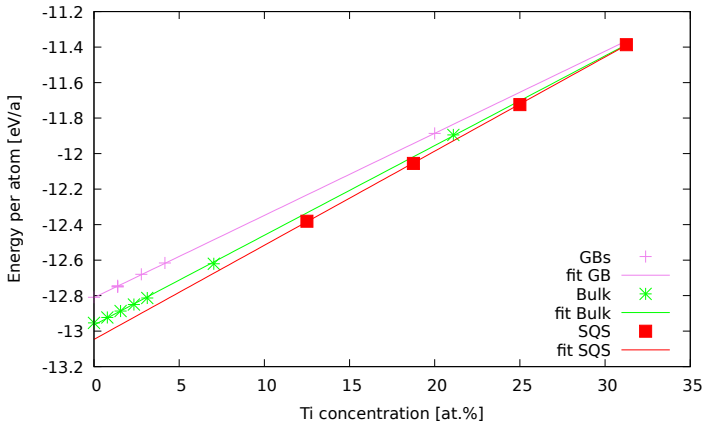

Figure 4.6.: The energy per atom for the structures depicted in Figures 4.3 to 4.5. To guide the eye linear fits were performed that fit the data well.

Expanding on a concept introduced in Chapter 2 allows us to assert the stability of the compounds.

In analogy to Eq. 2.28 we can define the enthalpy (or heat) of formation of a compound (A_nB_m) by the energies of its constituents (E_A, E_B) and the total energy of the compound $E_{A_nB_m}$,

$$\Delta H_f = E_{A_nB_m} - nE_A - mE_B. \tag{4.1}$$

In Fig. 4.7 the results of Eq. 4.1 per atom is depicted. Most noteworthy is the fact that the heats of formation are all positive, i.e. energy is needed to create the structures. Typically such compounds are metastable or unstable and tend to exhibit phase separation [66, p. 59], especially when subjected to external forces such as stress, high temperatures or electric fields. A comprehensive study on ball-milled Ti-W compounds did indeed find indications of phase separations and the results of the XPS analysis show similar structural changes as will be discussed in the next part. [67].

When looking at the enthalpy of formation per additional Ti atom, the GB structures exhibit an interesting behaviour as is shown in Fig. 4.8. While

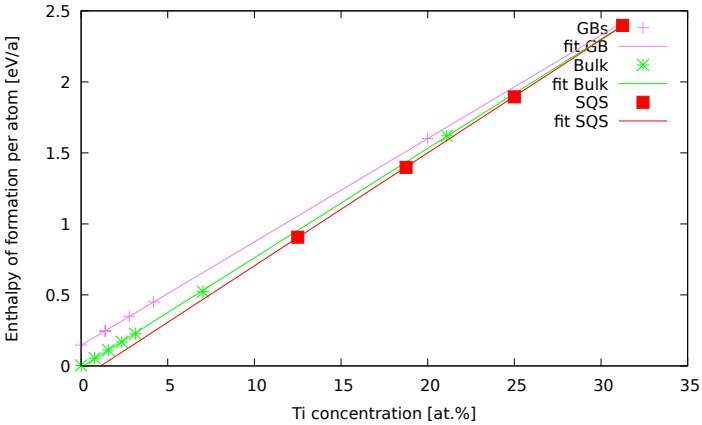

Figure 4.7.: The heats of formation for the structures depicted in Figures 4.3 to 4.5. To guide the eye linear fits were performed that fit the data well.

the results for the SQS and the bulk structures are very similar and linearly increasing, the energies of the GB structures decline with a x^{-1} power law when adding Ti atoms, up to a point of about 20 %, where SQS, bulk and GB structures experience a similar enthalpy of formation per Ti atom of approximately 8 eV. This is presumably caused by forming of surface state in the low Ti concentration GB structures. Only in higher concentrations interactions with the bulk can take place, which leads to a decrease in energy. The results suggest that low Ti concentration grain boundary structures are

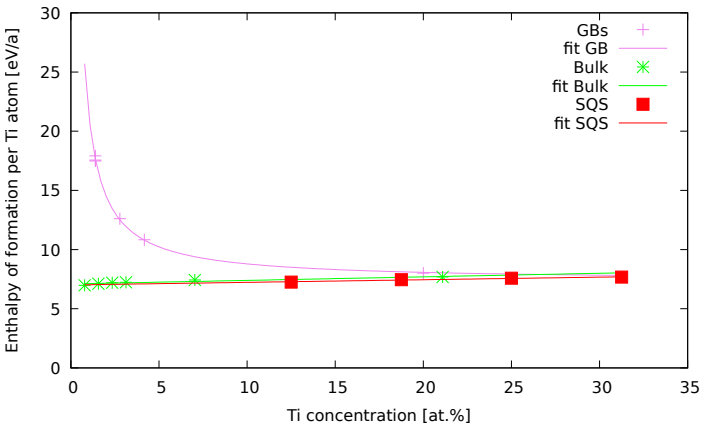

Figure 4.8.: The heats of formation per Ti atom for the structures depicted in Figures 4.3 to 4.5. The SQS and bulk structures are well described by linear fits but the GB structures experience an x^{-1} power law decrease.

unstable, whereas relatively high concentrations, above 20 % are energetically comparable to SQS and bulk structures.

Densities of State

The DOS is very dependent on local chemistry, e.g. neighboring atoms, the orbital overlaps and the chemical bonds. Thus we see distinctive features of the Ti-projected DOS in Figs. 4.9 and 4.10, such as the width of the first peak just below E_f and the intricate peak structures in $[-4, -2]$eV, that would theoretically allow a distinction of the structures with Ti in the grain boundaries or in bulk. However, this data is experimentally not (easily) available. While there are means, such as resonant XPS, such experiments were unavailable. Thus we can only compare to the full DOS obtained by the XPS analysis.

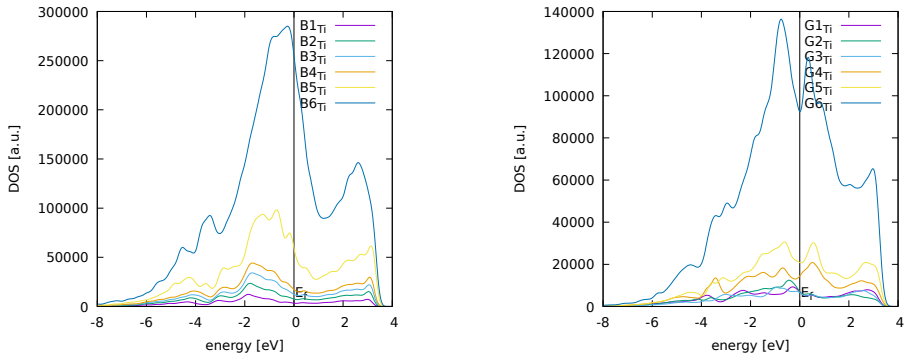

(a) (b)

Figure 4.9.: The Ti projected DOS of structures B1-B6 and G1-G6 depicted in Figs. 4.3 and 4.4.

When looking at the cross sections [68], σ_{Ti}, of Ti in comparison to those of W, σ_W, however, it can be deduced that the direct visibility of the Ti in the DOS will be negligible. For X-ray energies of 1.5 keV to 6 keV $\sigma_{Ti} \approx \frac{1}{3}\sigma_W$, thus seeing as the maximum concentration of Ti is 26.9 %, the expected impact of the Ti on the DOS is below 10 %, which can also be seen in Figures 4.13a to 4.13d, where it is shown that the greatest contribution stems from the W d-Orbital. This means that a direct identification of the Ti bulk or GB features in the experimental data will be hard to impossible, even for the high concentration structures, Figs. 4.3f and 4.4f. For a more detailed insight on this, the DOS of structures containing equal amounts of Ti are depicted in Fig. 4.11.

Nonetheless, we can analyze the impact of the Ti doping on the total DOS. Looking at the total densities of state of the SQS from Figs. 4.3 and 4.4 that are depicted in Fig. 4.12, we see next to no difference in the low concentration DOS. In the high concentration DOS however, a broadening and a loss of intensity of the very first peak below E_f of the bulk structure when compared to the GB structure can be seen, as well as an additional peak, where before

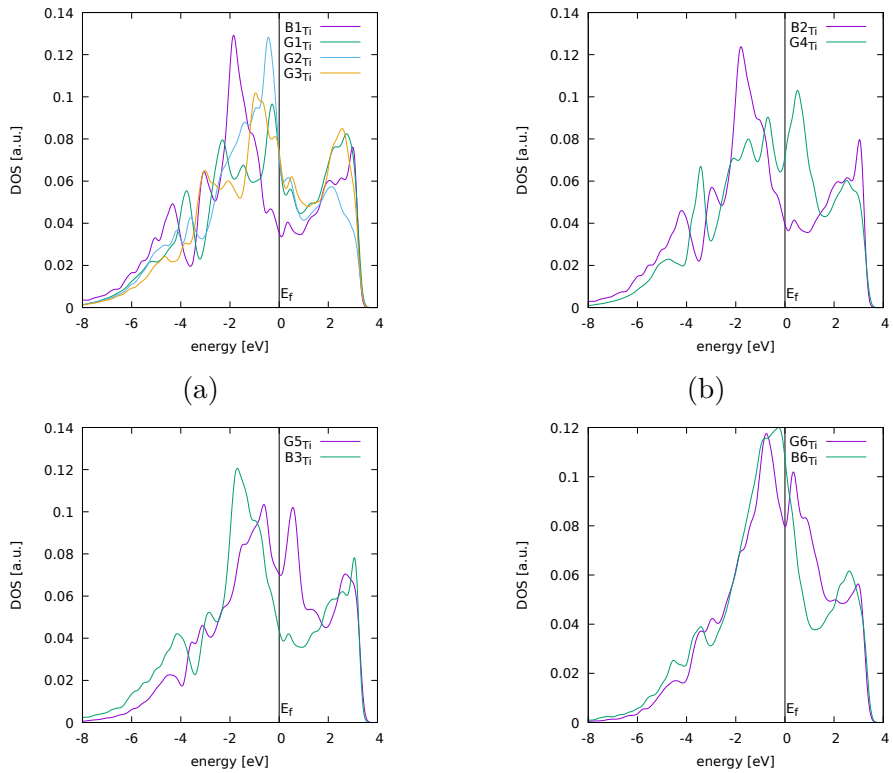

Figure 4.10.: Normalized Ti projected DOS of the structures containing one Ti atom (Fig. 4.10a, B1, G1-G3), two Ti atoms (Fig. 4.10b, B2, G4), three Ti atoms (Fig. 4.10c, B3, G5) and 20 at% Ti (Fig. 4.10d, B6, G6), as depicted in Figs. 4.3 and 4.4.

a minimum is found. These features are not visible in the HAXPES and XPS spectra depicted in Figs. 4.15 and 4.16, either because they were smeared out by e.g. temperature effects, or because the measured structures were simply too disordered to exhibit them. In Fig. 4.14 the densities of state for the SQS are depicted. It can be seen that the first area containing peaks below the Fermi energy E_f, i.e. $[-3, 0]$eV, is becoming less pronounced, whereas the second area, i.e. $[-5, -3]$eV, remains at a similar intensity. This can also be seen in the experimental data in Figs. 4.17 and 4.18 and is possibly caused by the increased interaction energy due to the higher Ti concentration, which we saw in the energetic considerations, e.g. Fig. 4.7 as well. The increase in interaction energy steepens the band structure and thus the density of states decreases.

Further we see a broadening of the DOS with decreasing Ti concentration, this effect is likely due to the small change in volume that was discussed and depicted in Fig. 4.2.

Comparing Figs. 4.15 and 4.16 to Fig. 4.14, it can be deducted that annealing leads to an increase in Ti content on the surface, something that has already

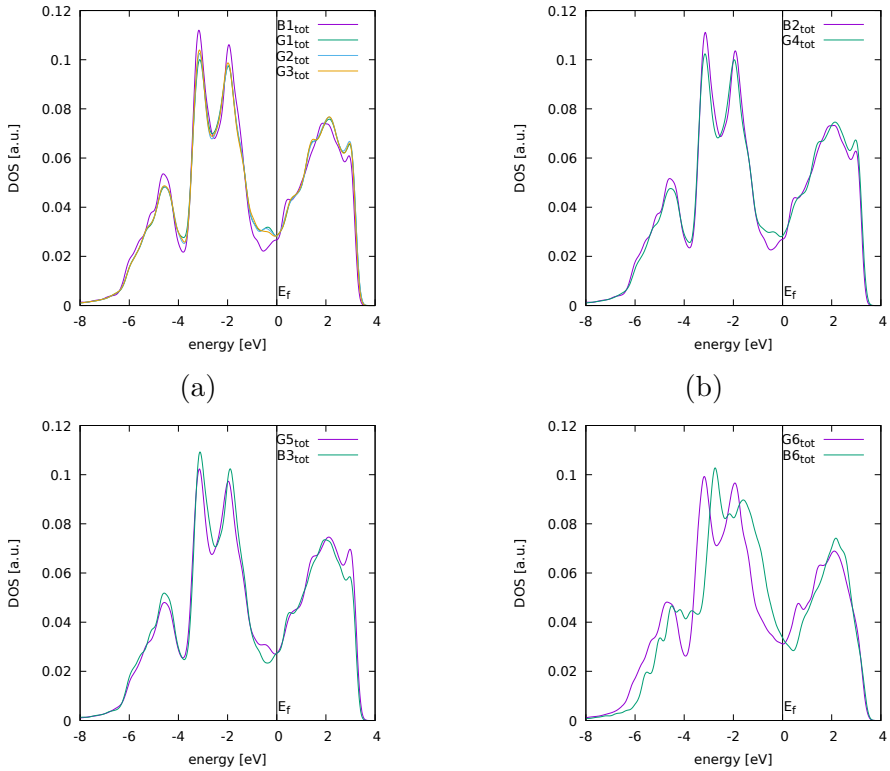

(a) (b) (c) (d)

Figure 4.11.: Normalized total DOS of the structures containing one Ti atom (Fig. 4.11a, B1, G1-G3), two Ti atoms (Fig. 4.11b, B2, G4), three Ti atoms (Fig. 4.11c, B3, G5) and 20 at% Ti (Fig. 4.11d, B6, G6), as depicted in Figs. 4.3 and 4.4.

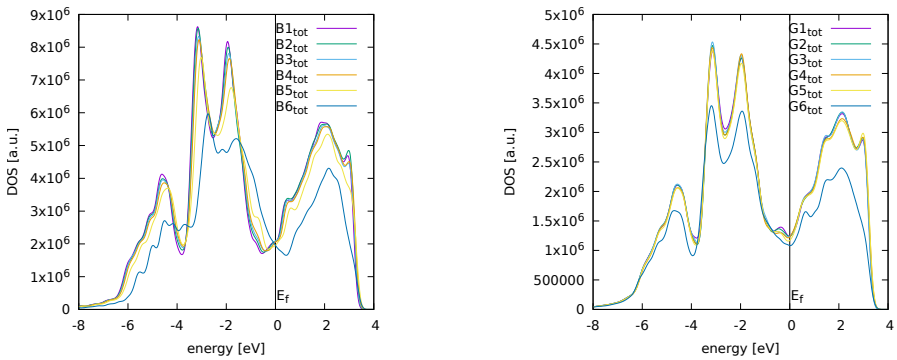

(a) (b)

Figure 4.12.: The total DOS of structures B1-B6 and G1-G6 depicted in Figs. 4.3 and 4.4.

been noted in literature as well [69, p. 55]. The effect is not as pronounced in Fig. 4.16 which is a consequence of the depth resolution of the hard X-rays. In his thesis, M. Fugger analyzed samples similar to ours, however they had an additional Cu layer on top of the Ti-W. He concluded that, when

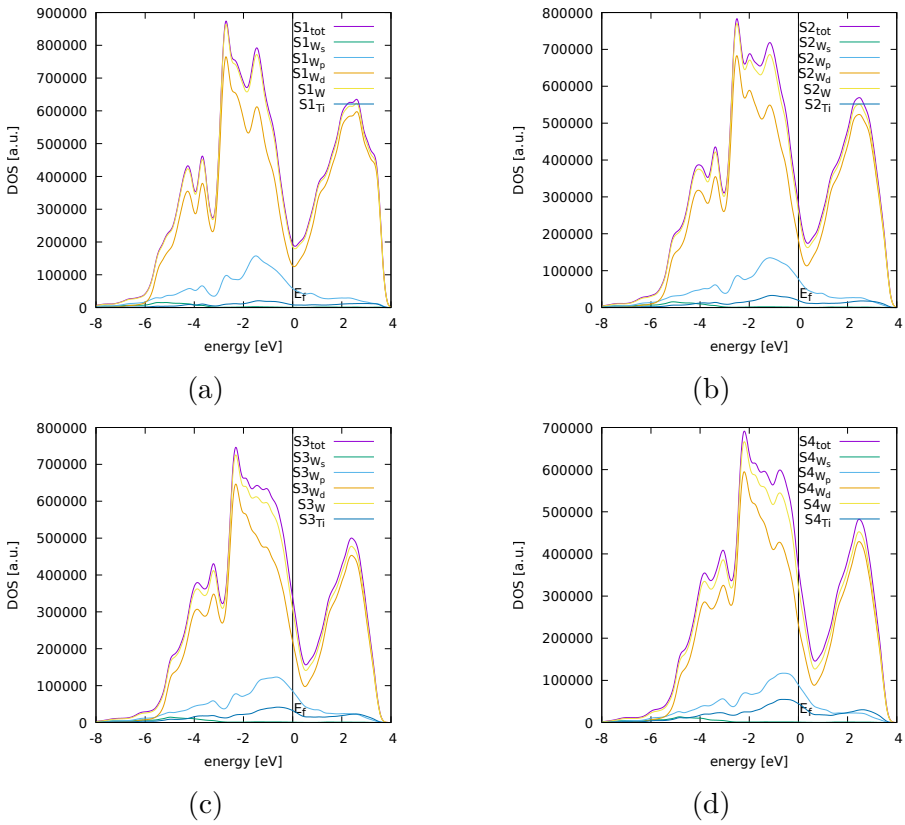

Figure 4.13.: DOS of the structures depicted in Fig. 4.5. Elemental decomposition shows the clear dominance of tungsten features, particularly the tungsten d-Orbital (shown in orange).

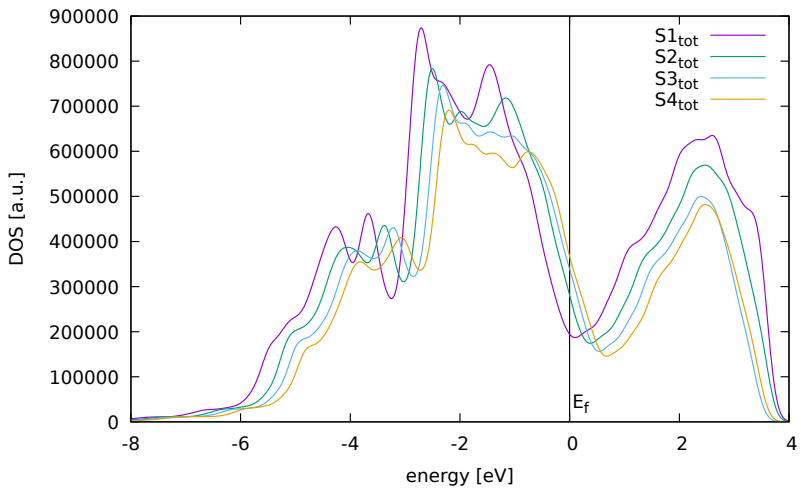

Figure 4.14.: The total DOS of the SQS depicted in Fig. 4.5 to visualize the impact of different Ti concentrations.

saturated, 27 % of Ti had went from the diffusion barrier into the copper and suspected grain boundary diffusion to be responsible [69, p. 42]. This can, theoretically, also be concluded from the core level spectra depicted in

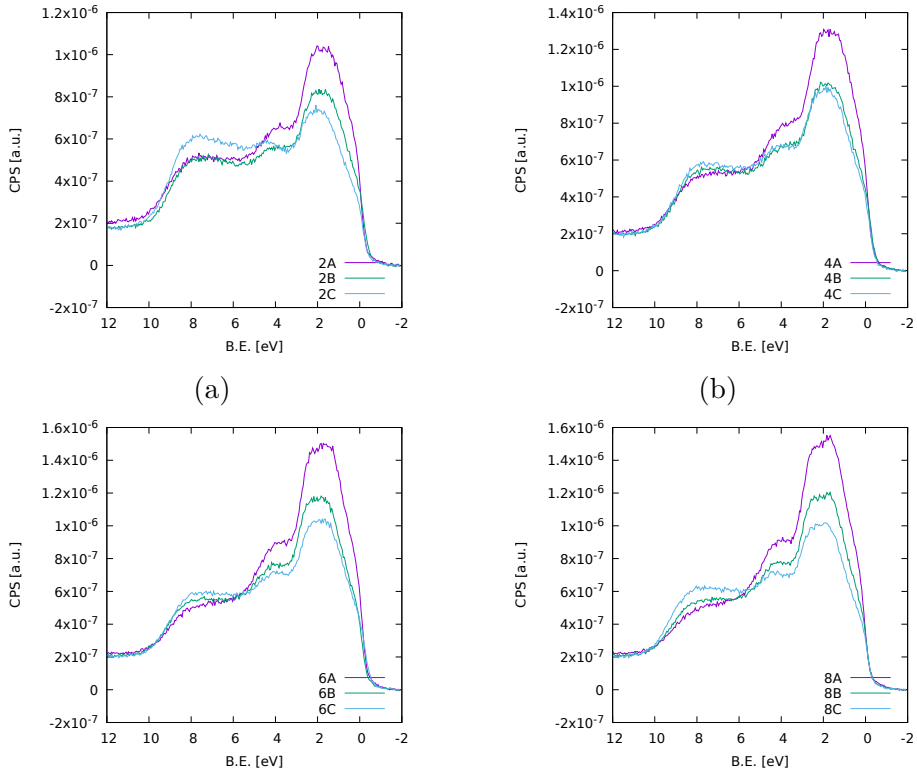

(a) (b) (c) (d)

Figure 4.15.: XPS measurements of the valence band of the different samples to visualize the effects of different anneals (increasing annealing time from A to C). Clearly the surface structure is affected significantly by annealing. Positive binding energies correspond to the negative energies in the computationally obtained DOS.

the Appendix. However, this was not the focus of this thesis and is thus postponed for future work. It should be noted that these are preliminary evaluations, more detailed analysis will be performed by Dr. A. Regoutz, however, the trends are not expected to change.

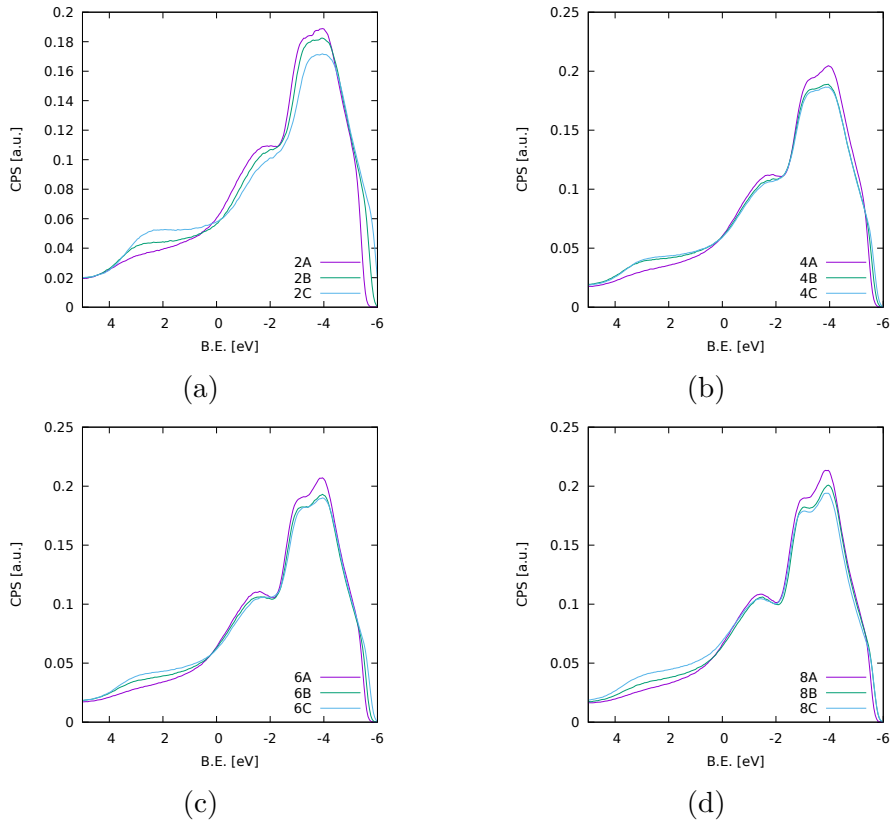

Figure 4.16.: HAXPES measurements of the valence band of the different samples to visualize the effects of different anneals (increasing annealing time from A to C). The bulk features are not as affected by annealing as the surface structure shown in Fig. 4.15. Positive binding energies correspond to the negative energies in the computationally obtained DOS.

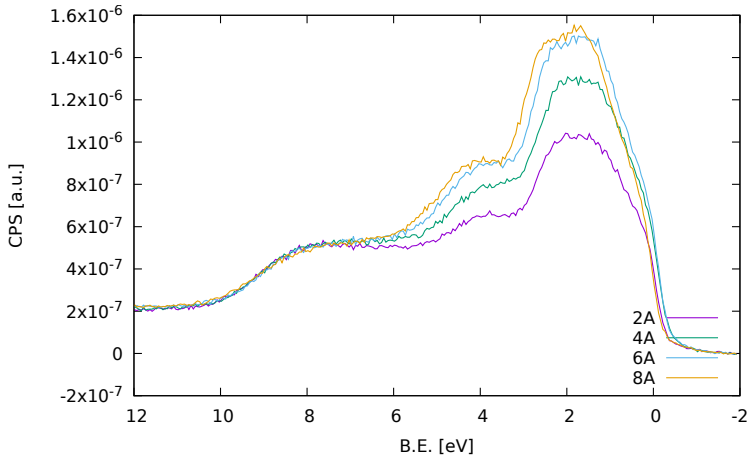

(a)

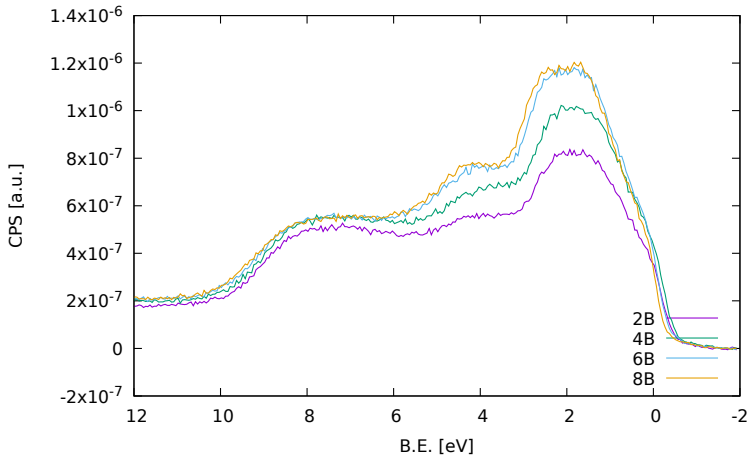

(b)

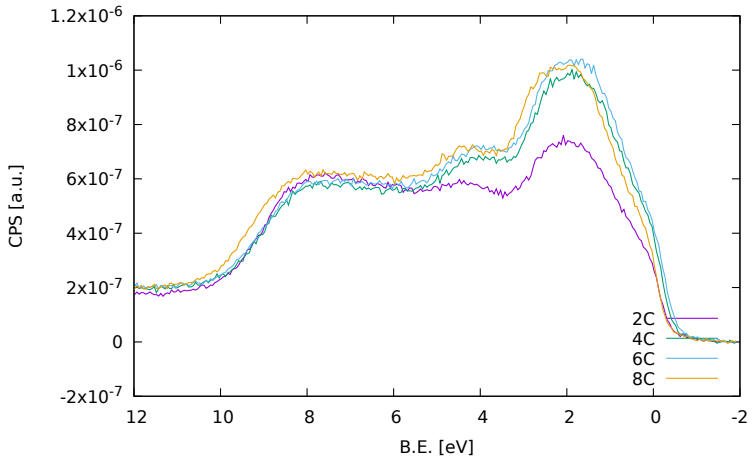

(c)

Figure 4.17.: XPS measurements of the valence band of the different samples to visualize the effects of different Ti concentrations (decreasing from sample 2 to 8). The decrease of the DOS at the first peak below the Fermi edge is clearly visible. Positive binding energies correspond to the negative energies in the computationally obtained DOS.

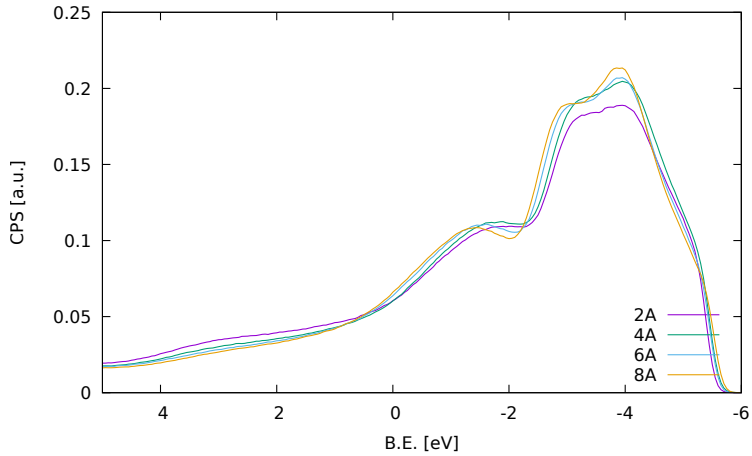

(a)

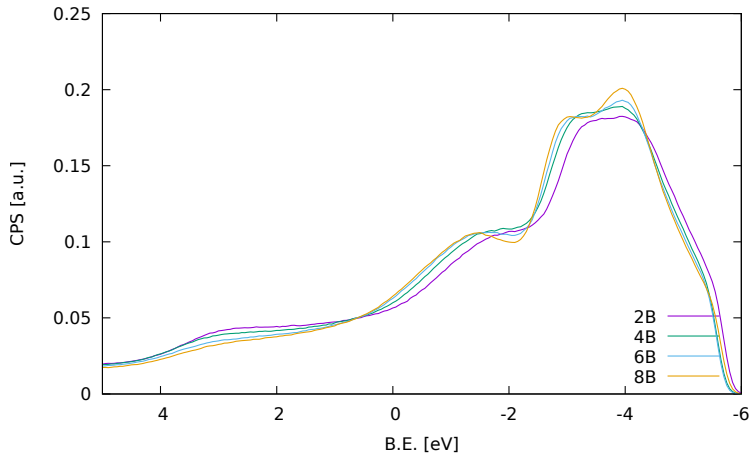

(b)

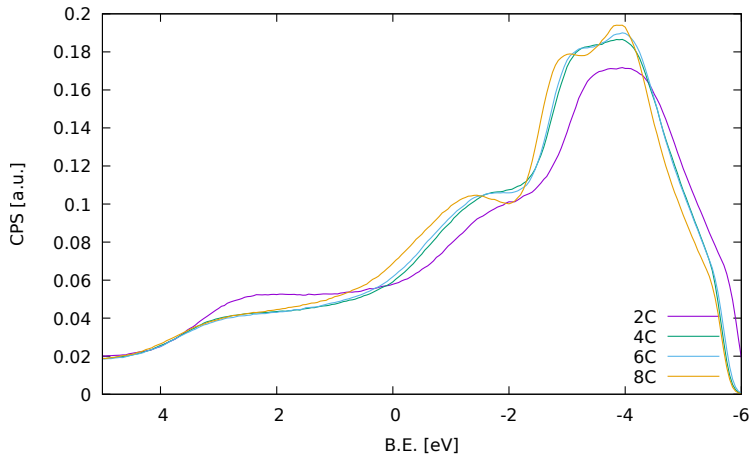

(c)

Figure 4.18.: HAXPES measurements of the valence band of the different samples to visualize the effects of different Ti concentrations (decreasing from sample 2 to 8). Decline of the first peak is not as pronounced due to difficult normalization of data. Positive binding energies correspond to the negative energies in the computationally obtained DOS.

4.3. Self-Diffusion of Tungsten

As was discussed in Section 2, we require the equilibrium lattice parameter, which we already obtained in the previous section, the vacancy concentration and the tracer jump frequency for determining the self diffusion coefficient.

4.3.1. Vacancy Concentration

After constructing the perfect and one-vacancy cells depicted in Figs. 4.19a and 4.19b the structures were allowed to relax ionically. Afterwards the total ground state energies were determined and, after insertion into Eq. 2.28, the formation enthalpy obtained. The results are depicted in Tab. 4.4. By

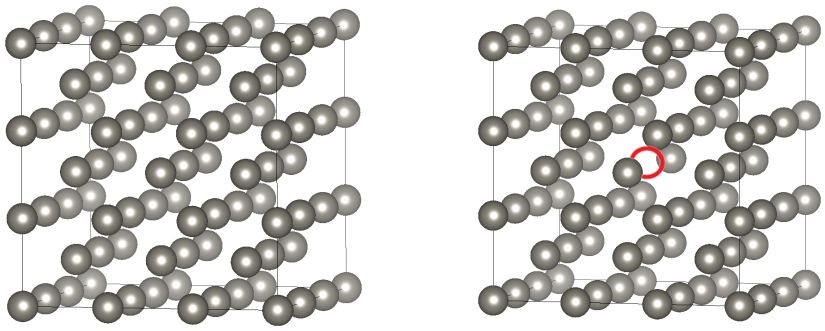

(a) (b)

Figure 4.19.: The two cells necessary for calculating the vacancy concentration. Fig. 4.19a is the perfect state, whereas Fig. 4.19b had one atom removed.

means of a DFPT calculation the phonon frequencies, i.e. the vibrational spectrum, was obtained. As can be seen in Figs. 4.20 and 4.21 the match with experiment and other calculations is, at least qualitatively, very good. Through Eq. 2.29 the vibrational entropies were obtained. Inserting both quantities in Eq. 2.27 yields the equilibrium vacancy concentration as a function of temperature which is depicted in Fig. 4.22. While the fit of the simulation data with the experiments mentioned in Tab. 4.4 is not perfect, it should be noted that the experimental results show a significant spread, indicating that the sample quality plays a major role in determining the formation energy and entropy. Another very important factor is that tungsten is, generally speaking, a nanocrystalline material and the behaviour at the grain boundaries does not necessarily reflect that of the bulk. In experiment it is expected that bulk and grain boundaries are mixed, whereas in the simulation just the bulk structure is considered.

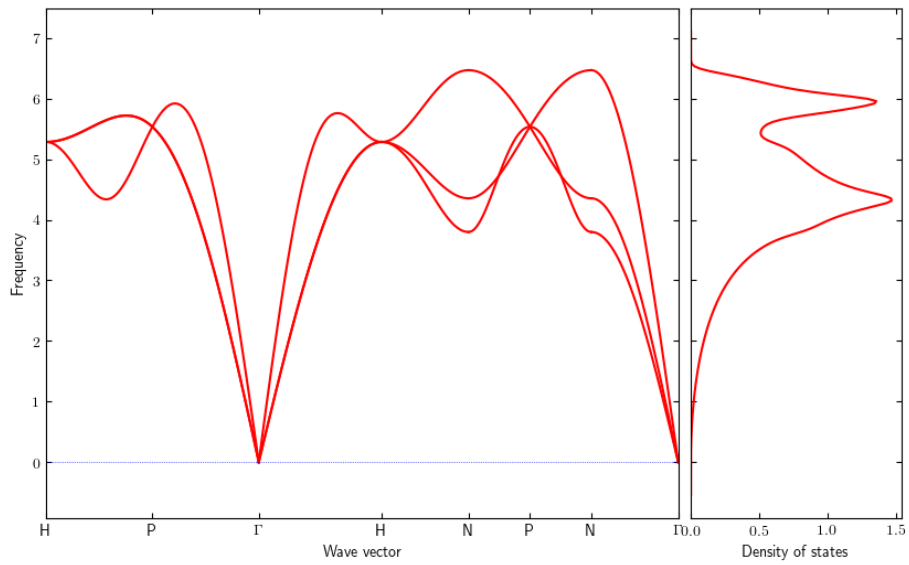

Figure 4.20.: Phononic DOS and bandstructure for a W cell.

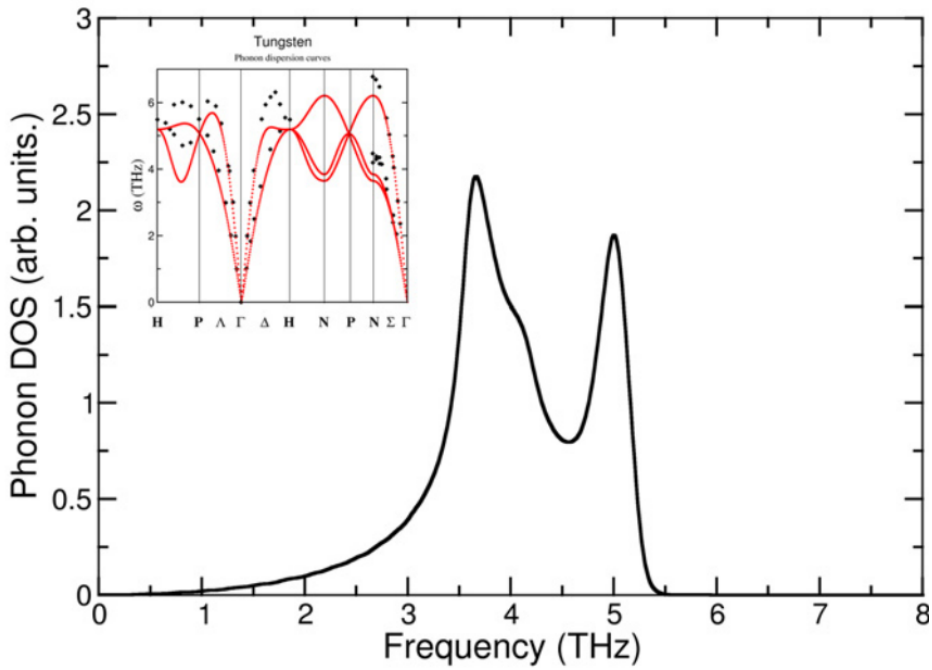

Figure 4.21.: The calculated phonon DOS for W by [70], with an inset showing the band structure as well as - dotted - experimental results from inelastic neutron scattering experiments [71].

4.3.2. Tracer Jump Frequency

To determine the transition state the CINEB method as explained in Chapter 3 was used. The minimum energy path (MEP) is shown in Fig. 4.23. The

$\mathbf{\Delta H_f}$ / eV	$\mathbf{\Delta S_f^{vib}}$ / k_B	**Reference**
3.26	2.57	this work
3.6	3.2	[72]
3.67 ± 0.2	2.3	[73]
$3.14 - 3.42$	6.5	[74]

Table 4.4.: Vacancy formation parameters of W in this thesis compared to experiments.

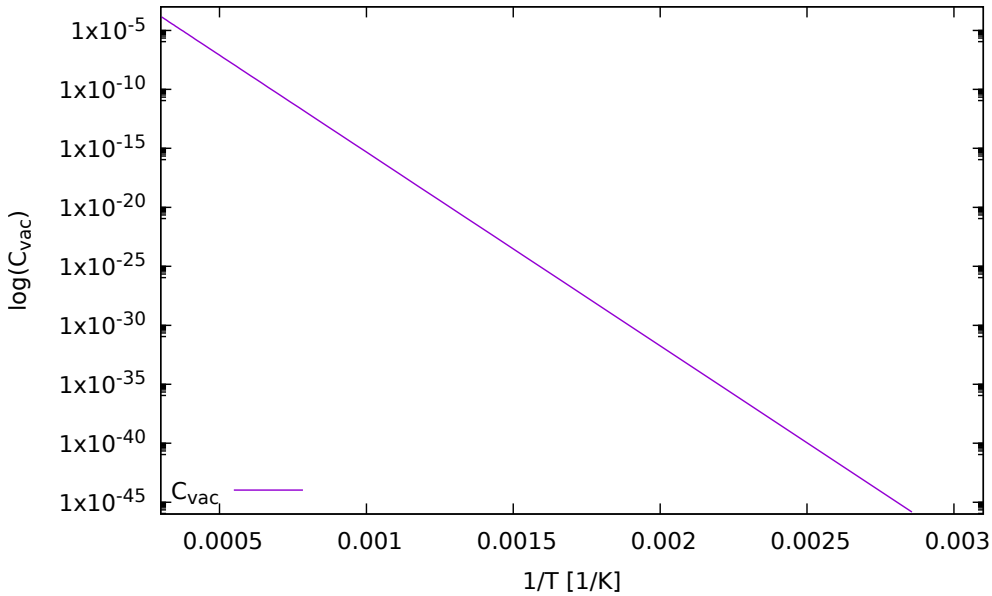

Figure 4.22.: Equilibrium vacancy concentration as a function of (inverse) temperature.

height of the barrier $\Delta H_m = 1.798\,\text{eV}$ agrees very well with literature values, that range from 1.78 eV to 1.82 eV, as shown in Tab. 4.5. On the saddle point the transition state is found. Due to its unstable nature, it is characterized by one imaginary mode in the phononic spectrum as can be seen in Fig. 4.24, where imaginary frequencies are indicated by negative frequencies. This mode corresponds to the vibration in the direction of the MEP. The degrees of freedom perpendicular to this yield the peak at about 7 THz, since the moving atom is unusually close to other atoms - which leads to fast oscillations. Using the phonons obtained by these calculations and evaluating Eqs. 2.31 and 2.32, the tracer jump frequency, $w_0 = 12.84 \times \exp\left(-\frac{1.79}{k_B T}\right)$THz is obtained.

4.3.3. Result

The results are summarized in Tab. 4.5 along various experimental and other computational results. Using Eq. 2.33 this yields the self-diffusion coefficient of tungsten. In Fig. 4.25 the self diffusion coefficient is depicted as a $(log, \frac{1}{T})$

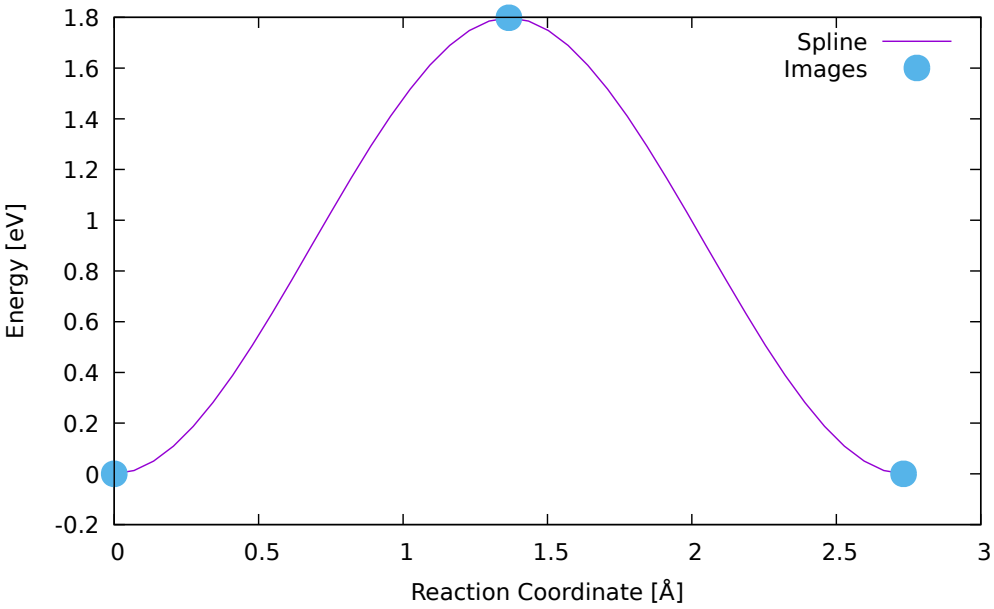

Figure 4.23.: The minimum energy path of the jump process w_0, as shown in Fig. 2.6. The height of the barrier is $\Delta H_m = 1.798\,\mathrm{eV}$.

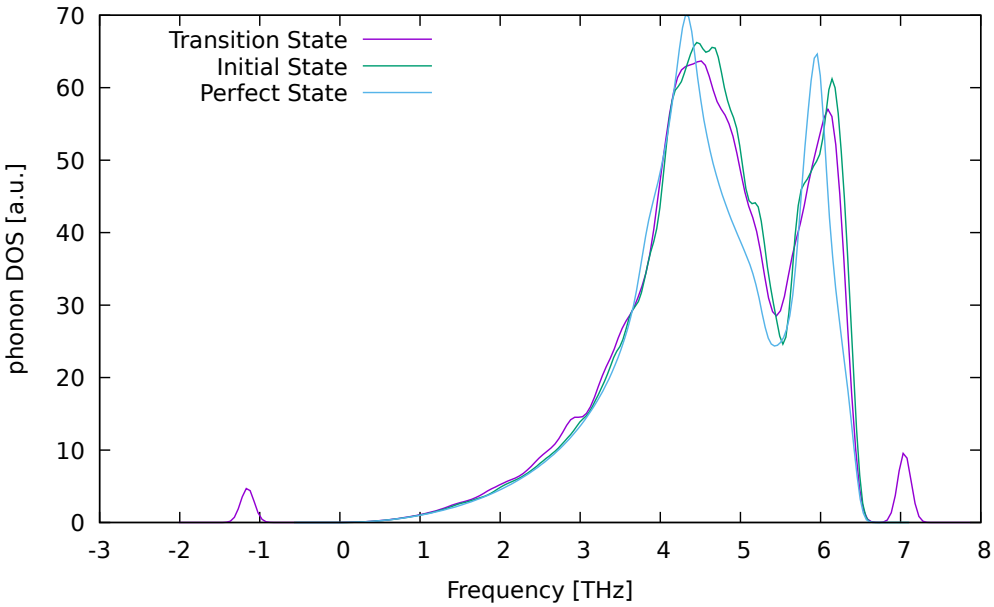

Figure 4.24.: The phonon DOS for the perfect, initial and transition state. The imaginary (here drawn as negative) frequency at $-1.12\,\mathrm{THz}$ identifies the transition state.

diagram together with experimental results from [75]. When comparing the data one needs to consider the caveats mentioned earlier and, even more, the fact that as a transport process, diffusion is highly correlated with the crystal quality, i.e. the more ideal the structure, the better the diffusion, thus explaining the deviations from experiment.

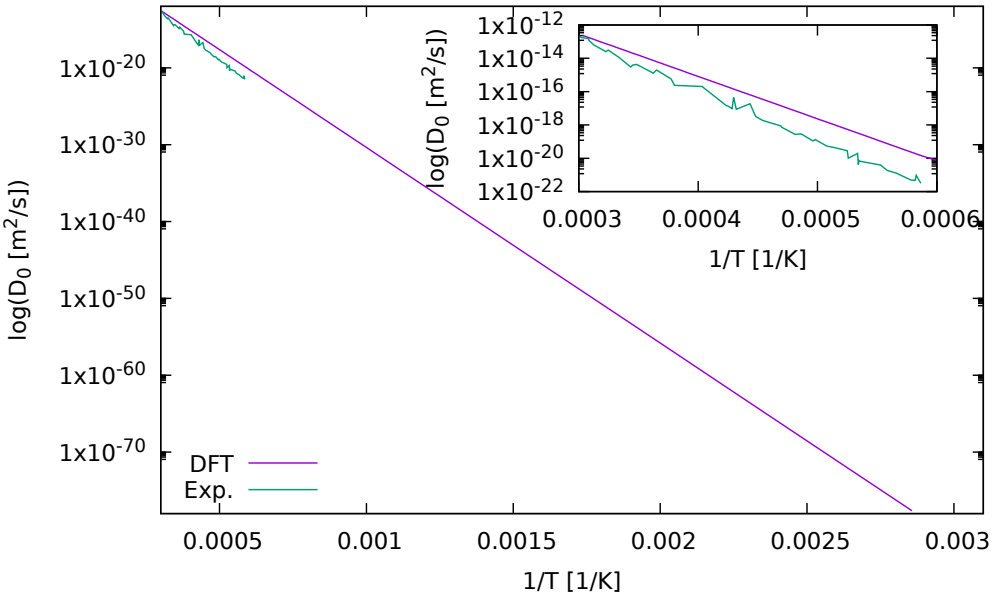

Figure 4.25.: Self-diffusion coefficient of tungsten. The inset shows comparison with experimentally observed values [75].

ΔH_f / eV	ΔS_f / k_B	ΔH_m / eV	D_0 / m/s^2	Q / eV	Ref.
3.26	2.57	1.798	1.23×10^{-5}	5.06	this
3.9 ± 0.2	3	1.8 ± 0.1	-	5.7 ± 0.3	[76]
3.6	3.2	-	-	-	[72]
$3.44 - 3.76$	-	$1.69 - 1.82$	-	$5.26 - 5.48$	[77]
-	2	-	-	-	[78]
3.67 ± 0.2	2.3	1.78 ± 0.1	-	5.45 ± 0.3	[73]
3.6 ± 0.2	3	1.8 ± 0.1	4.6×10^{-3}	5.4 ± 0.3	[75]

Table 4.5.: Quantities necessary for the calculation of the tungsten self-diffusion coefficient in comparison with various computational and experimental results.

4.4. Diffusion of Titanium in Tungsten

To extend the results obtained in the previous section to the diffusion of an impurity Ti atom the frequencies w_2, w_3 and w_4 (which is the reverse process of w_3) need to be obtained. This was again done using the methodology explained in Section 3 and the MEP as well as the phonon spectra can be seen in Figs. 4.26 and 4.27.
The symmetry of the initial and final state for the jump w_2 is expressed in the symmetry of the MEP, as well as the identical phonon spectrum, whereas the asymmetry of w_3 is visible by the lack of symmetry in the MEP and the (albeit slightly) different phononic spectra. Using Eq. 2.34 the diffusion coefficient of Ti impurities in W is obtained and depicted in Fig. 4.28. An approximation of the moved distance can be obtained by inserting these

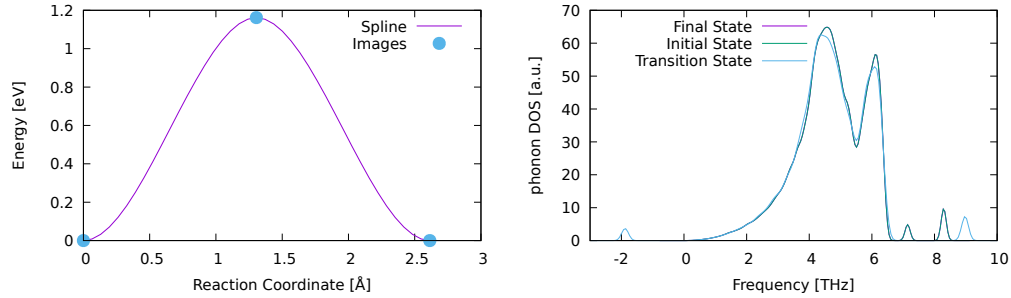

(a) (b)

Figure 4.26.: The MEP and phonon spectra of the states involved in w_2. Clearly visible is the high symmetry in Fig. 4.26a and the identical phononic spectra of the initial and final state in Fig. 4.26b pointing at the symmetric conditions of the jump.

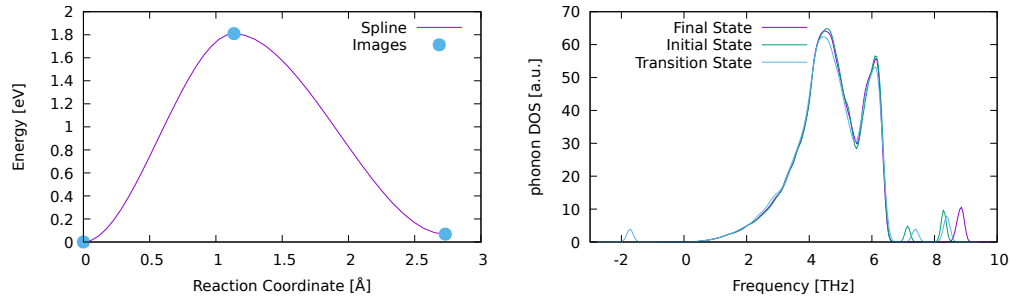

(a) (b)

Figure 4.27.: The MEP and phonon spectra of the states involved in w_3. The asymmetry of the process is reflected in the phononic spectra and the MEP.

results in Eq. 2.23. For the temperature range between 300 K and 700 K for up to an hour, the average distance moved,

$$\sqrt{\langle x^2 \rangle} = \sqrt{2 * D * t},$$

is orders of magnitude below an Ångström, thus we can expect the arrangement of atoms to be as deposited by the sputtering process, i.e. no bulk equilibration can take place in our case. This could be the cause of the intrinsic stresses in the material that are reported in literature [69].

The changes in Ti concentration due to annealing as was shown in e.g. Fig. 4.15, can thus not be the result of bulk diffusion, which means that a significant fraction must be situated in the GB. There, diffusion coefficients are typically $6 - 9$ orders of magnitude higher than in bulk [79–81]. This has numerous reasons, most noteworthy are the drastically increased defect density and a decrease in the activation energies, which can be enhanced even more by external factors, such as electric fields or mechanical stress [82]. Unfortunately no method of calculating grain boundary diffusion coefficients

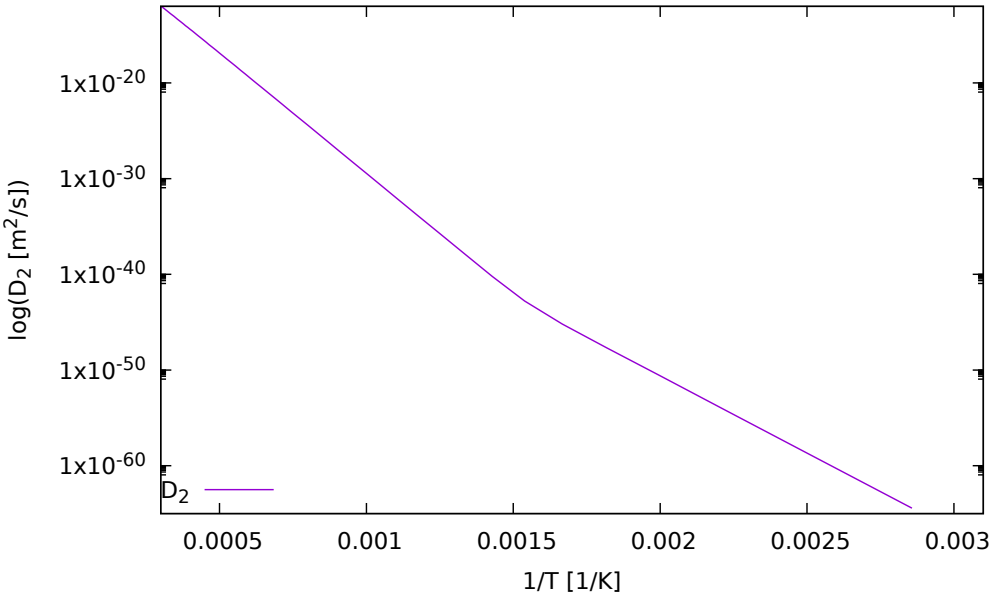

Figure 4.28.: The diffusion coefficient of dilute Ti in W as a function of (inverse) temperature.

using ab initio methods which is practical in terms of either accuracy or computational time is known to the author and is thus postponed for future work.

5. Conclusion and Outlook

The heat of formation of 16 structures containing various amounts of titanium (Ti) in tungsten (W) structures, organized in bulk, grain boundary (GB) and special quasirandom structures (SQS), was calculated and discussed. We found a linear increase of the energy per atom, as well as the heat of formation with increasing Ti content, stemming from an increase in interaction energy. Furthermore all heats of formation were positive, thus pointing towards meta- or unstable structures. From the SQS it was deduced that Ti-W behaves non-Vegard up to about 30 at% Ti.

The densities of states (DOS) of 16 structures were examined using density functional theory (DFT) as implemented in the Vienna ab-initio Simulation Package (VASP) and compared to twelve samples of Ti-W, differing in annealing time and Ti concentration, that have been analyzed using X-ray photoelectron spectroscopy (XPS) and hard X-ray photoelectron spectroscopy (HAXPES) experiments. It was shown that although the cross-section of titanium is very low, the impact of the Ti atoms on the tungsten DOS is noticeable in experiment and simulation alike, however direct identification of GB or bulk specific electronic characteristics is so far impossible. In agreement with the simulations the experimental results show a decrease of the DOS near the Fermi edge with increasing Ti concentration, which can possibly be attributed to an increase of interaction energy. The direct identification of the location of Ti atoms in tungsten has proven to be impossible, mainly due to the aforementioned low intensity of the Ti signal.

Furthermore the impurity diffusion coefficient of Ti in W was determined using first principle methods. Using VASP and phonopy the vibrational properties of tungsten and Ti-doped tungsten was determined. Due to the good agreement of the W self-diffusion coefficient to literature it can be assumed that the match of the impurity diffusion coefficient is reasonable as well. As diffusivity of Ti in bulk W at the temperatures of interest ($T < 670\,\mathrm{K}$) is negligible, it can be deducted that no significant diffusion in the bulk takes place.

However, it was experimentally shown that annealing clearly impacts the DOS of the surface (about 5 nm, XPS) and bulk (about 50 nm, HAXPES) - thus a structural change had to have taken place. Combined with the results from the SQS simulations, the data suggests a significant increase of Ti in the

surface layers and, albeit less pronounced, the near-surface bulk, as annealing time increases. One possible explanation would be a not equilibrated and thus greatly increased vacancy concentration. However the effect alone would have to be very large to increase the diffusion coefficient enough to account for the changes observed in experiment. Another possible explanation would be grain boundary diffusion, something that is also conjectured in literature [69], which in itself is already faster than bulk diffusion. This effect could be furthered even more by the reported residual stresses [83]. Following this hypothesis and combining it with what was reported in literature we can conclude that a significant amount of Ti is located in the grain boundaries.

The core level spectra which were also obtained during the XPS and HAXPES measurements can not be calculated with standard VASP methods. Other DFT codes, such as Wien2k, do have this possibility and should be used to gain a better understanding of the experimental data. Furthermore, given proper analysis by an expert, the XPS and HAXPES data can quantify relative concentrations, which should shed more light on the actual amount of Ti that diffused to the surface.

Future computational work should address diffusion in grain boundaries and develop a methodology to investigate these phenomena as well. Since Ti in diffusion barriers is usually found in higher concentrations as considered for the diffusivity analysis, calculations of the jump frequencies in more environments should likewise be done.

To verify results, experimental measurements using, e.g. the positron annihilation method [84–86], to explore the possibility of a drastically increased vacancy concentration due to the deposition should be carried out. Further XPS analysis, possibly with in-situ annealing, should be performed to better understand the dynamics of the Ti enrichment on the surface. Resonant XPS measurements could theoretically enable differentiation of the GB and bulk Ti-specific features identified in this thesis. Finally atom probe tomography could be able to determine the concentration of Ti within the sample and explore possible phase formation of the constituents.

Appendix

Appendix A.

CL Spectra of the Samples

A.1. XPS Spectra

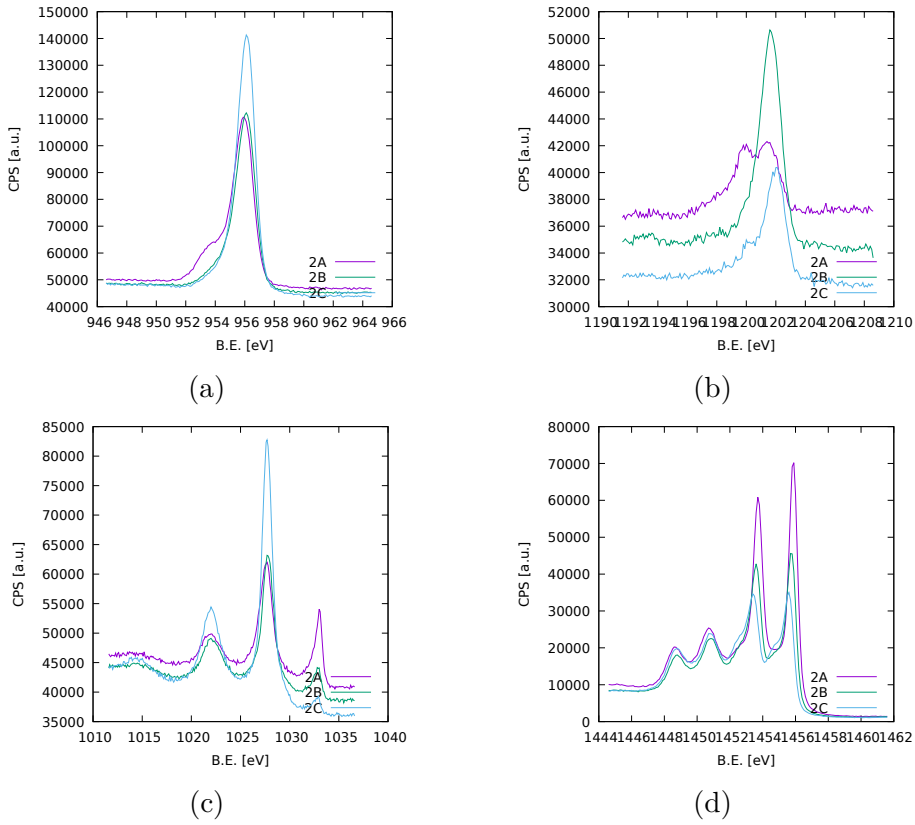

Figure A.1.: XPS CL spectra comparing different anneals of sample 2. Fig. A.1a: $O - 1s$, Fig. A.1b: $C - 1s$, Fig. A.1c: $Ti - 2p$, Fig. A.1d: $W - 4f$.

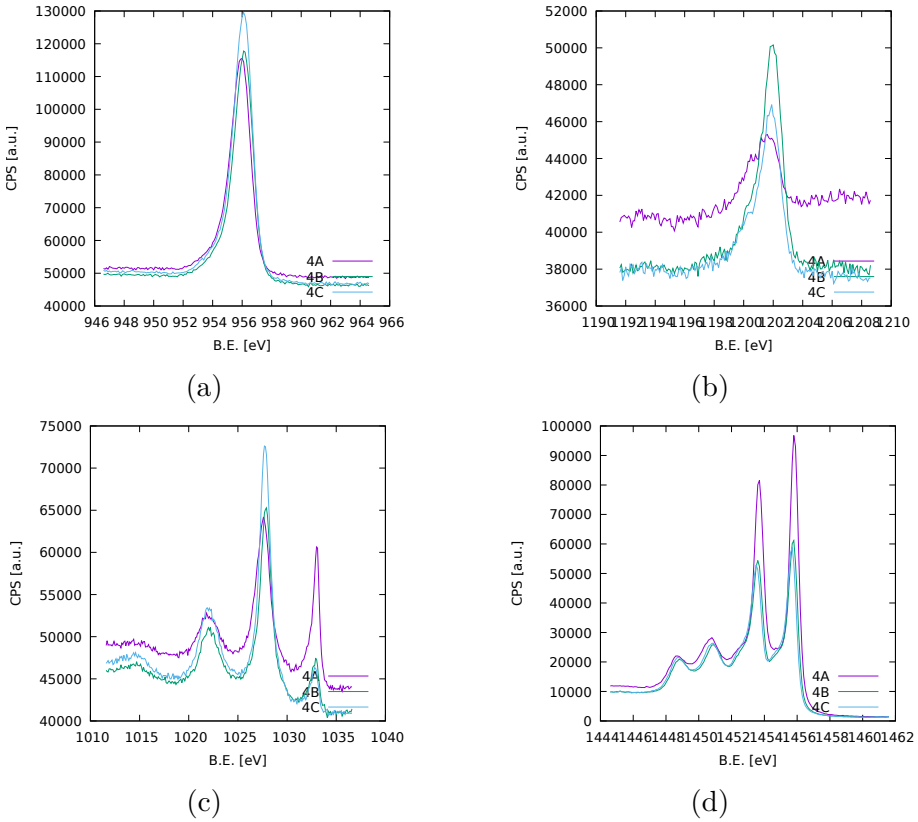

Figure A.2.: XPS CL spectra comparing different anneals of sample 4. Fig. A.2a: $O-1s$, Fig. A.2b: $C-1s$, Fig. A.2c: $Ti-2p$, Fig. A.2d: $W-4f$.

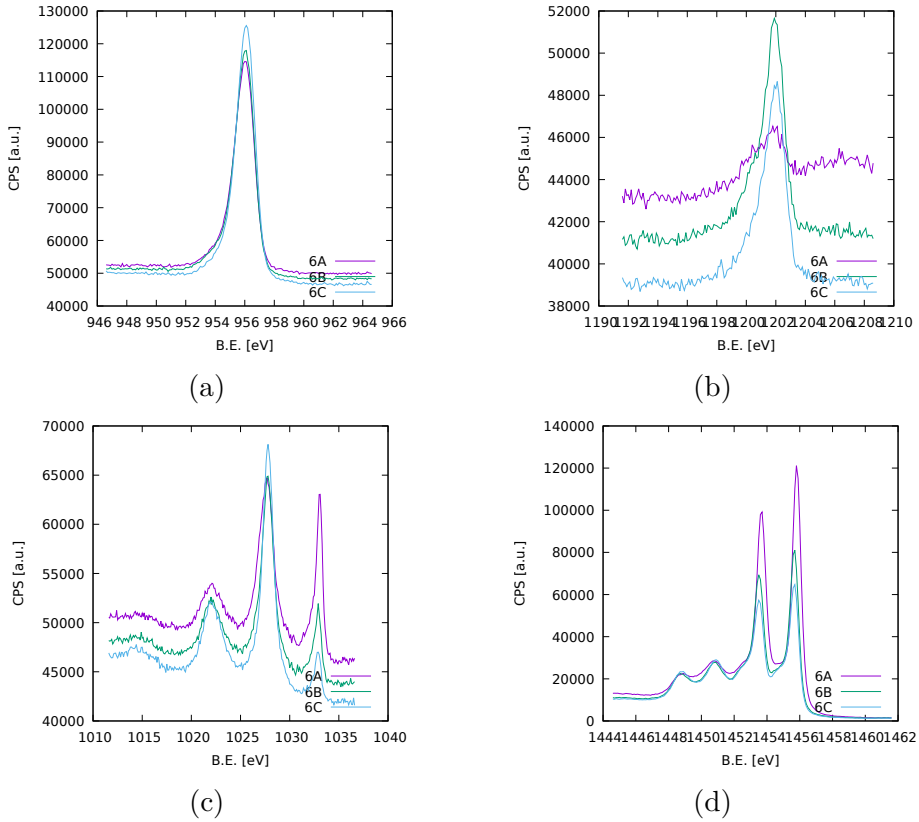

Figure A.3.: XPS CL spectra comparing different anneals of sample 6. Fig. A.3a: $O-1s$, Fig. A.3b: $C-1s$, Fig. A.3c: $Ti-2p$, Fig. A.3d: $W-4f$.

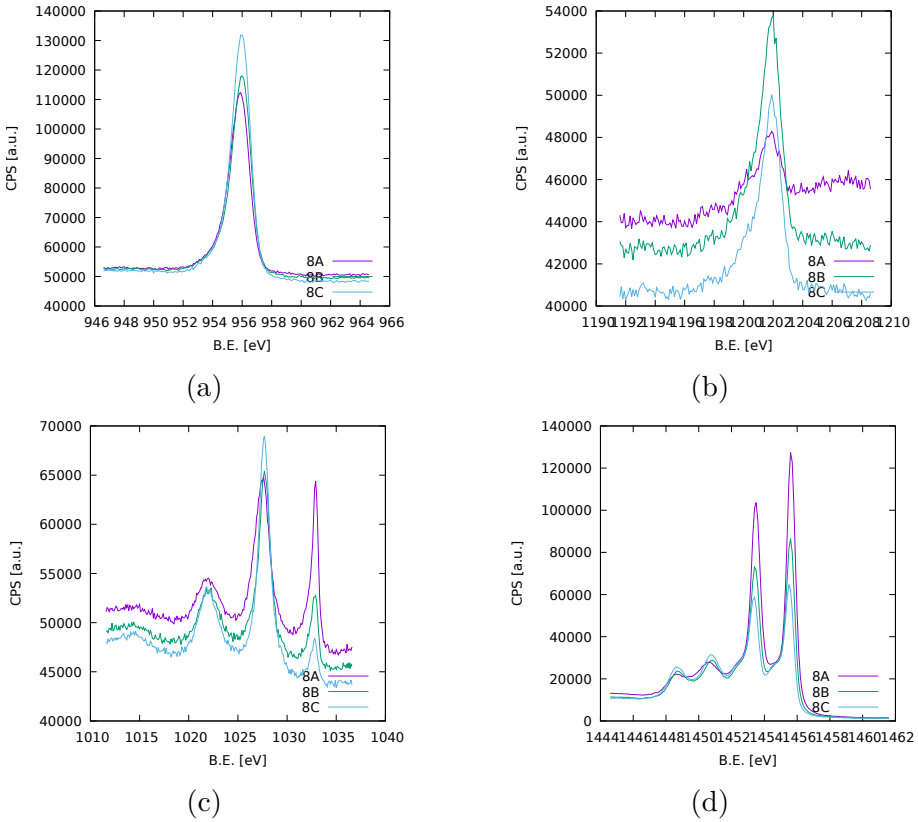

Figure A.4.: XPS CL spectra comparing different anneals of sample 8. Fig. A.4a: $O-1s$, Fig. A.4b: $C-1s$, Fig. A.4c: $Ti-2p$, Fig. A.4d: $W-4f$.

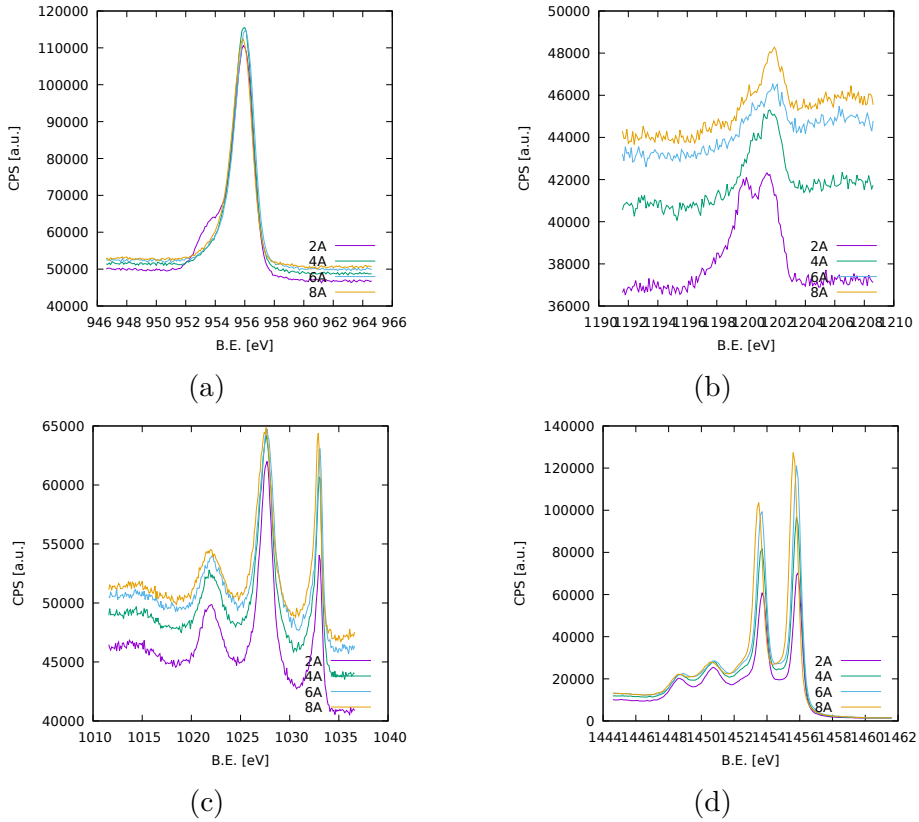

Figure A.5.: XPS CL spectra comparing different concentrations of as deposited samples. Fig. A.5a: $O-1s$, Fig. A.5b: $C-1s$, Fig. A.5c: $Ti-2p$, Fig. A.5d: $W-4f$.

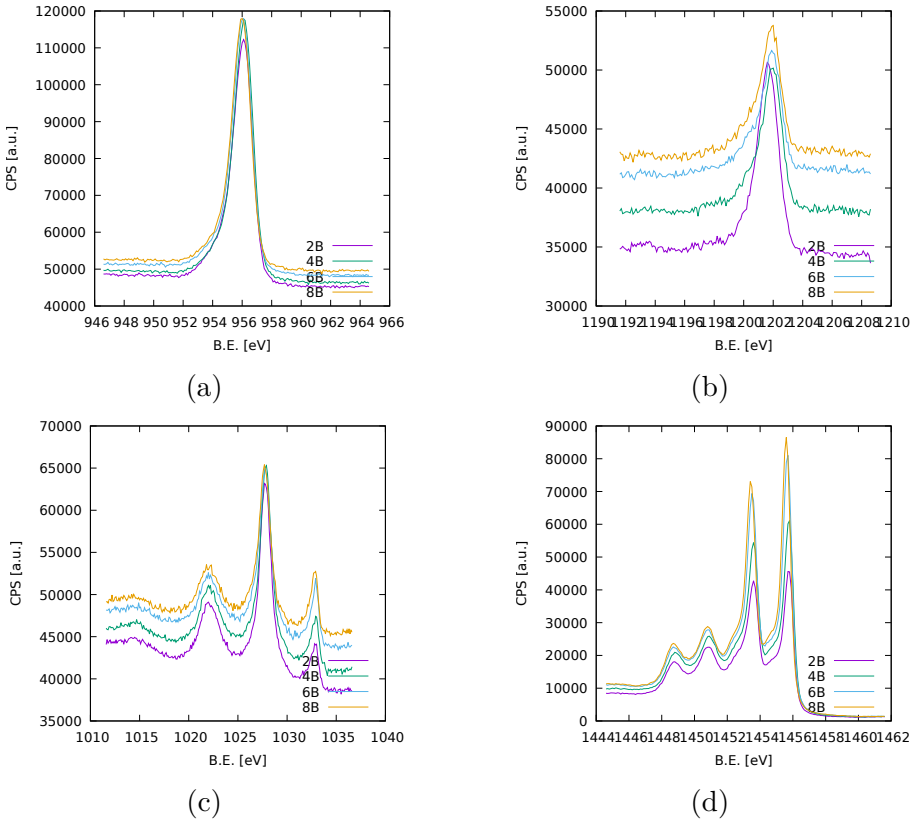

Figure A.6.: XPS CL spectra comparing different concentrations of briefly annealed samples. Fig. A.6a: $O-1s$, Fig. A.6b: $C-1s$, Fig. A.6c: $Ti-2p$, Fig. A.6d: $W-4f$.

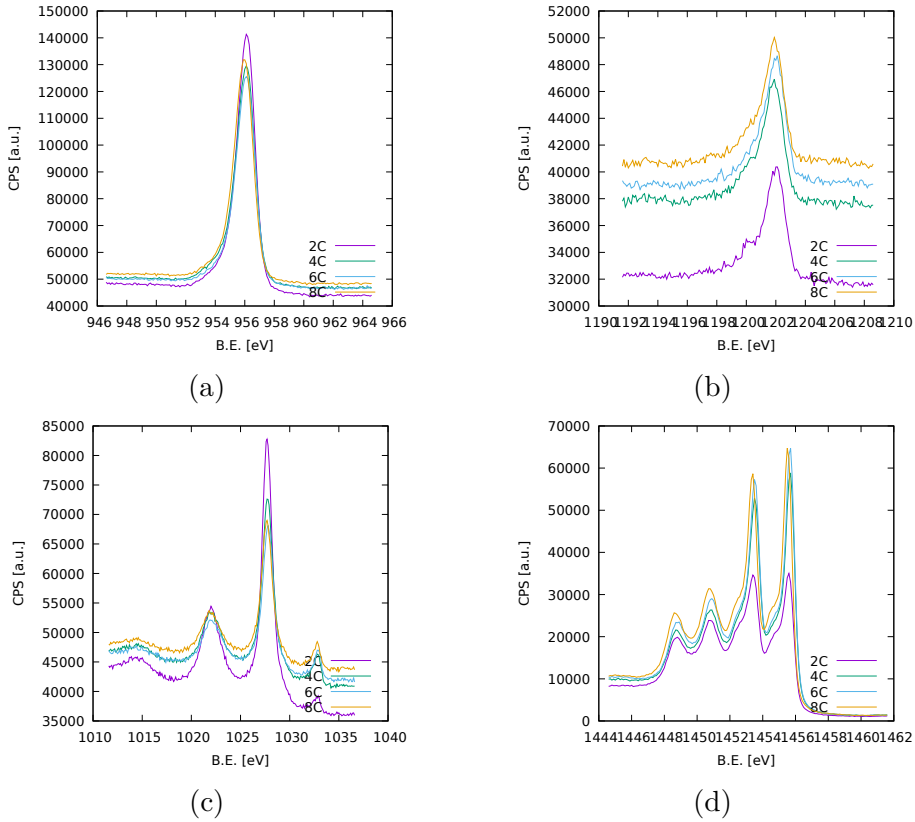

Figure A.7.: XPS CL spectra comparing different concentrations of long-term annealed samples. Fig. A.7a: $O-1s$, Fig. A.7b: $C-1s$, Fig. A.7c: $Ti-2p$, Fig. A.7d: $W-4f$.

A.2. HAXPES Spectra

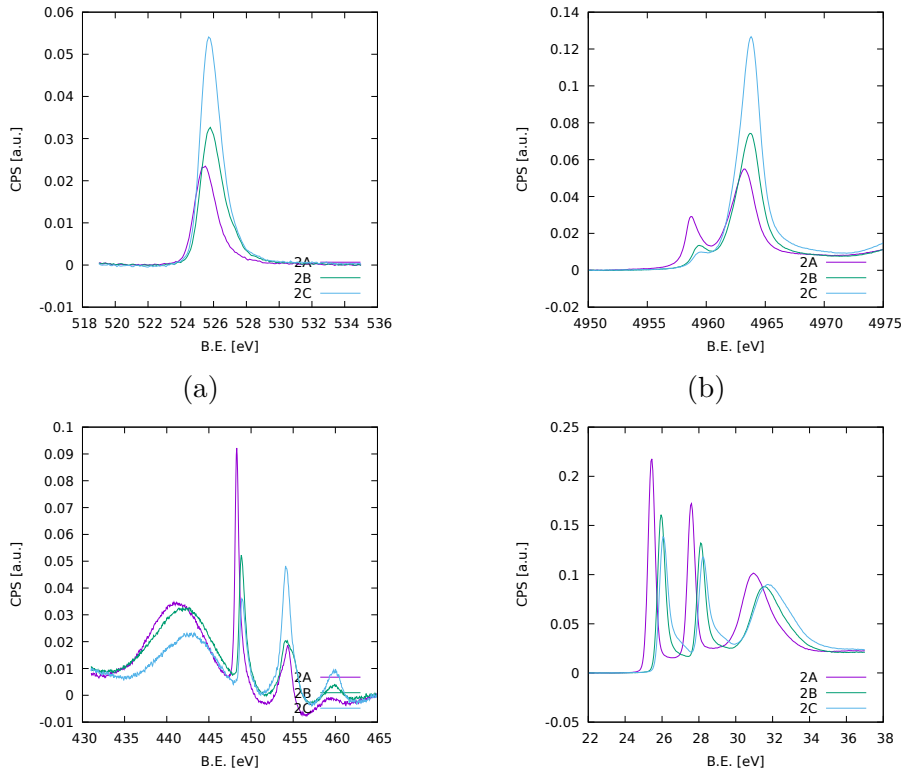

(a) (b) (c) (d)

Figure A.8.: HAXPES CL spectra comparing different anneals of sample 2. Fig. A.8a: $O-1s$, Fig. A.8b: $Ti-1s$, Fig. A.8c: $Ti-2p$, Fig. A.8d: $W-4f$.

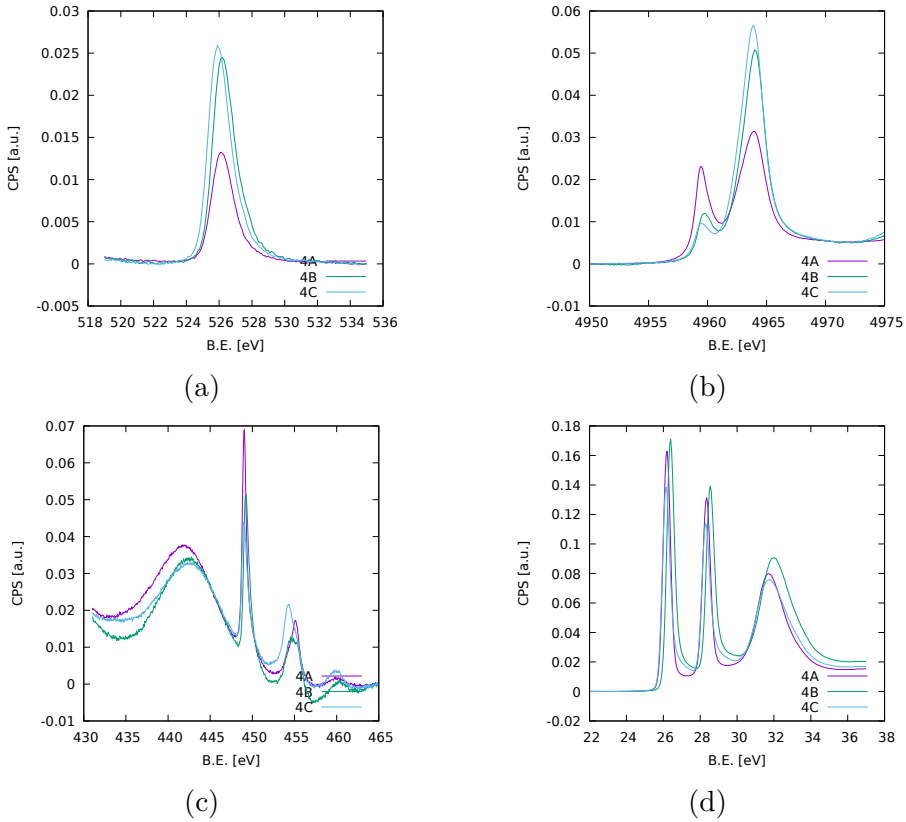

Figure A.9.: HAXPES CL spectra comparing different anneals of sample 4. Fig. A.9a: $O-1s$, Fig. A.9b: $Ti-1s$, Fig. A.9c: $Ti-2p$, Fig. A.9d: $W-4f$.

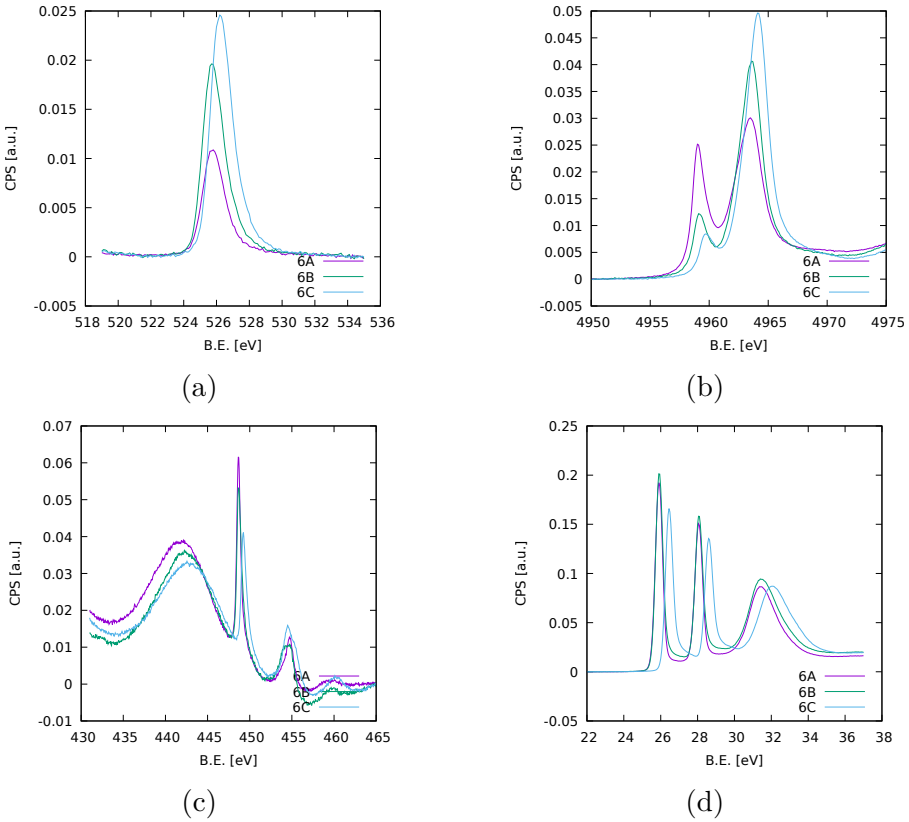

Figure A.10.: HAXPES CL spectra comparing different anneals of sample 6. Fig. A.10a: $O-1s$, Fig. A.10b: $Ti-1s$, Fig. A.10c: $Ti-2p$, Fig. A.10d: $W-4f$.

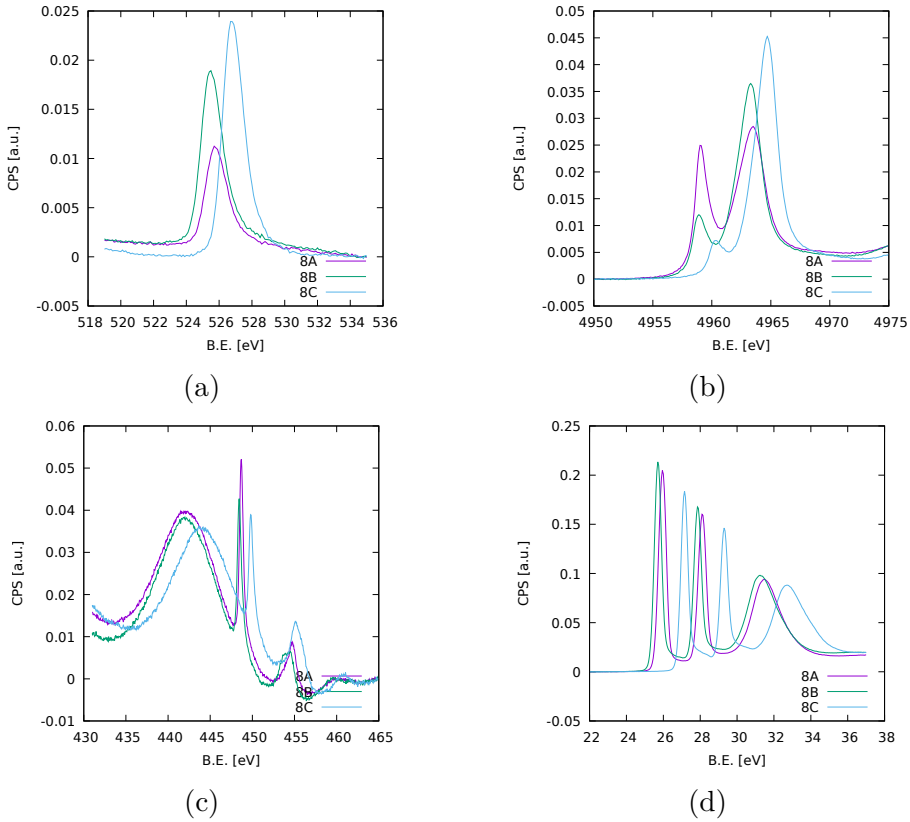

Figure A.11.: HAXPES CL spectra comparing different anneals of sample 8. Fig. A.11a: $O-1s$, Fig. A.11b: $Ti-1s$, Fig. A.11c: $Ti-2p$, Fig. A.11d: $W-4f$.

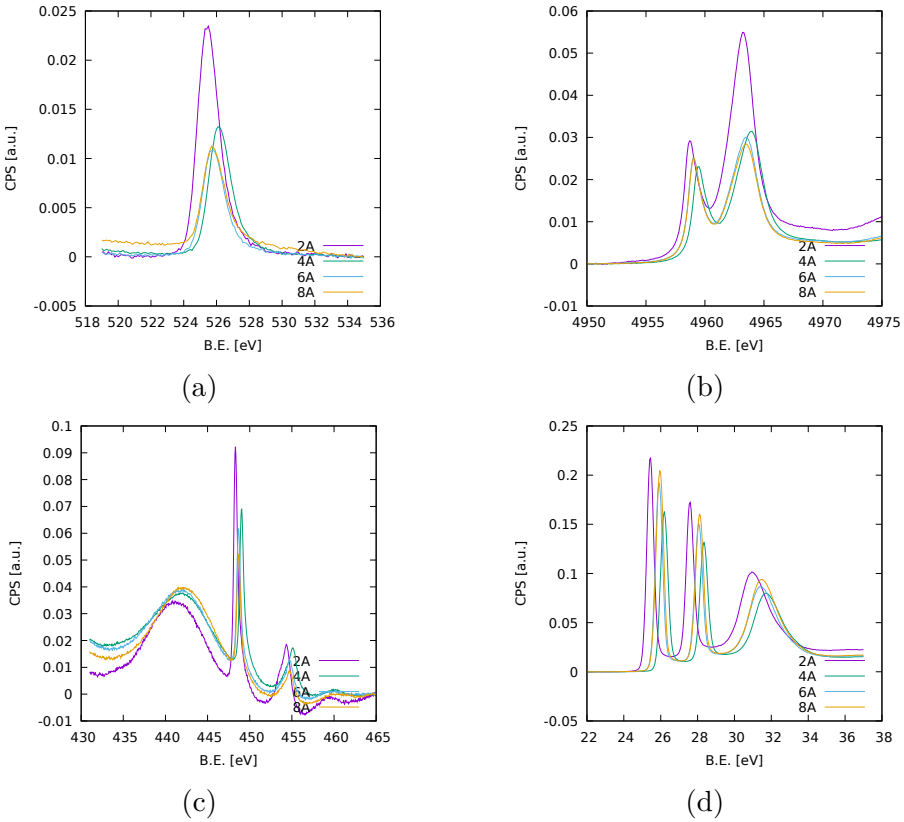

Figure A.12.: HAXPES CL spectra comparing different concentrations of as deposited samples. Fig. A.12a: $O-1s$, Fig. A.12b: $Ti-1s$, Fig. A.12c: $Ti-2p$, Fig. A.12d: $W-4f$.

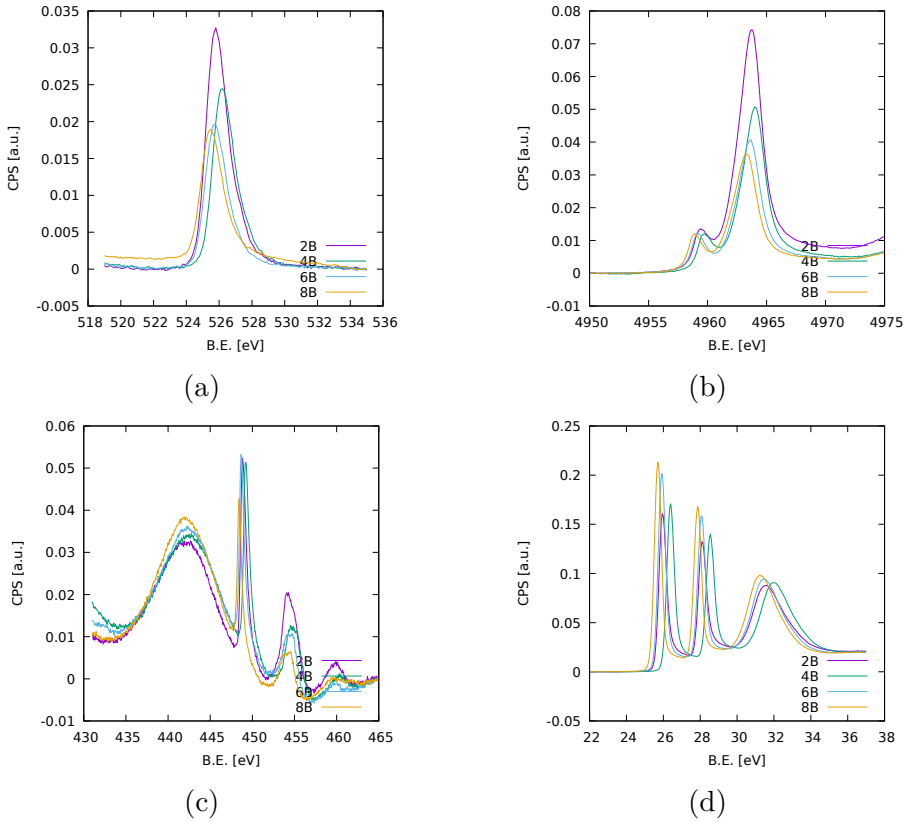

Figure A.13.: HAXPES CL spectra comparing different concentrations of briefly annealed samples. Fig. A.13a: $O - 1s$, Fig. A.13b: $Ti - 1s$, Fig. A.13c: $Ti - 2p$, Fig. A.13d: $W - 4f$.

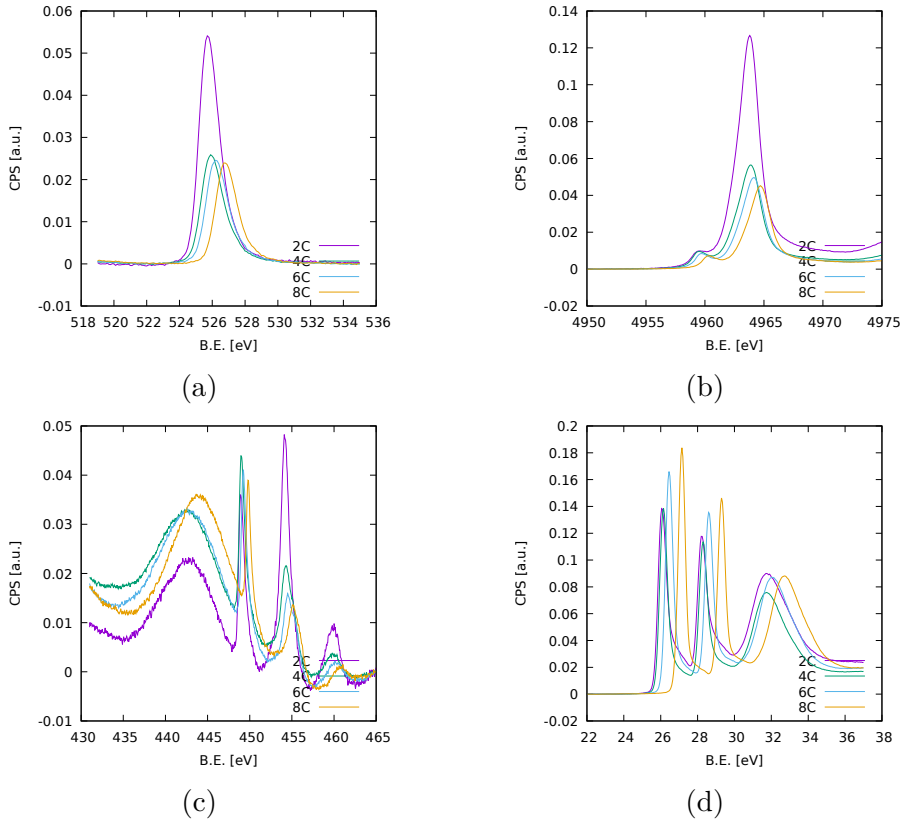

Figure A.14.: HAXPES CL spectra comparing different concentrations of long-term annealed samples. Fig. A.14a: $O-1s$, Fig. A.14b: $Ti-1s$, Fig. A.14c: $Ti-2p$, Fig. A.14d: $W-4f$.

Appendix B.

All Densities of State

B.1. Bulk Structures

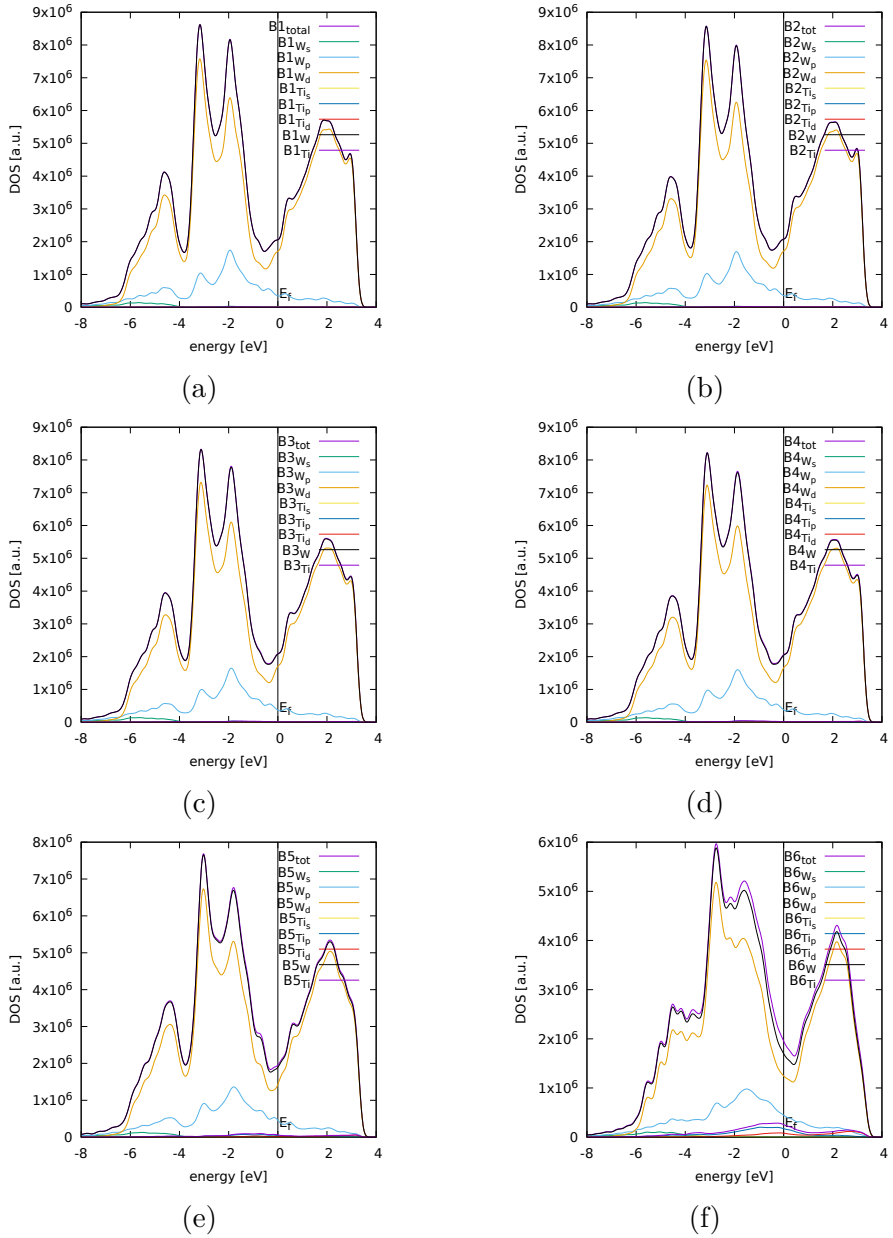

Figure B.1.: The decomposed DOSes of all bulk structures considered. B1: Fig. B.1a; B2: Fig. B.1b; B3: Fig. B.1c; B4: Fig. B.1d; B5: Fig. B.1e; B6: Fig. B.1f.

B.2. Grain Boundary Structures

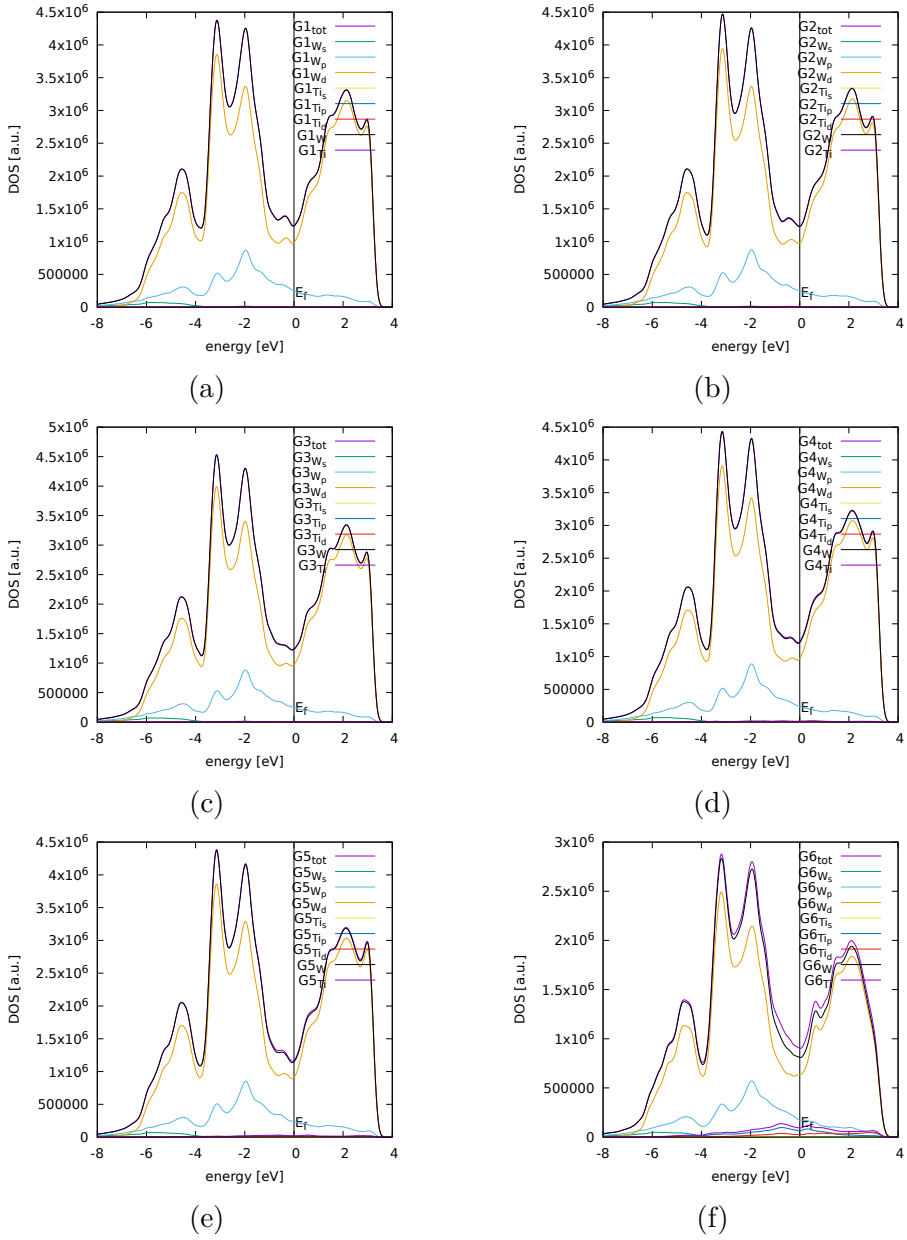

Figure B.2.: The decomposed DOSes of all GB structures considered. G1: Fig. B.2a; G2: Fig. B.2b; G3: Fig. B.2c; G4: Fig. B.2d; G5: Fig. B.2e; G6: Fig. B.2f.

Bibliography

[1] W. Robl, M. Melzl, B. Weidgans, R. Hofmann, and M. Stecher. "Last Metal Copper Metallization for Power Devices". In: *IEEE Transactions on Semiconductor Manufacturing* 21.3 (2008), pp. 358–362. ISSN: 0894-6507.

[2] Andrei A. Istratov and Eicke R. Weber. "Physics of Copper in Silicon". In: *Journal of The Electrochemical Society* 149.1 (2002), G21. ISSN: 8756-663X.

[3] S. P. Murarka. "Diffusion Barriers in Semiconductor Devices/Circuits". In: *Diffusion processes in advanced technological materials*. Ed. by Devendra Gupta. Norwich, NY and Heidelberg: William Andrew and Springer, 2005, pp. 239–281. ISBN: 9780815515012.

[4] Vance Hoffman. "Tungsten Titanium Diffusion Barrier Metallization". In: *Solid State Technology* 26.6 (1983), pp. 119–126.

[5] G. Neumann and C. Tuijn. *Self-diffusion and impurity diffusion in pure metals: Handbook of experimental data*. Pergamon materials series. Amsterdam and London: Elsevier, 2009. ISBN: 1856175111.

[6] G. Kresse and J. Hafner. "Ab initio molecular dynamics for liquid metals". In: *Physical Review B* 47.1 (1993), p. 558.

[7] G. Kresse and J. Hafner. "Ab initio molecular-dynamics simulation of the liquid-metal–amorphous-semiconductor transition in germanium". In: *Physical Review B* 49.20 (1994), p. 14251.

[8] G. Kresse and J. Furthmüller. "Efficient iterative schemes for ab initio total-energy calculations using a plane-wave basis set". In: *Physical Review B* 54.16 (1996), p. 11169.

[9] G. Kresse and D. Joubert. "From ultrasoft pseudopotentials to the projector augmented-wave method". In: *Physical Review B* 59.3 (1999), p. 1758.

[10] Daniel Scheiber, Reinhard Pippan, Peter Puschnig, and Lorenz Romaner. "Ab initio calculations of grain boundaries in bcc metals". In: *Modelling and Simulation in Materials Science and Engineering* 24.3 (2016), p. 035013. ISSN: 0965-0393.

[11] D. Scheiber, R. Pippan, P. Puschnig, and L. Romaner. "Ab initio search for cohesion-enhancing impurity elements at grain boundaries in molybdenum and tungsten". In: *Modelling and Simulation in Materials Science and Engineering* 24.8 (2016), p. 085009. ISSN: 0965-0393.

[12] D. W. Oxtoby, H. P. Gillis, and A. Campion. *Principles of Modern Chemistry*. Cengage Learning, 2011. ISBN: 9780840049315.

[13] Nils Sandberg, Blanka Magyari-Köpe, and Thomas R. Mattsson. "Self-diffusion rates in Al from combined first-principles and model-potential calculations". In: *Physical review letters* 89.6 (2002), p. 065901. ISSN: 0031-9007.

[14] George H. Vineyard. "Frequency factors and isotope effects in solid state rate processes". In: *Journal of Physics and Chemistry of Solids* 3.1-2 (1957), pp. 121–127. ISSN: 00223697.

[15] Manjeera Mantina. "A first-principles methodology for diffusion coefficients in metals and dilute alloys". PhD thesis. Pennsylvania State University, 2008.

[16] M. Mantina, Y. Wang, R. Arroyave, L. Q. Chen, Z. K. Liu, and C. Wolverton. "First-principles calculation of self-diffusion coefficients". In: *Physical review letters* 100.21 (2008), p. 215901. ISSN: 0031-9007.

[17] M. Mantina, S. L. Shang, Y. Wang, L. Q. Chen, and Z. K. Liu. "3d transition metal impurities in aluminum: A first-principles study". In: *Physical Review B* 80.18 (2009), p. 207.

[18] A. D. Leclaire and A. B. Lidiard. "LIII. Correlation effects in diffusion in crystals". In: *Philosophical Magazine* 1.6 (1956), pp. 518–527. ISSN: 0031-8086.

[19] Peter Mohn and Silke Bühler-Paschen. *Festkörperphysik II*. 2014.

[20] M. Born and R. Oppenheimer. "Zur Quantentheorie der Molekeln". In: *Annalen der Physik* 389.20 (1927), pp. 457–484. ISSN: 00033804.

[21] D. R. Hartree. "The Wave Mechanics of an Atom with a Non-Coulomb Central Field. Part II. Some Results and Discussion". In: *Mathematical Proceedings of the Cambridge Philosophical Society* 24.01 (1928), p. 111. ISSN: 0305-0041.

[22] W. Pauli. "Über den Zusammenhang des Abschlusses der Elektronengruppen im Atom mit der Komplexstruktur der Spektren". In: *Zeitschrift für Physik* 31.1 (1925), pp. 765–783. ISSN: 0044-3328.

[23] V. Fock. "Näherungsmethode zur Lösung des quantenmechanischen Mehrkörperproblems". In: *Zeitschrift für Physik* 61.1-2 (1930), pp. 126–148. ISSN: 0044-3328.

[24] J. C. Slater. "The Theory of Complex Spectra". In: *Physical Review* 34.10 (1929), pp. 1293–1322. ISSN: 0031-899X.

[25] P. Hohenberg and W. Kohn. "Inhomogeneous Electron Gas". In: *Physical Review* 136.3B (1964), B864–B871. ISSN: 0031-899X.

[26] Walter Ritz. "Über eine neue Methode zur Lösung gewisser Variationsprobleme der mathematischen Physik". In: *Journal für die reine und angewandte Mathematik (Crelle's Journal)* 1909.135 (1909), pp. 1–61. ISSN: 0075-4102.

[27] W. Kohn and L. J. Sham. "Self-Consistent Equations Including Exchange and Correlation Effects". In: *Physical Review* 140.4A (1965), A1133–A1138. ISSN: 0031-899X.

[28] David S. Sholl and Janice A. Steckel. *Density Functional Theory*. Hoboken, NJ, USA: John Wiley & Sons, Inc, 2009. ISBN: 9780470447710.

[29] John P. Perdew. "Jacob's ladder of density functional approximations for the exchange-correlation energy". In: *AIP Conference Proceedings*. AIP, June 2000, pp. 1–20.

[30] Kieron Burke, John P. Perdew, and Yue Wang. "Derivation of a Generalized Gradient Approximation: The PW91 Density Functional". In: *Electronic Density Functional Theory*. Ed. by John F. Dobson, Giovanni Vignale, and Mukunda P. Das. Boston, MA and s.l.: Springer US, 1998, pp. 81–111. ISBN: 978-1-4899-0318-1.

[31] John P. Perdew, Kieron Burke, and Matthias Ernzerhof. "Generalized Gradient Approximation Made Simple". In: *Physical Review Letters* 77.18 (1996), p. 3865.

[32] Jianmin Tao, John P. Perdew, Viktor N. Staroverov, and Gustavo E. Scuseria. "Climbing the density functional ladder: nonempirical meta-generalized gradient approximation designed for molecules and solids". In: *Physical review letters* 91.14 (2003), p. 146401. ISSN: 0031-9007.

[33] A. D. Becke. "Density-functional exchange-energy approximation with correct asymptotic behavior". In: *Physical Review A* 38.6 (1988), pp. 3098–3100. ISSN: 0556-2791.

[34] Chengteh Lee, Weitao Yang, and Robert G. Parr. "Development of the Colle-Salvetti correlation-energy formula into a functional of the electron density". In: *Physical Review B* 37.2 (1988), pp. 785–789.

[35] Charles Kittel. *Introduction to solid state physics*. 8. ed. Hoboken, NJ: Wiley, 2005. ISBN: 9780471680574.

[36] Koichi Momma and Fujio Izumi. "VESTA 3 for three-dimensional visualization of crystal, volumetric and morphology data". In: *Journal of Applied Crystallography* 44.6 (2011), pp. 1272–1276. ISSN: 0021-8898.

[37] S. Ranganathan. "On the geometry of coincidence-site lattices". In: *Acta Crystallographica* 21.2 (1966), pp. 197–199. ISSN: 0365-110X.

[38] Pavel Lejcek. *Grain Boundary Segregation in Metals*. Vol. 136. Springer Series in Materials Science. Berlin, Heidelberg: Springer-Verlag Berlin Heidelberg, 2010. ISBN: 9783642125041.

[39] Alex Zunger, S.-H. Wei, L. G. Ferreira, and James E. Bernard. "Special quasirandom structures". In: *Physical Review Letters* 65.3 (1990), p. 353.

[40] A. van de Walle, M. D. Asta, and G. Ceder. "The Alloy Theoretic Automated Toolkit: A User Guide". In: *Calphad* 26 (2002), pp. 539–553.

[41] A. van de Walle. "Multicomponent multisublattice alloys, nonconfigurational entropy and other additions to the Alloy Theoretic Automated Toolkit". In: *Calphad* 33 (2009), pp. 266–278.

[42] A. Einstein. "Über die von der molekularkinetischen Theorie der Wärme geforderte Bewegung von in ruhenden Flüssigkeiten suspendierten Teilchen". In: *Annalen der Physik* 322.8 (1905), pp. 549–560. ISSN: 00033804.

[43] Wilhelm Jost and Henry Eyring, eds. *Physical chemistry: An advanced treatise*. New York: Acad. Pr, 1970. ISBN: 0122456106.

[44] A. D. Le Claire. "The theory of D0 in the Arrhenius equation for self-diffusion in cubic metals". In: *Acta Metallurgica* 1.4 (1953), pp. 438–447. ISSN: 00016160.

[45] James Stirling and Ian Tweddle. *James Stirling's Methodus differentialis: An annotated translation of Stirling's text*. Sources and studies in the history of mathematics and physical sciences. London: Springer, 2003. ISBN: 1852337230.

[46] N. L. Peterson. "Self-diffusion in pure metals". In: *Journal of Nuclear Materials* 69-70 (1978), pp. 3–37. ISSN: 00223115.

[47] Henry Eyring. "The Activated Complex in Chemical Reactions". In: *The Journal of Chemical Physics* 3.2 (1935), pp. 107–115. ISSN: 0002-7863.

[48] G. Neumann, C. Tuijn, G. de Vries, and H. Bakker. "Diffusion Mechanisms in B.C.C. Metals. Calculation of the Correlation Factor for Mixed Nearest and Next-Nearest Neighbour Vacancy Jumps". In: *physica status solidi (b)* 149.2 (1988), pp. 483–493. ISSN: 03701972.

[49] John R. Manning. "Correlation Factors for Impurity Diffusion. bcc, Diamond, and fcc Structures". In: *Physical Review* 136.6A (1964), A1758–A1766. ISSN: 0031-899X.

[50] D. Briggs. "XPS". In: *Surface analysis of polymers by XPS and static SIMS*. Ed. by David Briggs. Cambridge solid state science series. Cambridge: Cambridge University Press, 1998, pp. 14–46. ISBN: 9780511525261.

[51] P. E. Blöchl. "Projector augmented-wave method". In: *Physical Review B* 50.24 (1994), p. 17953.

[52] M. Methfessel and A. Paxton. "High-precision sampling for Brillouin-zone integration in metals". In: *Physical Review B* 40.6 (1989), p. 3616.

[53] Adam J Jackson, Alex M Ganose, Anna Regoutz, Russell G. Egdell, and David O Scanlon. "Galore: Broadening and weighting for simulation of photoelectron spectroscopy". In: *Journal of Open Source Software* 3.26 (2018), p. 773.

[54] Atsushi Togo and Isao Tanaka. "First principles phonon calculations in materials science". In: *Scripta Materialia* 108 (2015), pp. 1–5. ISSN: 13596462.

[55] Graeme Henkelman and Hannes Jónsson. "Improved tangent estimate in the nudged elastic band method for finding minimum energy paths and saddle points". In: *The Journal of Chemical Physics* 113.22 (2000), pp. 9978–9985. ISSN: 0002-7863.

[56] Graeme Henkelman, Blas P. Uberuaga, and Hannes Jónsson. "A climbing image nudged elastic band method for finding saddle points and minimum energy paths". In: *The Journal of Chemical Physics* 113.22 (2000), pp. 9901–9904. ISSN: 0002-7863.

[57] P. Güttinger. "Das Verhalten von Atomen im magnetischen Drehfeld". In: *Zeitschrift für Physik* 73.3-4 (1932), pp. 169–184. ISSN: 0044-3328.

[58] Francis Birch. "Finite Elastic Strain of Cubic Crystals". In: *Physical Review* 71.11 (1947), pp. 809–824. ISSN: 0031-899X.

[59] Wheeler P. Davey. "Precision Measurements of the Lattice Constants of Twelve Common Metals". In: *Physical Review* 25.6 (1925), pp. 753–761. ISSN: 0031-899X.

[60] B. N. Dutta and B. Dayal. "Lattice Constants and Thermal Expansion of Palladium and Tungsten up to 878 °C by X-Ray Method". In: *physica status solidi (b)* 3.12 (1963), pp. 2253–2259. ISSN: 03701972.

[61] C. T. Chan, David Vanderbilt, and Steven G. Louie. "Application of a general self-consistency scheme in the linear combination of atomic orbitals formalism to the electronic and structural properties of Si and W". In: *Physical Review B* 33.4 (1986), pp. 2455–2464.

[62] Neil W. Ashcroft and N. David Mermin. *Solid state physics*. Repr. South Melbourne: Brooks/Cole Thomson Learning, 2012. ISBN: 97800-30839931.

[63] Lianhua He, Fang Liu, Geoffroy Hautier, Micael J. T. Oliveira, Miguel A. L. Marques, Fernando D. Vila, J. J. Rehr, G.-M. Rignanese, and Aihui Zhou. "Accuracy of generalized gradient approximation functionals for density-functional perturbation theory calculations". In: *Physical Review B* 89.6 (2014), p. 920.

[64] R. M. Wood. "The Lattice Constants of High Purity Alpha Titanium". In: *Proceedings of the Physical Society* 80.3 (1962), p. 783. ISSN: 0370-1328.

[65] L. Vegard. "Die Konstitution der Mischkristalle und die Raumfüllung der Atome". In: *Zeitschrift für Physik* 5.1 (1921), pp. 17–26. ISSN: 0044-3328.

[66] Rodney Boyer, Gerhard Welsch, and E. W. Collings. *Materials properties handbook: Titanium alloys*. 4. printing. Materials Park, Ohio: ASM International, 2007. ISBN: 9780871704818.

[67] Tongjai Chookajorn, Heather A. Murdoch, and Christopher A. Schuh. "Design of Stable Nanocrystalline Alloys". In: *Science* 337.6097 (2012), pp. 951–954. ISSN: 1095-9203.

[68] W. H. McMaster, N. Kerr Del Grande, J. H. Mallett, and J. H. Hubbell. "Compilation of x-ray cross sections UCRL-50174, sections I, II revision 1, III, IV". In: *Atomic Data and Nuclear Data Tables* 8.4-6 (1970), pp. 443–444. ISSN: 0092640X.

[69] Michael Fugger. "Integrity of diffusion barriers in modern high-voltage power semiconductors". PhD thesis. Technische Universität Wien, 2014.

[70] Jean-Paul Crocombette, Paul Notargiacomo, and M-C Marinica. "Effect of the variation of the electronic density of states of zirconium and tungsten on their respective thermal conductivity evolution with temperature". In: *Journal of Physics: Condensed Matter* 27.16 (2015), p. 165501. ISSN: 0953-8984.

[71] A. Larose and B. N. Brockhouse. "Lattice vibrations in tungsten at 22 °C studied by neutron scattering". In: *Canadian Journal of Physics* 54.17 (1976), pp. 1819–1823. ISSN: 0008-4204.

[72] J. Y. Park, H. C. W. Huang, R. W. Siegel, and R. W. Balluffi. "A quantitative study of vacancy defects in quenched tungsten by combined field-ion microscopy and electrical resistometry". In: *Philosophical Magazine A* 48.3 (1983), pp. 397–419. ISSN: 0141-8610.

[73] K-D. Rasch, R. W. Siegel, and H. Schultz. "Quenching and recovery investigations of vacancies in tungsten". In: *Philosophical Magazine A* 41.1 (1980), pp. 91–117. ISSN: 0141-8610.

[74] H. Schultz. "Point defects in body-centered cubic transition metals". In: *Materials Science and Engineering* 3.4 (1968), pp. 189–219. ISSN: 00255416.

[75] J. N. Mundy, S. J. Rothman, N. Q. Lam, H. A. Hoff, and L. J. Nowicki. "Self-diffusion in tungsten". In: *Physical Review B* 18.12 (1978), p. 6566.

[76] K.-D. Rasch, R. W. Siegel, and H. Schultz. "Quenching and recovery experiments on tungsten". In: *Journal of Nuclear Materials* 69-70 (1978), pp. 622–624. ISSN: 00223115.

[77] Alessandra Satta, F. Willaime, and Stefano de Gironcoli. "Vacancy self-diffusion parameters in tungsten: Finite electron-temperature LDA calculations". In: *Physical Review B* 57.18 (1998), pp. 11184–11192.

[78] G. Grimvall. *Thermophysical Properties of Materials*. 1. Aufl. s.l.: Elsevier professional, 1999. ISBN: 0444827943.

[79] L. C. Dufour and C. Monty. *Surfaces and Interfaces of Ceramic Materials*. Springer Netherlands, 2012. ISBN: 9789400910355.

[80] J. S. Lee, C. Minkwitz, and Ch. Herzig. "Grain Boundary Self-Diffusion in Polycrystalline Tungsten at Low Temperatures". In: *physica status solidi (b)* 202.2 (1997), pp. 931–940. ISSN: 03701972.

[81] C. P. Buhsmer and P. H. Crayton. "Carbon self-diffusion in tungsten carbide". In: *Journal of Materials Science* 6.7 (1971), pp. 981–988. ISSN: 1573-4803.

[82] Christian Cherubini, Simonetta Filippi, Alessio Gizzi, and Ricardo Ruiz-Baier. "A note on stress-driven anisotropic diffusion and its role in active deformable media". In: *Journal of theoretical biology* 430 (2017), pp. 221–228.

[83] Max O. Bloomfield, Daniel N. Bentz, and Timothy S. Cale. "Stress-Induced Grain Boundary Migration in Polycrystalline Copper". In: *Journal of Electronic Materials* 37.3 (2008), pp. 249–263. ISSN: 1543-186X.

[84] Chong Yong Lee. "Positron Annihilation Study of Vacancy Type Defects in Ti, Si, and BaSrFBr:Eu". In: *Applied Science and Convergence Technology* 25.5 (2016), pp. 85–87.

[85] M. J. Fluss, L. C. Smedskjaer, M. K. Chason, D. G. Legnini, and R. W. Siegel. "Measurements of the vacancy formation enthalpy in aluminum using positron annihilation spectroscopy". In: *Physical Review B* 17.9 (1978), pp. 3444–3455.

[86] M. J. Fluss, L. C. Smedskjaer, R. W. Siegel, D. G. Legnini, and M. K. Chason. "Positron annihilation measurement of the vacancy formation enthalpy in copper". In: *Journal of Physics F: Metal Physics* 10.8 (1980), pp. 1763–1774. ISSN: 0305-4608.